Dissertation for PhD

Evolution of the Electronic Phase Diagram for Iron-based Superconductor $LaFeP_{1-x}As_xO_{1-y}F_y$ $(y = 0 - 0.1)$

Department of Physics, Graduate School of Science

Osaka University

Kwing To Lai

August 2014

Abstract

Superconductivity of iron-based superconductor LaFeAsO can be induced by suppressing the antiferromagnetic phase through F doping. On the other hand, LaFePO itself is a superconductor, and F doping cannot significantly change T_c. The difference between the electronic behaviors in LaFeAsO and LaFePO can be realized from the difference in their Fermi surface topologies. In particular, around Γ point, a 3-dimenional Fermi surface with d_{Z^2} orbital character appears at in LaFePO, while there is a cylindrical Fermi surface with the $d_{X^2-Y^2}$ orbital character in LaFeAsO. In our previous study in $R\mathrm{FeP}_{1-x}\mathrm{As}_x\mathrm{O}_{0.9}\mathrm{F}_{0.1}$ (R = La, Pr, Nd), a maximum $T_c \sim 28$ K as well as T-linear behavior in resistivity and strong temperature dependent R_H are observed at $x = 0.6$ in R = La. Similar behaviors at $x = 0.6$ are also able to be observed in R = Pr and Nd in spite of the difference in lattice size. It suggests that these behaviors are driven by the change of electronic states due to P/As substitution, and such change corresponds to the exchange of the energy levels of the d_{Z^2} and $d_{X^2-Y^2}$ bands. We call this exchange as band crossover.

In this study, the effect of the band crossover has been further investigated by studying the electronic properties of polycrystalline $\mathrm{LaFeP}_{1-x}\mathrm{As}_x\mathrm{O}_{1-y}\mathrm{F}_y$ with $y = 0$ and 0.05. For $y = 0$, a new superconducting dome (SC1 dome) with a maximum T_c of 12 K is observed around $x = 0$ – 0.3. This is separated from another SC dome (SC1 dome) with T_c ∼10 K at $x = 0.6$ – 0.8 by an antiferromagnetic region around $x = 0.3$ – 0.6 (AFM2 phase) which is detected by NMR measurements. These behaviors construct a two-dome

structure in the corresponding phase diagram. As y increases, the two SC domes merge together, changing to a double-peak structure at $y = 0.05$, and a single dome at $y = 0.1$. The evolution of the electronic behaviors shows that SC2 dome expands as y increases, and merges with SC1 dome. The expansion of SC2 dome is due to the spin fluctuation coming from the suppression of AFM2 phase when y increases. Strong temperature dependence of Hall coefficient is observed at $x = 0.3$ – 0.8 for $y = 0$, and at $x = 0.6$ – 0.8 for $y = 0.05$ and 0.1. This indicates the reconstruction of Fermi surface due to the band crossover and the presence of two different Fermi surface states in this system.

In addition, the magnetic properties of AFM2 phase for $y = 0$ is different from the antiferromagnetic phase in LaFeAsO (AFM1 phase). It is revealed by NMR that AFM2 phase has a long-ranged order but the magnetic moment is smaller than AFM1 phase. Furthermore, the magnetic transition is rather smooth without any structural transitions. The density of states revealed by NMR and specific heat decreases with increasing x, and it particularly decreases faster around the emergence of AFM2 phase, suggesting that the shrinkage of the d_{Z^2} band is essential for the formation of AFM2 phase.

Acknowledgement

I would like to express my sincere gratitude to my supervisors, Prof. Setsuko Tajima and Prof. Shigeki Miyasaka, for their supervision, advice and guidance in these three years. They inspired me the way to do good research on physics and enriched my research skill, presentation skill as well as writing skill. I also would like to thank their help when I met some language problems on research.

I would like to thank Mr. Akira Takemori for his contribution to this study in the measurement of Hall effect and his teaching for the experimental techniques. I also appreciate his study for $LaFeP_{1-x}As_xO_{0.9}F_{0.1}$ and the discussions with him.

I would like to thank Prof. Kiyohisa Tanaka, Prof. Masamichi Nakajima, Mr. Tatsuka Kobayashi, Mr. Taichi Tokuhisa and Mr. Masahiro Uekubo for their support on experiments and discussions. The support from Prof. Akiko Nakao, Prof. Hironori Nakao, Prof. Reiji Kumai and Prof. Youichi Murakami for the experiments in KEK, and Prof. Takehito Nakano for the specific heat measurements was also grateful.

I also would like to thank Dr. Ece Uykur for the development of the Matlab code for plotting the phase diagram of $LaFeP_{1-x}As_xO_{1-y}F_y$ and fruitful discussions. The fun time with her outside research was also adorable.

Moreover, I would like to express my special thank to Prof. Hidekazu Mukuda for fruitful discussion. His idea helped us to improve the quality of this study.

I also appreciate the interesting discussions with Prof. Kazuhiko Kuroki and his invitation to the seminar in his group.

Thanks are also forwarded to the Takuetsu program for the financial support to the trip for the American Physical Society March Meeting in Denver, USA on March, 2014. The meeting broadened my horizon and inspired my idea for my future research.

Last but not least, I would like to acknowledge the lab members for their support, especially for some problems in daily life, and the fun time in the parties. Special thank is given to the secretary of our lab, Miss Yoshiko Ishimoto, who helped me to deal with many documents and some daily-life issues. I also appreciate the fun time with Tan Thi Pham, Minh Hien Nguyen.

Finally, I would like to thank my family and Miss Angela Siu Yee Lam for their continuous support and encouragement.

Contents

List of Figures

Make the dreams come true,

Make the dreams bigger!

Chapter 1

Introduction

1.1 Background

1.1.1 Basic Facts of Iron-based Superconductors

In 2008, a Japanese research group, Hosono group in Tokyo Institute of Technology, discovered a new superconductor, $LaFeAsO_{1-x}F_x$, with critical temperature T_c of about 26 K [1]. Physicists were surprised with such high T_c in a compound including a magnetic Fe atom, and a lot of related research was thus started. Over these several years, many kinds of related compounds were discovered, such as RFeAsO (R = rare earth metals) [2, 3, 4, 5, 6, 7], AFe$_2$As$_2$ (A = alkaline earth metals, Eu) [8, 9, 10, 11], LiFeAs [12], FeSe [13], etc. The highest T_c among these compounds are about 55 K. Since all of them contain Fe in their chemical formulae, this family of superconductors is named as iron-based superconductors.

1.1.2 Physical Properties of Iron-based Superconductors

1111-type Systems

RFePnO-type iron-based superconductors (Pn = As, P) are often categorized as 1111-type because of their ratio of the elements in their chemical formulae (1:1:1:1). Their crystal structure is a tetragonal layered structure, with the space group $P4/nmm$ at room temperature, as illustrated in Fig. 1.1. The superconducting layer is the quasi-2D layer consisting of Fe atoms bonding with As atoms, while the charge-reservoir layer is the R-O layer. The maximum T_c can be achieved to about 55 K in this family.

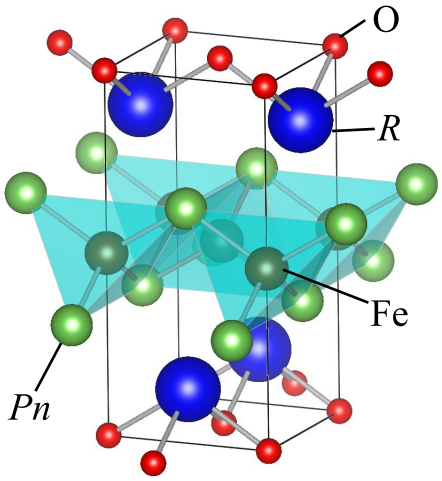

Figure 1.1: The crystal structure of RFePnO.

For Pn = As, the (undoped) parent compounds are spin-density-wave (SDW) metals with the transition temperature T_N ~140 K. The magnetic behavior below T_N can be observed via different techniques like neutron scattering [14]. There is a structural transition from tetragonal to orthorhombic at the temperature T_s slightly higher than T_N, namely ~160 K. Using temperature dependent X-ray diffraction, a Bragg peak (220) observed at $T > T_s$ splits into two peaks when it is measured at $T < T_s$, indicating the structural transition [15]. Moreover, this transition gives a characteristic kink in temperature dependence of resistivity as illustrated in Fig. 1.2, and shows two jumps

around 140 K $< T <$ 160 K in specific heat measurement as shown in Fig. 1.3, which correspond to T_N and T_s, respectively [16].

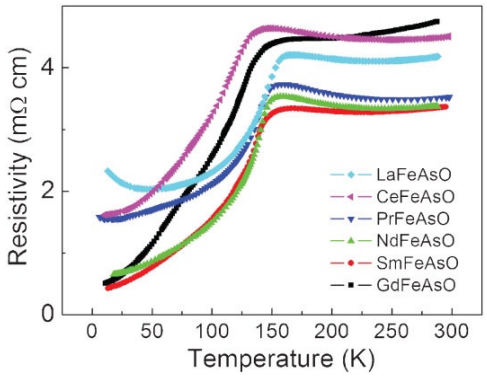

Figure 1.2: The temperature dependence of resistivity of RFeAsO (R = La, Ce, Pr, Nd, Sm and Gd) [17].

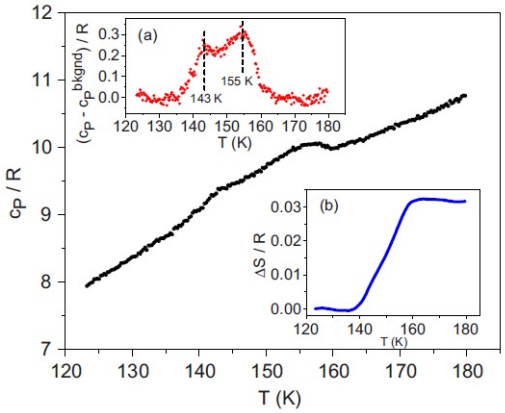

Figure 1.3: The temperature dependence of specific heat of LaFeAsO [16].

Upon the introduction of additional electrons, like substituting O to F, the SDW state is suppressed and superconductivity (SC) is induced. The details about the effect of doping will be described in Section 1.1.3. Similar phenomenon can also be observed in hole doped system like substituting R to Sr in $R_{1-x}\mathrm{Sr}_x\mathrm{FeAsO}$, with $T_c \sim 25$ K for R = La [18].

Apart from cation substitution, SC can also be induced by oxygen deficiency. Oxygen deficient samples $R\mathrm{FeAsO}_{1-\delta}$ have been prepared by high-pressure synthesis [19]. By

increasing the value of δ to $\sim$0.05, the systems experience the phase transition from SDW to SC, which is similar to the case in cation substitution. T_c can also be achieved to about 55 K.

Applying pressure to the parent compound can also induce SC. For example, applying 12 GPa to LaFeAsO can induce SC with T_c of 21 K [20]. Since the lattice size is reduced by pressure, it suggests the close correlation between structural parameters and SC, which will be discussed in more details in Section 1.4.

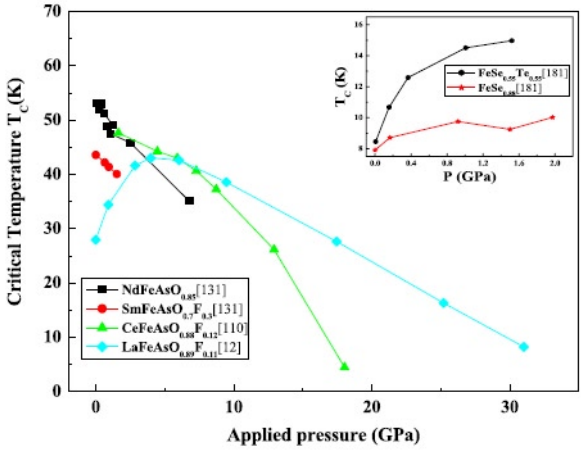

Figure 1.4: The pressure dependence of T_c of RFeAsO$_{1-x}$F$_x$ (R = La, Ce, Nd, Sm). The inset is the pressure dependence of T_c of FeSe$_{0.88}$ and FeSe$_{0.55}$Te$_{0.55}$ [21].

On the other hand, the pressure effect on F-doped 1111 systems is more complicated. The pressure dependence of T_c of RFeAsO$_{1-x}$F$_x$ (R = La, Ce, Nd, Sm) is illustrated in Fig. 1.4. In most of the cases, the T_c of RFeAsO$_{1-x}$F$_x$ decreases when the pressure increases [3, 22], but the T_c of LaFeAsO$_{1-x}$F$_x$ first increases and then decreases with increasing pressure, and it peaks at $\sim$5 GPa [23]. This unique behavior in LaFeAsO$_{1-x}$F$_x$ compared to other F-doped 1111 systems suggests the electronic structure of LaFeAsO is essentially different from other 1111 systems.

In the case of Pn = P, the parent compound is superconducting except CeFePO. T_c found in LaFePO is $\sim$5 K [24] and that in (Pr/Nd/Sm)FePO is $\sim$3 K [25, 26], while

CeFePO is a heavy-fermion compound [27].

A similar system AeFeAs(F/H) (Ae = Ca, Sr and Eu) has also been reported [28, 29]. This system has the same crystal structure as RFeAsO, and the parent compounds are also SDW. Upon the substitution of Fe by Co, Ni [30, 31, 32] or Ae by R [29, 33], SC can be induced.

It is worth to note that most of the studies in 1111 systems are performed with polycrystalline samples since the growth of single crystals is difficult, especially the doped samples. Although some groups have reported some successful growth of single crystals [34, 35], the further investigations for these samples are still difficult due to either small size or poor quality.

122-type Systems

122-type systems correspond to AFe$_2$As$_2$-type iron-based superconductors. Similar to 1111 systems, they are named because of their chemical ratio (1:2:2). At room temperature, their crystal structure is also a tetragonal layered structure, but the space group is $I4/mmm$. The difference of the crystal structure compared to 1111 systems can be visualized in Fig. 1.5. In particular, the charge-reservoir layer in 122 systems is replaced by A.

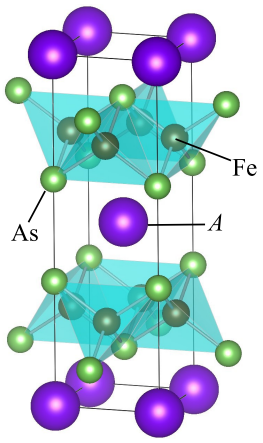

Figure 1.5: The crystal structure of AFe$_2$As$_2$.

The parent compound of 122 systems is also a SDW metal with $T_N \sim 150$ K, and structural transition from tetragonal to orthorhombic above T_N. It will also undergo phase transition from SDW to SC, similar to 1111 systems, if it is doped.

There are three kinds of doping that can induce SC: hole doping, electron doping and isovalent doping. In the following, $BaFe_2As_2$ (Ba122) will be taken as an example to discuss the effect of doping in 122-type systems. For the ease of the following discussion, the phase diagrams of K-doped, Co-doped and P doped Ba122 are summarized in Fig. 1.6.

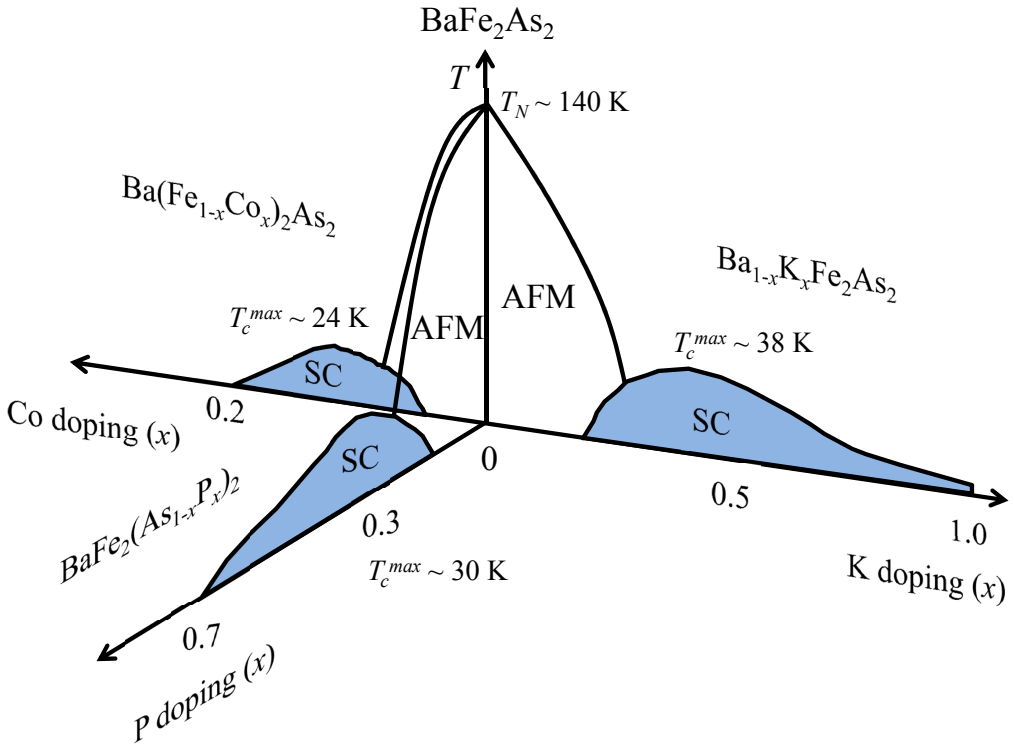

Figure 1.6: The phase diagrams of $Ba_{1-x}K_xFe_2As_2$ [8], $Ba(Fe_{1-x}Co_x)_2As_2$ [39] and $BaFe_2(As_{1-x}P_x)_2$ [40].

Hole doping can be achieved by substituting Ba by K in Ba122. K doping introduces one hole carriers to $Ba_{1-x}K_xFe_2As_2$, giving the maximum $T_c \sim 38$ K around $x = 0.4$ [8]. The SC gap is found to be nodeless via angle-resolved photoemission spectroscopy [36].

SC remains up to $x = 1.0$ (KFe_2As_2, K122) with $T_c \sim 4$ K [37]. However, the SC gap in K122 is found to be nodal [38], indicating the difference of their electronic states.

In the case of electron doping, Co doped $Ba(Fe_{1-x}Co_x)_2As_2$ is the most commonly studied system due to the ease of the production of the corresponding single crystals. Upon Co doping, an extra electron is introduced to the system. Only few % of Co doping is enough to suppress SDW state, and SC is observable, for instance, with $T_c \sim$24 K at $x = 0.06$ for [39]. SC disappears at further doping ($x \sim$0.3). Note that the substitution of Co for Fe in the superconducting Fe-As layer does not hinder the appearance of SC, which is different from cuprates.

Isovalent doping can be demonstrated by P doped $BaFe_2(As_{1-x}P_x)_2$. Since P has the same valence as As, no additional carriers are introduced to the system by P doping, but the size of the lattice decreases due to the smaller atomic radius of P atoms, resulting in chemical pressure. Chemical pressure is named because it has a similar effect to applying physical pressure to the system which will shrink the lattice size. After the introduction of P atoms, SDW is again suppressed and SC occurs around $x = 0.3$ with $T_c \sim 30$ K [40]. SC persists until $x > 0.7$. When the amount of P content increases ($0.2 \leq x \leq 0.7$), the behavior of resistivity changes from non-Fermi-liquid type to Fermi-liquid type, which points out the existence of spin fluctuations near the boundary of the phase transition known as quantum critical point (QCP).

By summarizing the electronic behaviors induced by the three kinds of doping in Ba122, a few similarities can be found in their properties. Each doping shows a similar trend that SC appears after the suppression of SDW, forming a SC dome across the phase diagram. Moreover, around the QCP, there is a small region for the coexistence of SDW and SC. Such behaviors point out that the close relationship between antiferromagnetism (AFM) and SC is common in various doped Ba122. It also suggests that the spin fluctuation originating from AFM near QCP is a possible candidate the pairing force of Cooper pairs.

In 122 systems, SC can also be induced by applying external pressure. After the suppression of SDW, Ba122 and Sr122 show SC with T_c ∼30 K at pressure of 4 GPa, while Ca122 shows SC with T_c ∼12 K at pressure of 0.5 GPa [41, 42, 43]. Applying higher pressure, Ba122 (∼27 GPa) and Sr122 (∼1 GPa) experience structural change known as collapsed tetragonal phase, which shows decrease in length of c-axis [44, 45].

$A_x Fe_{2-y} Se_2$ A similar system $A_x Fe_{2-y} Se_2$ (A = K, Rb, Cs, Tl) with the same crystal structure as 122 systems has also been widely studied [46]. However, the physical properties of this system are very different from other 122 systems. It is an intrinsically heavily electronic doped system, so hole Fermi surface is not able to be detected by ARPES [47, 48]. A strong AFM behavior with the highest T_N ($>$ 500 K) among iron-based superconductors is also observed in this system.

Furthermore, its electronic behaviors can be altered by adjusting the amount of iron vacancy. Figure 1.7 shows the phase diagram of $K_x Fe_{2-y} Se_2$ with various amount of iron vacancy [49]. All samples show magnetic transition from paramagnetic to AFM at ∼530 K. At the region of iron vacancy from 1.93 – 2.00, the AFM phase is rather metallic and coexists with SC of T_c ∼30 K. In the data of temperature dependence of resistivity and magnetic susceptibility as shown in Fig. 1.8, a hump in the resistivity data can be found around 200 K. In other regions, only AFM insulator can be observed.

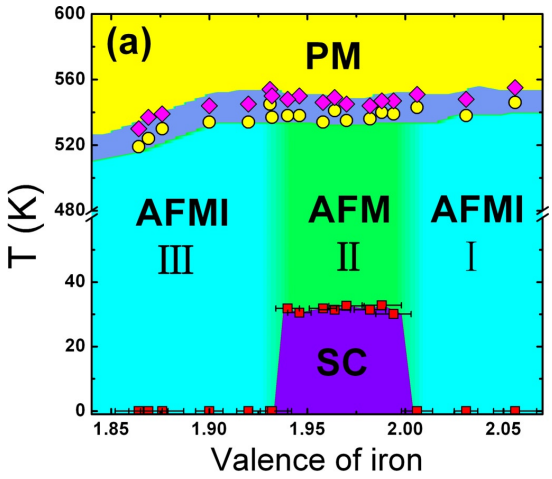

Figure 1.7: The phase diagrams of $K_xFe_{2-y}Se_2$ with various amount of iron vacancy [49].

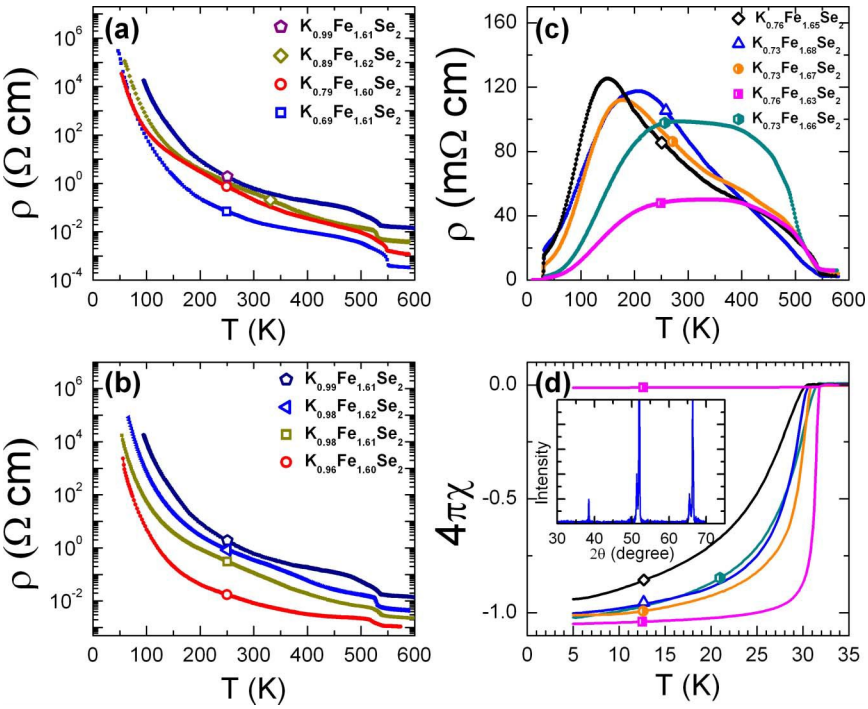

Figure 1.8: The temperature dependence of resistivity and magnetic susceptibility of $K_xFe_{2-y}Se_2$ [49].

The iron vacancy has been identified by neutron scattering as the origin of AFM, giving a $\sqrt{5} \times \sqrt{5}$ modulation in the magnetic unit cell [50]. The coexistence of AFM and SC can be realized as phase separation. Through scanning tunneling microscopy (STM), nanoscale phase separation between AFM and SC has been detected [51]. As illustrated in the corresponding STM image (Fig. 1.9), two kinds of phases can be clearly observed. In particular, one is the AFM insulating phase, while the other is the paramagnetic metallic/SC phase without iron vacancy.

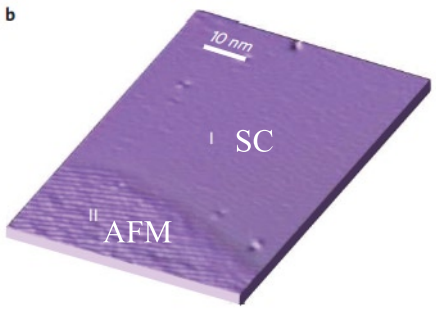

Figure 1.9: The STM image of $K_xFe_{2-y}Se_2$ [51].

Applying very high pressure (> 10 GPa), SC in $A_xFe_{2-y}Se_2$ is once suppressed and reappears with higher $T_c \sim 48$ K [52], as shown in the pressure dependent phase diagram in Fig. 1.10. This behavior once again demonstrates the uniqueness of $A_xFe_{2-y}Se_2$.

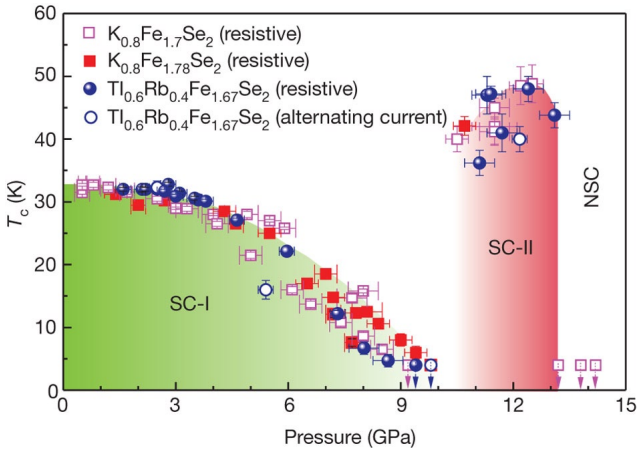

Figure 1.10: The pressure dependent phase diagram of $A_xFe_{2-y}Se_2$ [52].

Others

111-type systems AFePn (A = Li, Na; Pn = As, P) is called 111-type iron-based superconductor. Their crystal structure is also tetragonal with space group of $P4/nmm$ at room temperature, as shown in Fig. 1.11. Unlike 1111- and 122-type systems, the parent compound itself is superconducting. For example, T_c of LiFeAs is around 17 K, while that of LiFeP is around 5 K [12, 53].

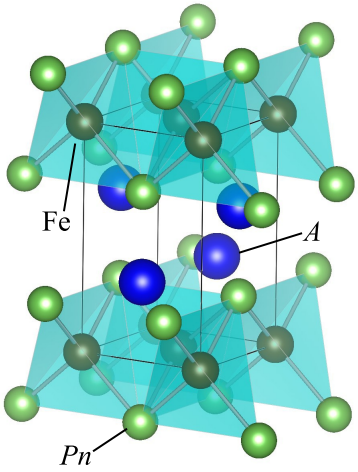

Figure 1.11: The crystal structure of AFePn.

11-type systems The type of iron-based superconductors has the simplest chemical composition: α-FeSe, with tetragonal crystal structure at room temperature (space group: $P4/nmm$). The corresponding crystal structure is illustrated in Fig. 1.12. The parent compound itself is superconducting with $T_c \sim 8$ K [13]. By applying high pressure at 7 – 9 GPa, T_c can be increased up to ∼37 K [41] (See the inset in Fig. 1.4). T_c can also be increased up to ∼15 K through substitution of Se by Te or S [21].

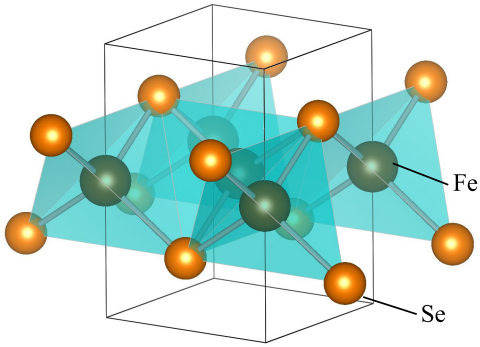

Figure 1.12: The crystal structure of FeSe.

Multilayer systems In this class of iron-based superconductors, the charge-reservoir layer is more complicated than the other systems, which composes two or three Fe-As layers and perovskite oxide layers in a unit cell. For example, SC with $T_c = 38$ K can be found in $Ca_{10}(Pt_4As_8)(Fe_{2-x}Pt_xAs_2)_5$ [54].

A similar system $(Ca_4Al_2O_6)Fe_2(As_{1-x}P_x)_2$ shows a special behavior that nodeless SC around $x = 0$ and nodal SC at $x = 1$ are separated by an AFM phase [55], as illustrated in the corresponding phase diagram in Fig. 1.13.

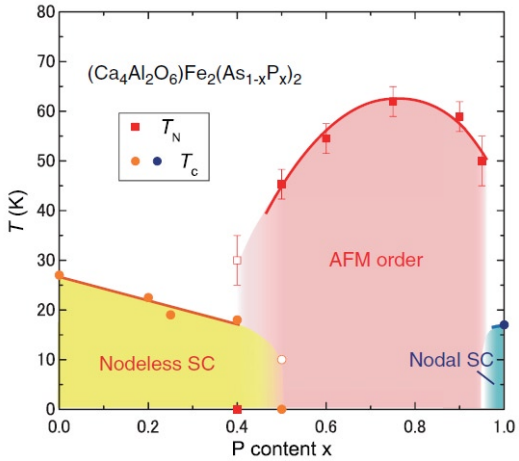

Figure 1.13: The phase diagram of $(Ca_4Al_2O_6)Fe_2(As_{1-x}P_x)_2$ [55].

1.1.3 Doping Dependence of 1111-type Systems and Their Physical Properties

The effect of doping in iron-based superconductors has been one of the focuses in the research of iron-based superconductors since their discovery, because doping not only induces SC, but also causes different kinds of physical properties for various cases. Such abundant behaviors stimulate the understanding of SC in iron-based superconductors, establishing the importance of studying the effect of doping. In this section, the effect of doping in 1111-type systems and the corresponding behaviors will be discussed.

F-doped 1111-type Systems

The substitution of O by F in 1111-type systems introduces additional electrons as well as shrinkage of lattice size, resulting in the change of the electronic structure. As mentioned in Section 1.1.2, SC can be induced upon F doping after the suppression of SDW.

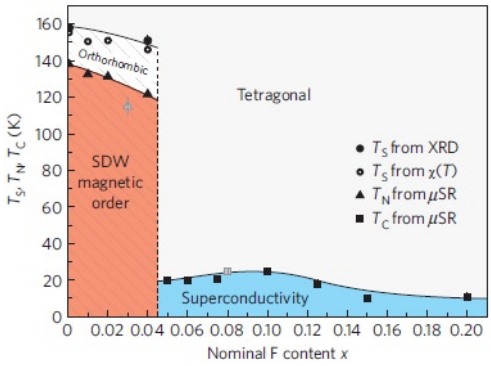

Figure 1.14: The phase diagram of $LaFeAsO_{1-x}F_x$ [56].

Taking La1111 [56] as an example, the phase diagram of $LaFeAsO_{1-x}F_x$ is illustrated in Fig. 1.14. When F concentration x increases, T_N of the SDW state starts to decrease gradually. When x increases to ~ 0.4, the SDW state suddenly disappears and SC is developed. This situation is different from the case of 122 systems that SDW and SC

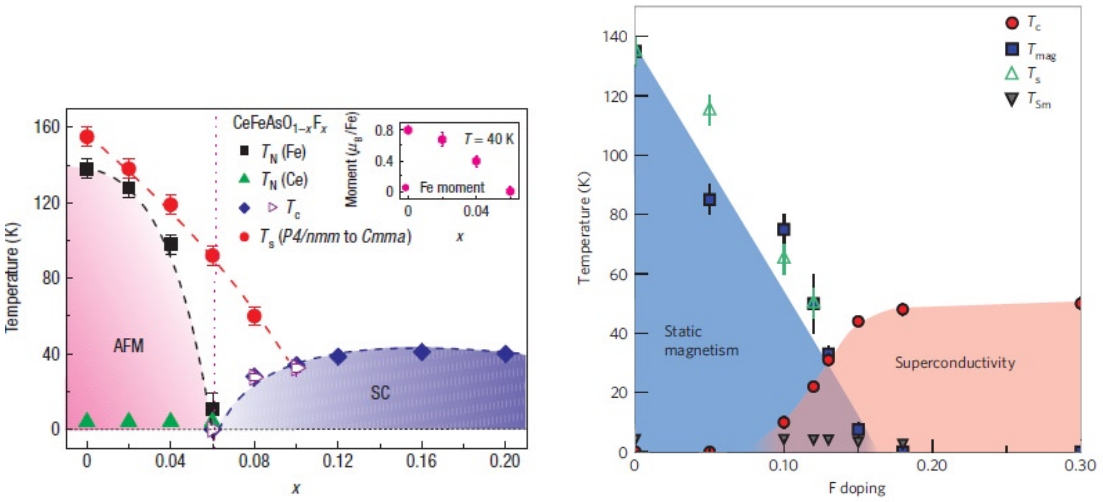

Figure 1.15: The phase diagrams of (Left) $CeFeAsO_{1-x}F_x$ [4] and (Right) $SmFeAsO_{1-x}F_x$ [57].

coexist in a certain range of doping when SC is emerging. Similar behaviors can be found in other kinds of 1111 systems, like Ce1111 [4] [1] and Sm1111 [57], as shown in their phase diagrams in Fig. 1.15. Such a sharp phase transition is uniquely found in 1111 systems among various kinds of iron-based superconductors. There are some studies arguing that there is coexistence of SDW and SC in the boundary of the phase transition [57, 58], but the evidence is not very convincing.

On the other hand, the effect of F doping in $LaFePO_{1-x}F_x$ shows a different story from what we have seen in $LaFeAsO_{1-x}F_x$. The phase diagram of $LaFePO_{1-x}F_x$ is shown in Fig. 1.16. Across various F concentratiosn from 0 to 0.08, the value of T_c does not change significantly, suggesting that the SC in LaFePO is not sensitive to introduction of charge carriers and/or structural changes [59].

It is important to note that the maximum F concentration is about 0.2 in all the studies of F-doped samples due to the low solubility of F^- ions in 1111 systems. This difficulty with synthesizing heavily F-doped samples hinders the further understanding

[1] In $CeFeAsO_{1-x}F_x$, the Ce magnetic order coexists with the Fe magnetic order in the SDW state at $T \sim 4$ K [4]. This feature is uniquely found in Ce1111.

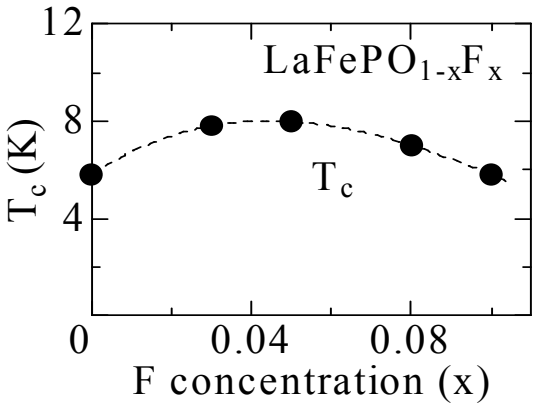

Figure 1.16: The phase diagram of $LaFePO_{1-x}F_x$ [59].

of the electronic doping dependence of 1111 systems.

H-doped 1111-type Systems

To overcome the problem about the solubility of F^- ions, electron doping has been introduced by using another element: H^- ions. Using high-pressure synthesis, polycrystalline RFeAs$O_{1-x}H_x$ (R = La, Ce, Sm, Gd) has been successfully synthesized with x up to ∼0.6 [60, 61, 62]. The phase diagram of RFeAs$O_{1-x}H_x$ (R = La, Ce, Sm, Gd) is shown in Fig. 1.17. At $x < 0.2$, the results are similar to the behaviors observed in F-doped samples. When the value of x becomes larger than 0.2, for R = Ce, Sm and Gd, the value of T_c does not change significantly up to $x \sim 0.4$ and the SC disappears around x = 0.5.

For R = La, however, T_c drops around x = 0.2, forming a two-dome structure in the phase diagram. This surprising result opens up the question about the origin of the two-dome structure. One of the clues appears on the value of the exponent n, which represents the temperature dependence of resistivity at the normal state by the following equation:

$$\rho(T) = \rho_0 + AT^n, \tag{1.1}$$

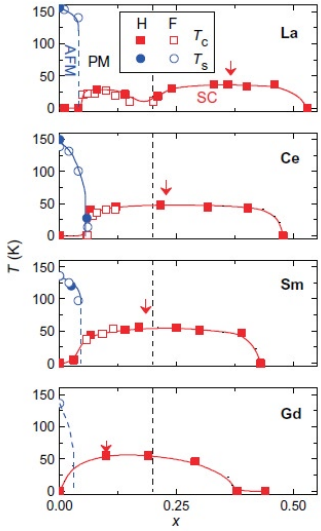

Figure 1.17: The phase diagram of $R\mathrm{FeAsO}_{1-x}\mathrm{H}_x$ (R = La, Ce, Sm, Gd) [63].

where ρ_0 is the residual resistivity and A is the slope of $\rho(T)$. By fitting the resistivity data from T_c to 150 K, the value of n is found to be $\sim$2 at $x < 0.2$ (SC1 dome) but $\sim$1 at $x > 0.2$ (SC2 dome). According to the Fermi liquid theory, the value of n in conventional metals, which are described as a Fermi liquid without strong electron interactions, should be 2 [64]. This result thus indicates that the transport behavior of the samples in SC1 dome is Fermi liquid while that in SC2 dome is non-Fermi liquid. That is, the electronic structure of these two regions is different from each other.

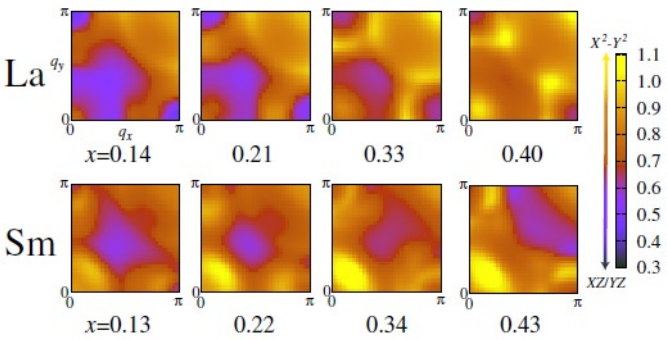

Figure 1.18: The ratio of the intra-orbital spin susceptibilities originating from the $d_{X^2-Y^2}$ and $d_{XZ/YX}$ bands for various H doping level for La1111 (top) and Sm1111. (bottom) [66].

Theoretical studies suggest that the nature of the d-bands and the condition of Fermi surface nesting change due to H doping [65, 66, 67, 68, 69]. For example, the spin fluctuation in SC1 dome is originated by $d_{XZ/YX}$ band while that in SC2 dome is originated by $d_{X^2-Y^2}$ band, as shown in Fig. 1.18. Comparing with the different value of n in the 2 domes, it suggests that the non-Fermi liquid behavior in transport properties is mainly contributed by the $d_{X^2-Y^2}$ band.

Moreover, the wavevector of Fermi surface nesting changes from $(0,\pi)/(\pi,0)$ in SC1 dome to $(\pi,\sim\pi/3)/(\sim\pi/3,\pi)$ in SC2 dome, as illustrated in Fig. 1.19. Such differences consequently affect the SC of the two regions through the different configuration of spin and/or orbital fluctuations [68, 69], resulting in the characteristic two-dome structure. Nevertheless, the question whether the SC is mainly induced by spin or orbital fluctuations still remains unclear.

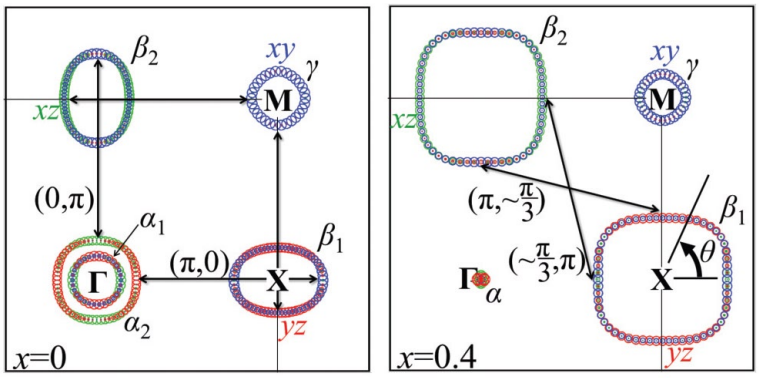

Figure 1.19: The Fermi surface of $LaFeAsO_{1-x}H_x$ for (Left) $x = 0$ and (Right) $x = 0.4$ [67].

More interestingly, when the amount of x further increases to ~0.5 in $LaFeAsO_{1-x}H_x$, reemergence of an AFM phase is observed [70, 71], as shown in the extended phase diagram of $LaFeAsO_{1-x}H_x$ in Fig. 1.20. Using NMR, neutron diffraction and μSR technique, it is revealed that the magnetic structure and the magnetic moment of the AFM phase in the overdoped region (AF2 phase) show differences from the AFM phase in the undoped region (AF1 phase), as shown in the inset of Fig. 1.20. This picture

suggests that the SC at $x > 0.2$ (SC2 dome) stems from AF2 phase, i.e. this AFM phase acts as another "parent compound" for the SC in SC2 dome. Since the magnetic behavior of AF2 phase is different from that of AF1 phase, the mechanism of SC in SC2 dome induced by the suppression of AF2 phase should be different from the SC in SC1 dome. The crossover of these two kinds of SC mechanism eventually results in the two-dome structure in the phase diagram of $LaFeAsO_{1-x}H_x$.

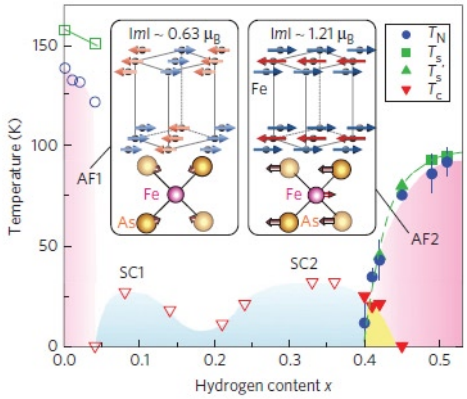

Figure 1.20: The extended phase diagram of $LaFeAsO_{1-x}H_x$ [71].

Effect of P/As Substitution in 1111-type Systems

P/As substitution[2] in 1111-type systems causes no additional carrier introduction due to the same valence of P^{3-} and As^{3-} ions, but the smaller ionic size of P^{3-} ions causes shrinkage of lattice size. This effect is analogous to the effect of applying external pressure to the systems. Hence it is sometimes called chemical pressure. In the following section, the behaviors of some P/As substituted 1111 systems will be discussed.

$LaFeAs_{1-x}P_xO$ Polycrystalline $LaFeAs_{1-x}P_xO$ with $x = 0 - 0.5$ has been first synthesized by C. Wang *et al.* (Z. A. Xu group in Zhejiang University, China) [72]. The behaviors of the doping dependence are summarized in Fig. 1.21. Increasing P content

[2]The randomness effect is believed not to be strong since P/As substitution does not disorder the systems seriously.

suppresses the SDW state and SC is observed around $x = 0.3$ with maximum $T_c \sim 10$ K. The further NMR study of this system shows another AFM phase at $x \sim 0.5$ with $T_N \sim 15$ K [73]. The nature of this AFM phase is seemingly different from the SDW state in the parent compound, because the magnitude of the internal field $H_{int}(T)$ in the SDW state follows the mean-field-type dependence, i.e. $H_{int}(T) \propto (T_N - T)^{0.5}$, while $H_{int}(T)$ of this AFM phase increases linearly with T. It suggests that the AFM phase around $x = 0.5$ may be a short-ranger order like spin glass.

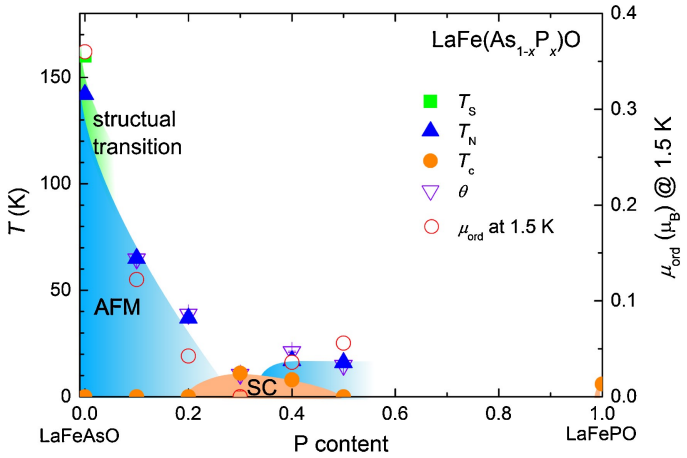

Figure 1.21: The phase diagram of $LaFeAs_{1-x}P_xO$ [73].

$SmFeAs_{1-x}P_xO$, $SmFeAs_{1-x}P_xO_{1-y}$ and $SmFeAs_{1-y}P_yO_{1-x}H_x$ The doping dependence of polycrystalline $SmFeAs_{1-x}P_xO$ with $x = 0$ – 0.8 has been studied by the same group in Zhejiang University [74], and the temperature dependence of resistivity of the samples is shown in Fig. 1.22. A sharp drop in resistivity with onset $T_c = 4.1$ K is only observed at $x = 0.565$, indicating that the window for SC in $SmFeAs_{1-x}P_xO$ is very narrow.

Single crystals of $SmFeAs_{1-x}P_xO_{1-y}$ with $x = 0.4$ – 0.6 and $y \sim 0.15$ have also been synthesized by high-pressure synthesis with NaCl/KCl flux [75]. The oxygen deficiency induces SC in $SmFeAs_{0.5}P_{0.5}O_{0.85}$ with $T_c = 23.4$ K.

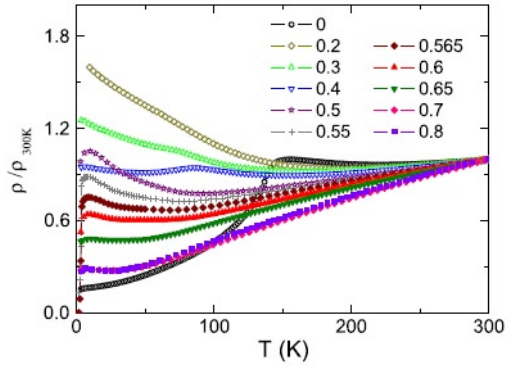

Figure 1.22: The temperature dependence of resistivity of $SmFeAs_{1-x}P_xO$ [74].

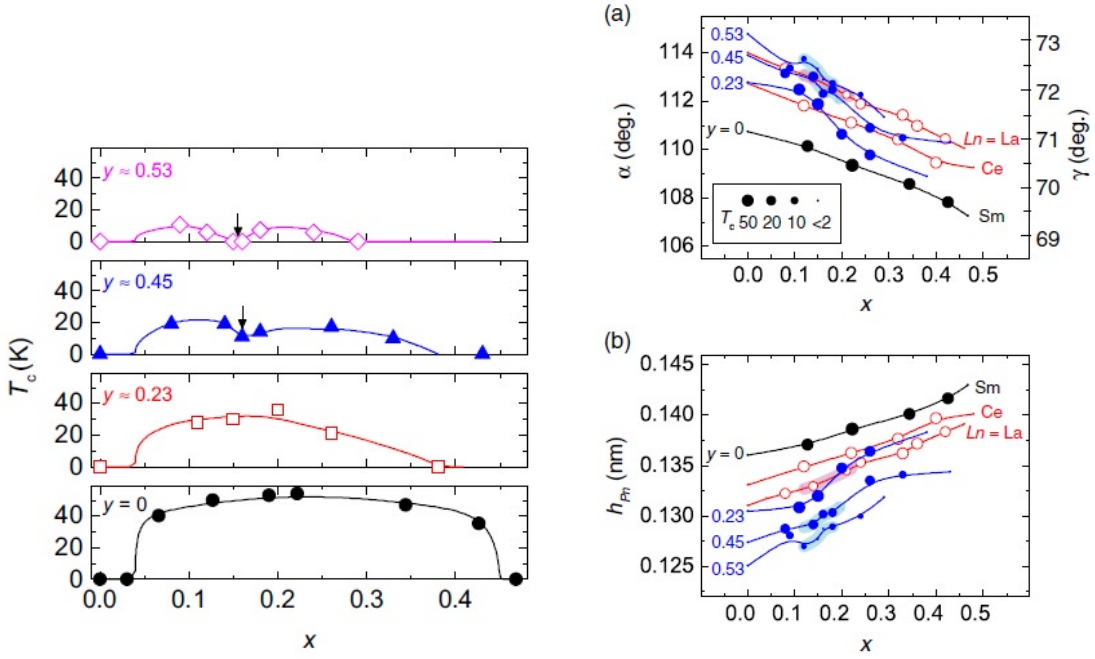

Figure 1.23: (Left) The x-dependence of T_c of $SmFeAs_{1-y}P_yO_{1-x}H_x$ (y = 0, 0.23, 0.45 and 0.53). (Right) The x-dependence of pnictogen height h_{Pn} and angle α of $SmFeAs_{1-y}P_yO_{1-x}H_x$. [76]

On the other hand, P and H co-doped $SmFeAs_{1-y}P_yO_{1-x}H_x$ with $x = 0$ – 0.5 and $y = 0$ – 0.53 has been investigated by Hosono group [76]. The x-dependence of the samples with different amount of P doping is shown in the left panel of Fig. 1.23. When P is slightly doped, T_c generally decreases and the SC dome becomes smaller. In the heavily P-doped samples ($y > 0.4$), a two-dome structure, which has been observed in $LaFeAsO_{1-x}H_x$, is revealed. It is argued that the change of the value of T_c is related to the change of structural parameters due to P doping. In the right panel of Fig. 1.23, which shows the x-dependence of the structural parameters, it suggests that the decrease in T_c is associated with the decrease in pnictogen height h_{Pn} and the increase in angle α [3].

$CeFeAs_{1-x}P_xO$ and $CeFeAs_{1-x}P_xO_{0.95}F_{0.05}$ Since CeFePO is not SC but a heavy-fermion compound, the phase diagram of $CeFeAs_{1-x}P_xO$ ($x = 0 - 1$) shows a complicated evolution of the electronic behaviors due to P/As substitution [27, 77], as illustrated in Fig. 1.24. When the amount of P increases, the SDW state is suppressed with the manner similar to F doping. At $x \sim 0.3$, the AFM order of Fe moments, the ferromagnetic (FM) order of Ce moments and SC with maximum $T_c \sim 4$ K coexist, forming a quantum critical point. Such complex behavior is thought to be a phase separation. When x exceeds 0.4, only the FM order of Ce moments is observed, and the FM state persists up to $x > 0.9$.

Similar behaviors can also be found in the phase diagram of $CeFeAs_{1-x}P_xO_{0.95}F_{0.05}$ [78], as shown in Fig. 1.25. At $x < 0.4$, SC with maximum $T_c \sim 20$ K coexists with the AFM order of Ce moments with $T_N \sim 5$ K. At $x \sim 0.5$, the AFM order disappears and the FM order arises which also coexists with SC. When the P content further increases, SC is suppressed and the FM state persists up to $x = 1$. Together with the behaviors observed in $CeFeAs_{1-x}P_xO$, we can conclude that these behaviors uniquely found in

[3] The definitions of h_{Pn} and α, and the discussions about the study of their relation to T_c can be referred to Section 1.4

P/As substituted Ce1111 are mainly due to the presence of the Ce moments.

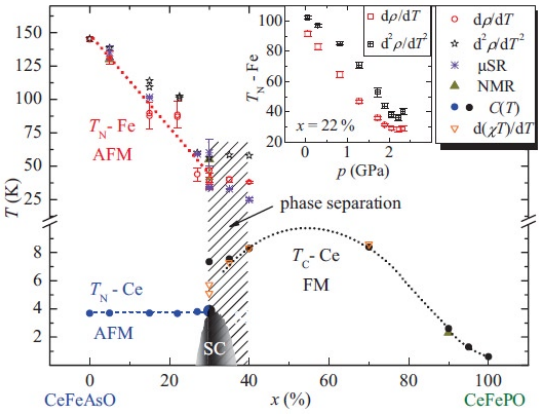

Figure 1.24: The phase diagram of $CeFeAs_{1-x}P_xO$ [77].

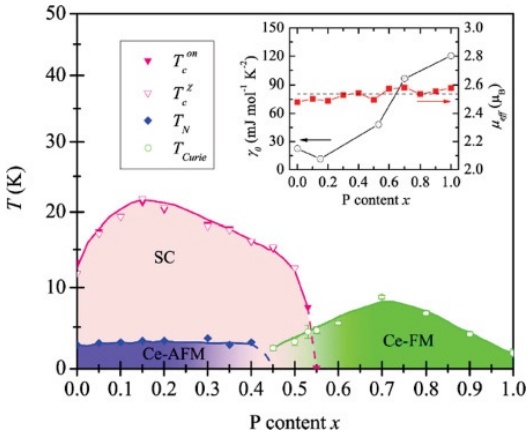

Figure 1.25: The phase diagram of $CeFeAs_{1-x}P_xO_{0.95}F_{0.05}$ [78].

$PrFe_{0.9}Co_{0.1}As_{1-x}P_xO$ The behaviors of P and Co co-doped $PrFe_{0.9}Co_{0.1}As_{1-x}P_xO$ have been studied by S. Sharma *et al.* [79]. The doping dependence of the SC properties is shown in Fig. 1.26. T_c shows a slight increase and then a decrease when x increases. This behavior is reminiscent of the effect of applying external pressure, proving that the chemical pressure induced by P doping has a similar effect as external pressure.

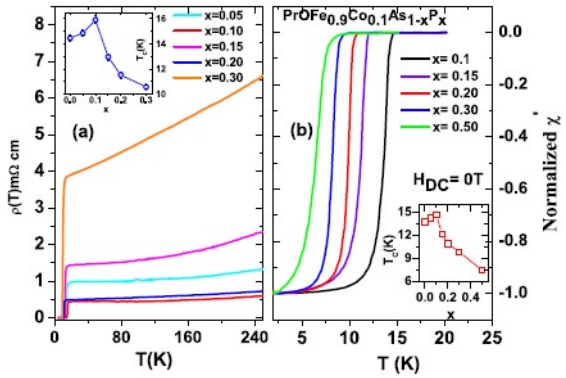

Figure 1.26: The doping dependence of the SC properties of $PrFe_{0.9}Co_{0.1}As_{1-x}P_xO$ [79].

***R*FeP$_{1-x}$As$_x$O$_{0.9}$F$_{0.1}$** In the previous work of our group, we have studied P/As substitution effect in RFeP$_{1-x}$As$_x$O$_{0.9}$F$_{0.1}$ (R = La, Pr, Nd) [80, 81, 82]. Their x-dependence of T_c and the exponent n in $\rho(T) = \rho_0 + AT^n$ [Equation (1.1)] is plotted in Fig. 1.27.

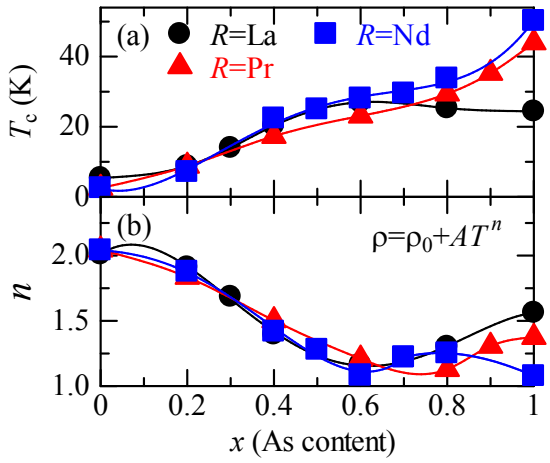

Figure 1.27: The x-dependence of (a) T_c and (b) the exponent n of RFeP$_{1-x}$As$_x$O$_{0.9}$F$_{0.1}$ (R = La, Pr, Nd) [82].

For R = La, a maximum $T_c \sim 28$ K is observed at $x = 0.6$ together with T-linearly dependent resistivity, while the T^2 behavior of resistivity is found at $x \sim 0$. It indicates that T_c is maximum when the sample is non-Fermi liquid, while the P-rich compounds are rather Fermi liquid. According to spin fluctuation theory, spin fluctuations near a

quantum critical point of an AFM phase induce non-Fermi-liquid behaviors[4], such as the T-linear behavior of resistivity for 2-dimenional AFM interactions [83]. Moreover, the enhancement of spin fluctuations around $x = 0.6$ is observed by the NMR technique [85]. Therefore, this implies that the increase in T_c correlates to the enhancement of spin fluctuations around $x = 0.6$.

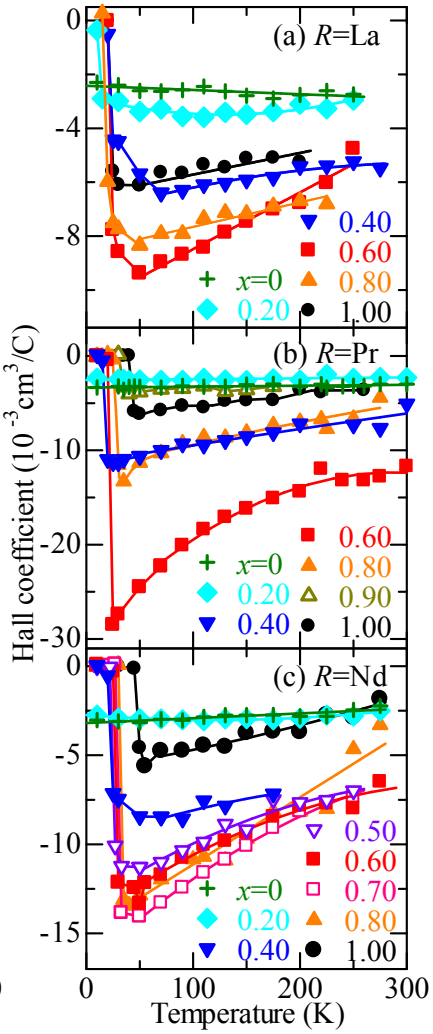

Figure 1.28: The temperature dependence of Hall coefficient R_H of $R\mathrm{FeP}_{1-x}\mathrm{As}_x\mathrm{O}_{0.9}\mathrm{F}_{0.1}$ (R = La, Nd, Pr) [82].

[4]Note that orbital fluctuations are also possible to induce non-Fermi-liquid behaviors [84].

For R = Nd and Pr, the T-linear behavior of resistivity is also found around $x = 0.6$, but T_c just increases almost linearly with increasing x. Together with the data for the case of La, it is obvious that T_c increases with decreasing n from $x = 0$ to 0.6, suggesting that SC in the P-rich samples is related to spin fluctuations. However, the relationship between T_c and n at $x > 0.6$ (or the As-rich samples) is not clear.

On the hand, temperature dependence of Hall coefficient R_H of $R\mathrm{FeP}_{1-x}\mathrm{As}_x\mathrm{O}_{0.9}\mathrm{F}_{0.1}$ provides more information about their electronic behaviors. The corresponding data is shown in Fig. 1.28. For all systems, the temperature dependence of R_H is the strongest at $x = 0.6$. Since Hall coefficient R_H is sensitive to the change of electronic states, it implies that there is a dramatic change in the electronic states driven by P/As substitution. Further discussions about this change will be continued in Section 1.2 and 1.3.

1.2 Band Structure Calculations in LaFeAsO and LaFePO

To understand the origin of the difference in their electronic properties between RFeAsO and RFePO, we shall look at their band structure and Fermi surface. Here we focus on the discussions in LaFeAsO and LaFePO for similarity[5]. Before we start, it should be reminded that iron-based superconductors are known as multiband systems. Their band structure near Fermi level consists of five Fe d-orbitals (hybridizated with As p-orbitals), so the Fermi surface will contain different kinds of orbital characters.

Figure 1.29 shows the band structures of LaFeAsO and LaFePO calculated by K. Kuroki *et al.* [86]. The total shape of their band structure is very similar, but there is a great difference. In LaFeAsO, the Fermi level from (π,π,0) to (π,π,π) is dominated by $d_{X^2-Y^2}$ band. Meanwhile in LaFePO, the Fermi level around (π,π,π) is dominated by d_{Z^2} band but no band touches the Fermi level around (π,π,0).

Consequently, the Fermi surfaces of LaFeAsO and LaFePO can be mapped and illus-

[5]The difference in the band structure of LaFeAsO and LaFePO is similar to the other 1111 systems. [86]

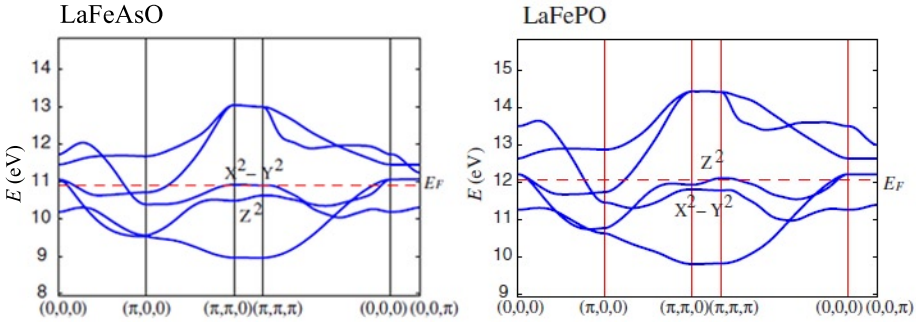

Figure 1.29: The band structures of (Left) LaFeAsO and (Right) LaFePO [86].

trated in Figs. 1.30 and 1.31, respectively. In LaFeAsO, the Fermi surface around Γ is a 2-dimensional tube along z-direction by virtue of the nature of $d_{X^2-Y^2}$ band. At the unfolded Brillouin zone mapping ($k_z = 0$), there is a hole Fermi pocket around (π,π). It is called γ pocket for convenience. On the other hand, the Fermi surface of LaFePO around Γ is a 3-dimensional pocket which is consistent with the domination of the d_{Z^2} band. More importantly, the γ pocket is absence around (π,π) at $k_z = 0$ mapping.

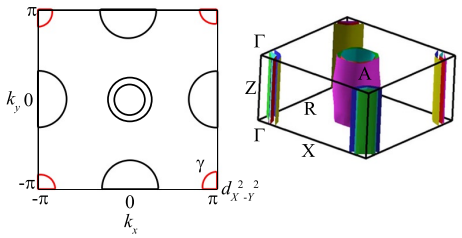

Figure 1.30: The Fermi surface of LaFeAsO [86, 87].

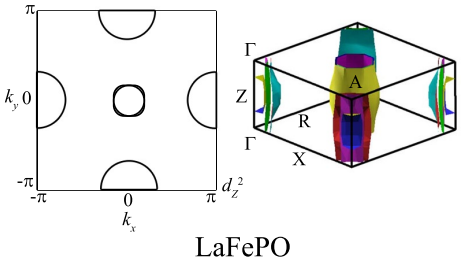

Figure 1.31: The Fermi surface of LaFePO [86, 87].

The difference in the orbital character near Fermi surface, or the occurrence of the γ pocket is believed to cause different electronic properties of LaFeAsO and LaFePO, such as Fermi surface nesting. The predicted Fermi surface nesting in LaFeAsO and LaFePO are illustrated in Fig. 1.32. With the presence of the γ pocket in LaFeAsO, electron Fermi pockets and hole Fermi pockets interact with the nesting vector (π,0) or (0,π), and this nesting can induce fully gapped s±-wave SC. In the case of LaFePO, however, the nesting condition is different due to the absence of the γ pocket. For instance, there is electron-electron Fermi pocket nesting. This nesting instead induces nodal s±-wave SC.

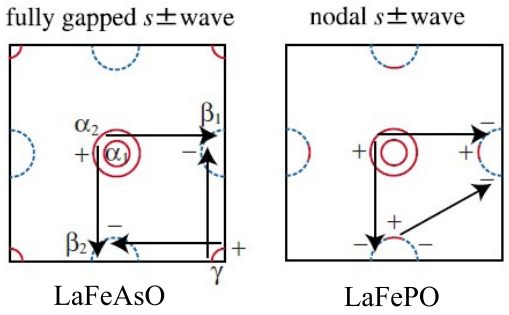

Figure 1.32: The Fermi surface nesting of (Left) LaFeAsO and (Right) LaFePO [86].

1.3 Band Crossover in $R\mathrm{FeP}_{1-x}\mathrm{As}_x\mathrm{O}_{0.9}\mathrm{F}_{0.1}$

In Section 1.2, it has been introduced that there is the difference between the band structures and Fermi surfaces of LaFeAsO and LaFePO, or generally *R*FeAsO and *R*FePO. Such difference naturally comes up a question: what will it happen if As is gradually substituted by P or vice versa? Many related experimental studies have been introduced in the last section (Section 1.1.3), but no detailed theoretical studies have been published. Nevertheless, our previous study has extended the idea from K. Kuroki *et al.* with our experimental data to interpret the effect of P/As substitution in $R\mathrm{FeP}_{1-x}\mathrm{As}_x\mathrm{O}_{0.9}\mathrm{F}_{0.1}$.

As discussed above, the Fermi surface topology of LaFeAsO and LaFePO is different

from each other, especially from the viewpoint of the presence of the γ pocket, due to the different band structures in the $d_{X^2-Y^2}$ and d_{Z^2} bands. This feature can simply apply to other 1111 systems using the similar calculations [86]. When we consider the corresponding band structures as shown in Fig. 1.29, the energy level of the $d_{X^2-Y^2}$ band is above the energy level of the d_{Z^2} band above (π,π,z) with $z = 0 - \pi$ in LaFeAsO, while the energy of $d_{X^2-Y^2}$ band is below the d_{Z^2} band in LaFePO. If As is substituted by P, it is natural to expect that the energy of the $d_{X^2-Y^2}$ and d_{Z^2} bands will interchange, and as a result the γ pocket will shrink in size and finally vanish. We call this effect as *band crossover*. According to our experimental results in Ref. [82], the T-linear behavior of resistivity as well as the strong enhancement of Hall coefficient at low temperatures suggest that there is a change in the electronic states across P/As substitution, specifically, around As-content $x = 0.6$. We argue that these findings suggest that the band crossover happens around $x = 0.6$, and the change of the electronic states, due to the interchange of the two bands and the corresponding new Fermi surface topology, induces the anomalous behaviors in the transport properties.

In other words, RFeP$_{1-x}$As$_x$O$_{0.9}$F$_{0.1}$ exists two kinds of electronic states across P/As substitution. In the P-rich compounds, the band structure and Fermi surface look like those of RFePO, in which the Fermi surface around (π,π) is controlled by the d_{Z^2} band and the γ pocket is absent. In the As-rich compounds, the band structure and Fermi surface look like those of RFeAsO, in which the Fermi surface is dominated by the $d_{X^2-Y^2}$ band and the γ pocket is visible.

This interpretation can be supported by the plot of T_c against the exponent n as shown in Fig. 1.33. This plot is inspired by S. Ishida *et al.* [88] who have plotted T_c against n for Fe-As superconductors to express their general trend for the relationship between T_c and n. The data of oxygen deficient RFeAsO$_{1-y}$ and (Ba,K)Fe$_2$As$_2$ form the right line in the figure. On the other hand, the data of RFeP$_{1-x}$As$_x$O$_{0.9}$F$_{0.1}$ ($x \leq 0.6$) as well as P doped 122 systems form another line at the left hand side. This suggests

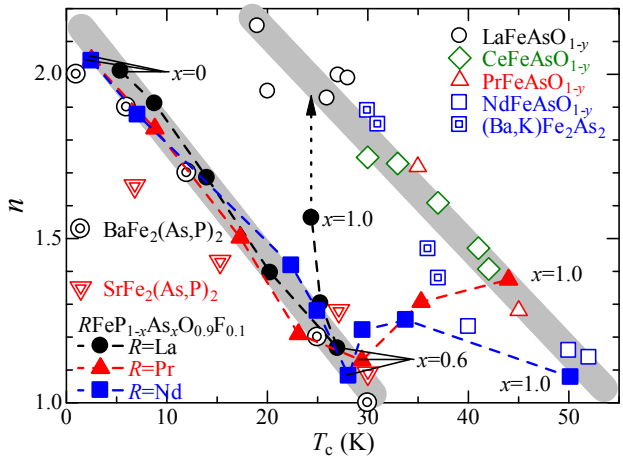

Figure 1.33: The plot of T_c against the exponent n of various iron-based superconductors [82].

there are two kinds of electronic states corresponding to the two kinds of the relationship between T_c and n. Moreover, for the samples of $R\mathrm{FeP}_{1-x}\mathrm{As}_x\mathrm{O}_{0.9}\mathrm{F}_{0.1}$ with $x > 0.6$, their data exist in between the two lines while the samples of $x = 1.0$ for $R =$ Pr and Nd lie on the right line[6]. It indicates the change of the electronic states from the RFePO-like state to the RFeAsO-like state across P/As substitution, which is consistent with our interpretation.

In summary, we propose that the band crossover can generally be found in P/As substituted 1111 systems. However, the evidence to support the picture about the band crossover and the two electronic states in P/As substituted 1111 systems is rather weak. Further investigations are necessary to confirm the reliability of this picture.

[6]The data of the sample of $x = 1.0$ for $R =$ La do not lie on the right line, but the data for $x > 0.6$ approach the data for $\mathrm{LaFeAsO}_{1-y}$ with increasing x.

1.4 Relation Between Structural Parameters and T_c in Iron-based Superconductors

In Fig. 1.33 from Section 1.3, we can see a general relation between T_c and the exponent n among Fe-As superconductors and Fe-P superconductors. Nevertheless, more general relations to T_c for iron-based superconductors can be found in their structural parameters.

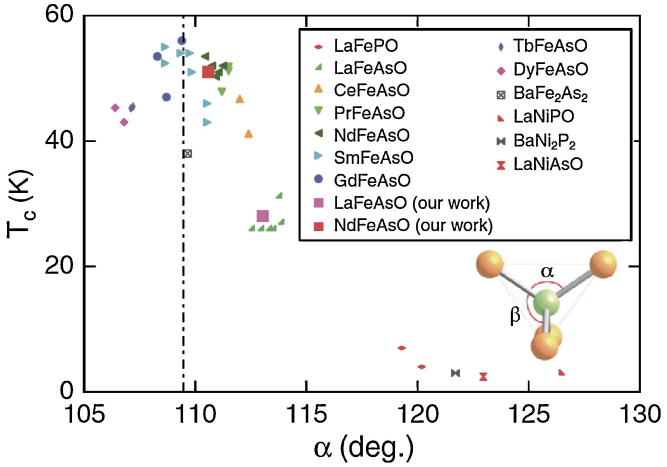

Figure 1.34: The plot of T_c against angle α of various iron-based superconductors [19].

Figure 1.34 shows the plot of T_c against angle α [19], which is defined as the angle between Fe-As/P-Fe bonds in Fe-As/P tetrahedral layers as illustrated in the inset. This plot indicates that iron-based superconductors approach to maximum T_c when the value of α reaches 109.5°, i.e. the Fe-As/P layers become perfect tetrahedra. It indeed suggests that there is a close relationship between T_c and the crystal structure. However, this plot cannot apply to some iron-based superconductors like LiFeAs with $T_c = 17$ K and $\alpha = 102.8°$, LiFeP with $T_c = 5$ K and $\alpha = 108.6°$ etc.

Another structural parameter is also proposed to be related to T_c: pnictogen height, or sometimes called anion height, which is defined as the distance between the Fe atoms and the As/P atoms inside the Fe-As/P layers as illustrated in Fig. 1.35. Figure 1.36 is

the plot of T_c against pnictogen height [89]. It shows that T_c reaches maximum when the value of pnictogen height is around 1.38 Å, and most of iron-based superconductors can be applied to this plot except some highly disordered systems like $LaFe_{0.89}Co0.11AsO$. In particular, it explains why T_c of Fe-As superconductors is generally higher than that of Fe-P superconductors. It is because the pnictogen height of Fe-As superconductors is typically greater and near 1.38 Å.

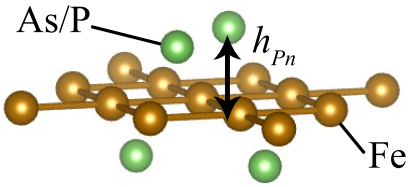

Figure 1.35: The schematic diagram of pnictogen height.

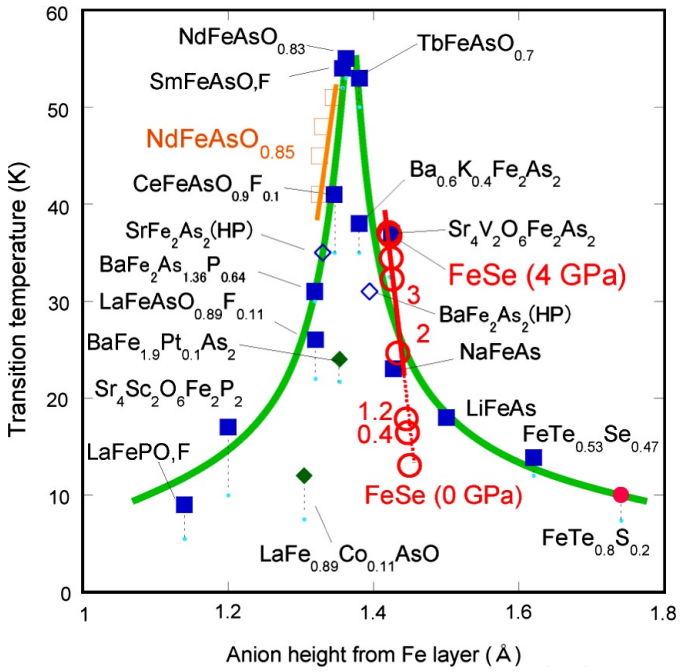

Figure 1.36: The plot of T_c against pnictogen height of various iron-based superconductors [89].

On the other hand, H. Kinouchi *et al.* have also plotted pnictogen height against Fe-Fe atoms distance to express the relationship between the structural parameters, nodeless/nodal SC and AFM [55], as illustrated in Fig. 1.37. It points out that the systems with the pnictogen height lower than ∼1.3 Å are nodal SC, those with the pnictogen height higher that ∼1.4 Å are nodeless SC, while those with the pnictogen height between 1.3 Å and 1.4 Å are AFM.

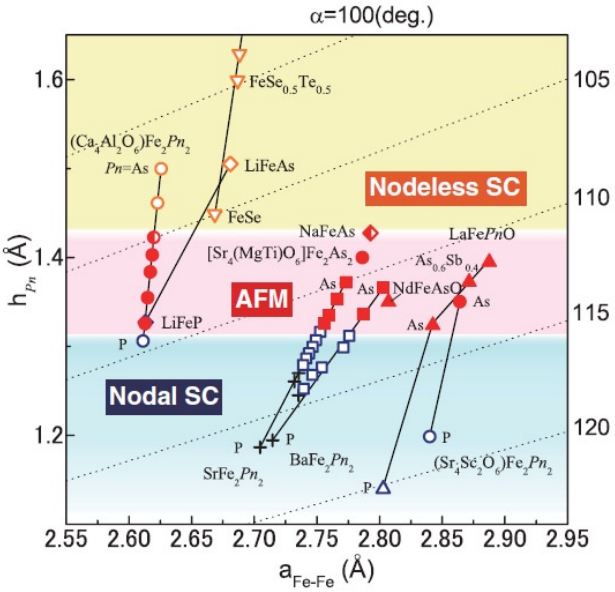

Figure 1.37: The plot of pnictogen height against Fe-Fe atoms distance of various iron-based superconductors [55].

Using the information that T_c can be characterized by the structural parameters, some corresponding theoretical studies have been performed to understand how the structural parameters modify the electronic properties of iron-based superconductors. For instance, K. Kuroki *et al.* have calculated the evolution of band structure and Fermi surface by varying the value of pnictogen height in 1111 systems [86], and the result is summarized in Fig. 1.38. It is found that low pnictogen height results in Fe-P type Fermi surface and nodal s±-wave, while high pnictogen height results in Fe-As type Fermi surface and nodeless s±-wave (as discussed in Section 1.2). It suggests that the value of

pnictogen height controls the band structure and the corresponding gap symmetry, and nodeless s±-wave induces high T_c in 1111 systems.

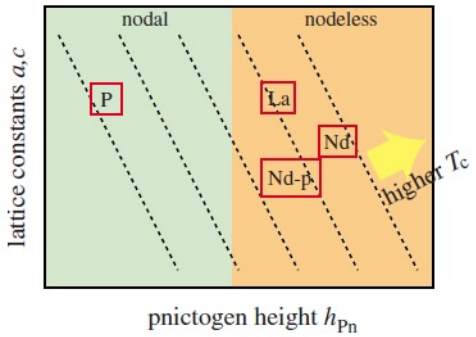

Figure 1.38: The schematic T_c phase diagram of 1111-type iron-based superconductors [86].

On the other hand, K. Suzuki *et al.*, also from K. Kuroki's group, have tried to modify the value of α to understand the two-dome structure in $LaFeAsO_{1-x}H_x$ [68]. It is realized that the two-dome structure can be revealed with a higher value of α, while the single-dome behavior in $SmFeAsO_{1-x}H_x$ can be revealed with a lower value of α.

In short, these findings provide a solid evidence that T_c, or the SC mechanism, is highly related to the structural parameters in iron-based superconductors. One should look up their relationship when studying iron-based superconductors.

1.5 Objectives

Due to proximity to SDW state, spin fluctuation is a possible candidate for the pairing force of Cooper pairs in SC for iron-based superconductors [90]. For example, it can be realized in the unified phase diagram of Ba122 (Fig. 1.6) which shows that the suppression of SDW state in their parent compounds can induce SC. However, orbital fluctuation is also proposed to be a possible candidate for the pairing glue [84]. There is still no consensus about the SC mechanism of iron-based superconductors.

Therefore, studying the phase diagrams of different types of iron-based superconduc-

tors provides a simple way to investigate the variations in the behaviors of iron-based superconductors upon doping, especially the relationship among SC, AFM and the corresponding Fermi surface nesting. 1111-type systems have a great potential to be studied because their phase diagrams are very complicated. A good example is LaFeAs(O,H) which two SC domes in the phase diagram, and the reappearance of the AFM phase in the overdoped region have been observed [62, 70]. The origin of these interesting behaviors has been argued in relation to spin or orbital fluctuations [65, 67, 68, 69, 70].

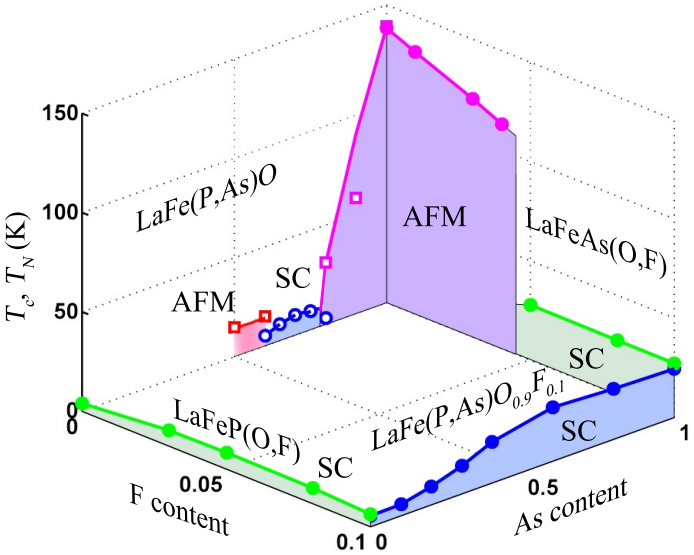

Figure 1.39: The phase diagram for summarizing the previous studies of $LaFeP_{1-x}As_xO_{1-y}F_y$ with $x = 0$ – 1 and $y = 0$ – 0.1 [56, 59, 73, 82].

Figure 1.39 summarizes the electronic behaviors of $LaFeP_{1-x}As_xO_{1-y}F_y$ with $x = 0$ – 1 and $y = 0$ – 0.1 [56, 59, 73, 82]. In our previous study of $LaFeP_{1-x}As_xO_{0.9}F_{0.1}$ [82], it has been found that T_c is maximum at $x = 0.6$, associated with T-linear behavior of resistivity and strong temperature dependence of Hall coefficient. This result suggests:

1. Spin fluctuation is strong at $x = 0.6$;

2. There are two kinds of electronic states across P/As substitution and the band crossover occurs around $x = 0.6$.

This finding has risen up some questions to be addressed. For example, what is the origin of the spin fluctuation at $x = 0.6$ as the fact that it is not proximity to the SDW state in the parent compound? Moreover, the band-crossover scenario is not very convincing for the existing data, and it cannot apply to the phase diagram of $LaFeAs_{1-x}P_xO$[7] reported by C. Wang *et al.* [72].

To solve the above problems, $LaFeP_{1-x}As_xO_{1-y}F_y$ with $y < 0.1$, namely 0 and 0.05, is chosen to be studied. Since the SDW state of $LaFeAsO_{1-y}F_y$ exists at $0 \leq x \leq 0.4$, lower values of y (i.e. lower F concentration) is nearer the SDW state than $y = 0.1$. Hence the interplay between AFM and SC, like the effect of spin fluctuations to SC, across P/As substitution is expected to be more easily observed.

On the other hand, the study for the series for $y = 0$ across P/As substitution provides a complete phase diagram to fully compare the behaviors in the series for $y = 0$. Together with the data of the series for $y = 0.05$, the evolution of the electronic states in $LaFeP_{1-x}As_xO_{1-y}F_y$ can be revealed through the construction of a x and y dependent phase diagram. The validity of the band-crossover scenario can thus be tested using this phase diagram.

[7] In the beginning of this study, the AFM phase around $x = 0.5$ observed by S. Kitagawa *et al.* [73] had not yet been reported.

Chapter 2

Experimental Methodology

2.1 Synthesis Environment

The processes of weighing and mixing the raw materials, as well as assembling the samples after synthesis were performed in a dry and Ar-filled glove box with the concentration of oxygen less than 10 ppm.

2.2 Synthesis of Precursors LaAs and LaP

The raw materials La powder (3N), As grains (6N) and P powder (5N) were used to synthesize LaAs and LaP by solid-state reaction method.

Since the commercial La powder was stored in paraffin oil, removal of the oil was necessary before the synthesis. The mixture of La powder and paraffin oil was first mixed with hexane in a breaker. The breaker was then set into an ultrasonic cleaner and then cleaned for 10 minutes. After the cleaning finished, hexane was exchanged immediately. The cleaning and the exchange of hexane would repeat for 3 – 4 times in order to completely remove the oil. Finally, the mixture was filtered by a filter paper, and the cleaned La powder was dried by putting into the pass box of the glove box and

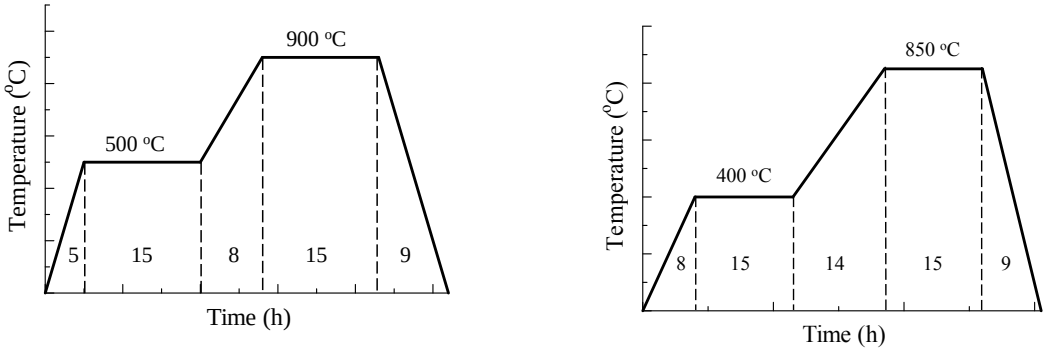

Figure 2.1: The annealing profiles of (Left) LaAs and (Right) LaP.

pumping to vacuum for about 3 hours. The dried La powder was stored in the glove box in order to prevent its oxidation.

La powder and As grains or P powder were mixed inside a quartz tube (with an inner diameter of 11 mm and an outer diameter of 13 mm) according to the stoichiometric ratio (1:1). The quartz tube was then pumped to high vacuum ($\sim 10^{-6}$ Torr) using a diffusion pump. The evacuated tube was sealed and annealed in a box furnace. LaAs was annealed at 500 °C for 15 hours and then 900 °C for 15 hours, while LaP was annealed at 400 °C for 15 hr and then 850 °C for 15 hours. The details of their annealing profiles could be referred in Fig. 2.1. It is worth to note that in order to prevent the breaking of the quartz tubes during annealing, the length of the tubes should be around 16 – 18 cm, while the weight of As (P) inside one tube should be less than 1.0 (0.4) g.

After annealing, the product was grounded to powder in the glove box for further use.

2.3 Synthesis of Polycrystalline $\mathbf{LaFeP_{1-x}As_xO_{1-y}F_y}$

Polycrystalline $LaFeP_{1-x}As_xO_{1-y}F_y$ was synthesized by solid-state reaction method. The precursors LaAs, LaP, Fe_2O_3 (4N), Fe (5N) and LaF_3 (3N) were used for the synthesis. They were weighed with the stoichiometric ratio according to the following chemical

equation:

$$\frac{x(3-y)}{3}\mathrm{LaAs}+\frac{(1-x)(3-y)}{3}\mathrm{LaP}+\frac{1-y-\delta}{3}\mathrm{Fe_2O_3}+\frac{1+2y+2\delta}{3}\mathrm{Fe}+\frac{y}{3}\mathrm{LaF_3}$$
$$+\frac{xy}{3}\mathrm{As}+\frac{y(1-x)}{3}\mathrm{P}$$
$$\longrightarrow \mathrm{LaFeP_{1-x}As_xO_{1-y-\delta}F_y}$$

The value of nominal x and y determined the ratio of P to As and O to F, respectively. δ indicated the oxygen deficiency. Because the precursors might partly be oxidized, the ratio of O to F might not be the same as the stoichiometric ratio. In order to increase the chance of successful F doping, δ was set to be 0.1. The total weight of the precursors should be around 1.0 – 1.2 g.

The precursors were then grounded for around 30 minutes. The powder mixture were put into a mount and pressed into a pellet with a diameter of 10 mm using an oil hydraulic press unit with pressure of 20 MPa. Finally, the pellet was sealed in an evacuated quartz tube (the same size as the one used in Section 2.2) under high vacuum. The sample was annealed at 1100 °C for 40 hours. The annealing profile was illustrated in Fig. 2.2 for further details.

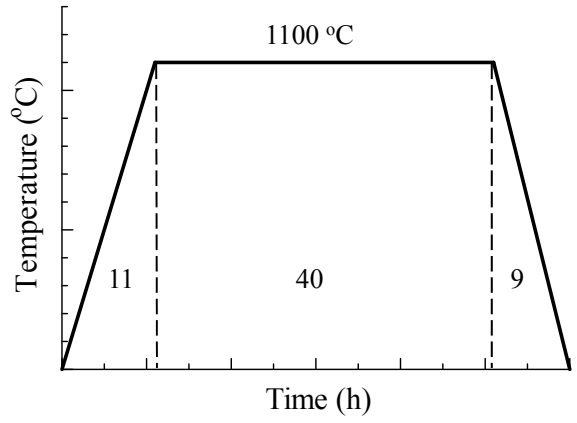

Figure 2.2: The annealing profile of $\mathrm{LaFeP_{1-x}As_xO_{1-y}F_y}$.

2.4 Measurements

2.4.1 Crystal Structural Analysis

Conventional powder X-ray diffraction was conducted by Rigaku MiniFlex and RINT-2000 with a source of Cu K_α radiation at room temperature. The lattice constants of the samples were determined by the least-square fitting of the corresponding Bragg peaks.

To obtain the structural information of the samples with higher accuracy, their diffraction patterns were obtained by using high-resolution synchrotron powder X-ray diffraction with the X-ray beam energy of 15 keV at BL-8A of Photo Factory (PF) in KEK, Tsukuba, Japan. The powder sample was inserted into a glass capillary tube with a diameter of 0.2 mm and a wall thickness of 0.01 mm. Temperature control of the samples was achieved by a He-flow cryostat. Different structural parameters of the corresponding diffraction patterns, including atomic positions, were determined by Rietveld analysis via the software RIETAN-FP [91].

2.4.2 Energy-dispersive X-ray Spectroscopy

Energy-dispersive X-ray spectroscopy (EDX) was applied to measure the elemental composition of the samples. One surface of an arbitrary-sized sample was first polished to be reasonably flat. The sample was then stuck on the sample holder with a flat surface using a carbon tape. The sample holder was evacuated in the chamber of a scanning electron microscope (SEM) in order to perform the measurements of EDX spectra. The EDX spectra from around 5 different points on each sample were obtained and the data were averaged to increase the accuracy.

2.4.3 Magnetic Susceptibility

Temperature dependent magnetic susceptibility of the samples was measured by a Quantum Design Magnetic Property Measurement System (MPMS, Model: MPMS-7). The

measurements were performed under zero-field cooling or field cooling with magnetic field of 10 Oe.

2.4.4 Electrical Resistivity

Electrical resistance of the samples was measured by a standard 4-point-probe method. The samples were first polished by a sandpaper to make them become roughly 1×1×5 mm^3 in shape. Gold wires were connected on the samples as electrodes with silver paint, in which the configuration was shown in Fig. 2.3. The whole setup was set in a long rod connected to the measurement system (computer-controlled current supplier and voltage meter). The rod was then put into a He tank to measure temperature dependence of the electrical resistance from room temperature down to 4.2 K. The current was usually set to 10 mA to keep the high accuracy of the data. Finally, the electrical resistivity ρ was calculated by the following equation:

$$\rho = R\frac{A}{l}, \tag{2.1}$$

where R is the electrical resistance, A is the cross-section area of the samples and l is the length between the electrodes for voltage measurements.

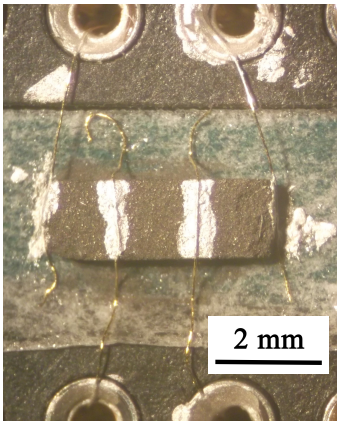

Figure 2.3: The connection of the electrodes in four-point-probe method.

2.4.5 Hall Effect

Hall effect measurements were conducted by inserting the samples in MPMS which controlled temperature and magnetic field. The electrodes were connected to the samples by a 4-point-probe method. Before the connection, the samples were polished by a sandpaper to be roughly 1.5×1.5×0.25 mm^3 in shape. The configuration of a sample was illustrated in Fig. 2.4. During the measurements, 10 mA of current was usually applied to the samples. After being stabilized in the selected temperatures ranged from room temperature to 5 K, the samples were scanned by magnetic field from -7 T to 7 T with the width of 0.5 T at each temperature. Since the value of Hall resistance was very small, 10 measurements were performed in each step of the field scan in order to increase the accuracy.

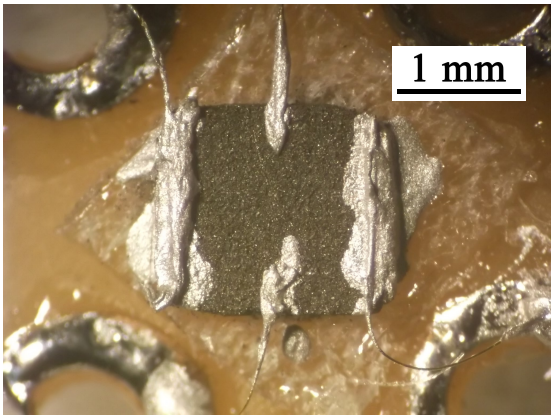

Figure 2.4: The connection of the electrodes for Hall measurements.

The reason why the field scan included negative fields will be given in the following. The resistance $R(H)$ obtained under the applied field H is not always equal to the Hall resistance $R_{xy}(H)$ since it may include the in-plane resistance $R_{xx}(H)$ due to imperfectness of the connection of the electrodes. That is,

$$R(H) = R_{xx}(H) + R_{xy}(H). \tag{2.2}$$

If the field is applied in an opposite direction, i.e. $-H$, $R(-H)$ becomes

$$R(-H) = R_{xx}(H) - R_{xy}(H), \tag{2.3}$$

since $R_{xx}(H) = R_{xx}(-H)$ and $R_{xy}(H) = -R_{xy}(-H)$ according to Lorentz force.

Hence, $R_{xy}(H)$ can be obtained from

$$R_{xy}(H) = \frac{R(H) - R(-H)}{2}. \tag{2.4}$$

Hall resistivity $\rho_{xy}(H)$ is given by

$$\rho_{xy}(H) = R_{xy}(H)\frac{Wd}{l}, \tag{2.5}$$

where W is the width of the samples, d is the thickness of the samples and l is the length between the electrodes for voltage measurements. Note that d should be small enough to obtain the good accuracy of the data.

Hall coefficient R_H is thus calculated by fitting the field dependence of $\rho_{xy}(H)$ with the following equation:

$$\rho_{xy}(H) = R_H H + \beta H^3, \tag{2.6}$$

where β is a constant. The H^3 term corresponds to the non-linear behavior in high field as well as the multiband effect.

2.4.6 Specific Heat

Specific Heat measurements were performed by using a Quantum Design Physical Property Measurement System (PPMS) in Nozue Group in Graduate School of Science, Osaka University. The sample holder for specific heat measurements with grease was first measured to obtain the temperature dependence of background specific heat. The surface of the samples was polished by a sandpaper to be reasonably flat and roughly smaller than 3×3 mm^2 in shape. The thickness of the samples was then adjusted by polishing so that the weight of the samples was adjusted to be about 10 mg. The thickness would be typically around 0.5 mm. Finally, the polished samples were mounted on the sample holder and the sample holder was inserted into the chamber of the PPMS to measure the temperature dependence of total specific heat. The specific heat of the samples was obtained by extracting the background specific heat from the total specific heat.

The specific heat C at low temperature could be described as

$$C/T = \gamma + \beta T^2, \tag{2.7}$$

where γ represents the electronic contribution and β represents the phonon contribution.

The values of γ and β could be determined by fitting the temperature dependence of C below 10 K.

Chapter 3

Results

3.1 Crystal Structure

Figure 3.1 shows the X-ray diffraction (XRD) spectra of $LaFeP_{1-x}As_xO$ ($y = 0$) and $LaFeP_{1-x}As_xO_{0.95}F_{0.05}$ ($y = 0.05$) at room temperature. All the bragg peaks observed in the diffraction patterns of all samples are able to be assigned within the tetragonal $P4/nmm$ symmetry. Although there is a minor impurity peak due to LaOF observed in some samples for $y = 0.05$, the portion of the main phase La1111 is still high, indicating La1111 is the majority of the samples.

The corresponding lattice constants a and c, pnictogen height h_{Pn} as well as angle α are calculated by Rietveld analysis [1]. The data is plotted in Figs. 3.2 and 3.3. Here h_{Pn} is defined as the vertical distance between As atoms and Fe atoms in Fe-As layers, and α is the angle of the tetrahedral in Fe-As layers. Both series of $y = 0$ and 0.05 show a linear increase in a, c and h_{Pn} with increasing As content x, while α decreases with increasing x. Since the size of As atoms is larger than that of P atoms, the increase is consistent with the Vegard's law [92], indicating that the As/P solution compounds are successfully prepared.

[1] The lattice constants are also calculated by the least-square fitting of the corresponding Bragg peaks, and the results are the same as Rietveld analysis.

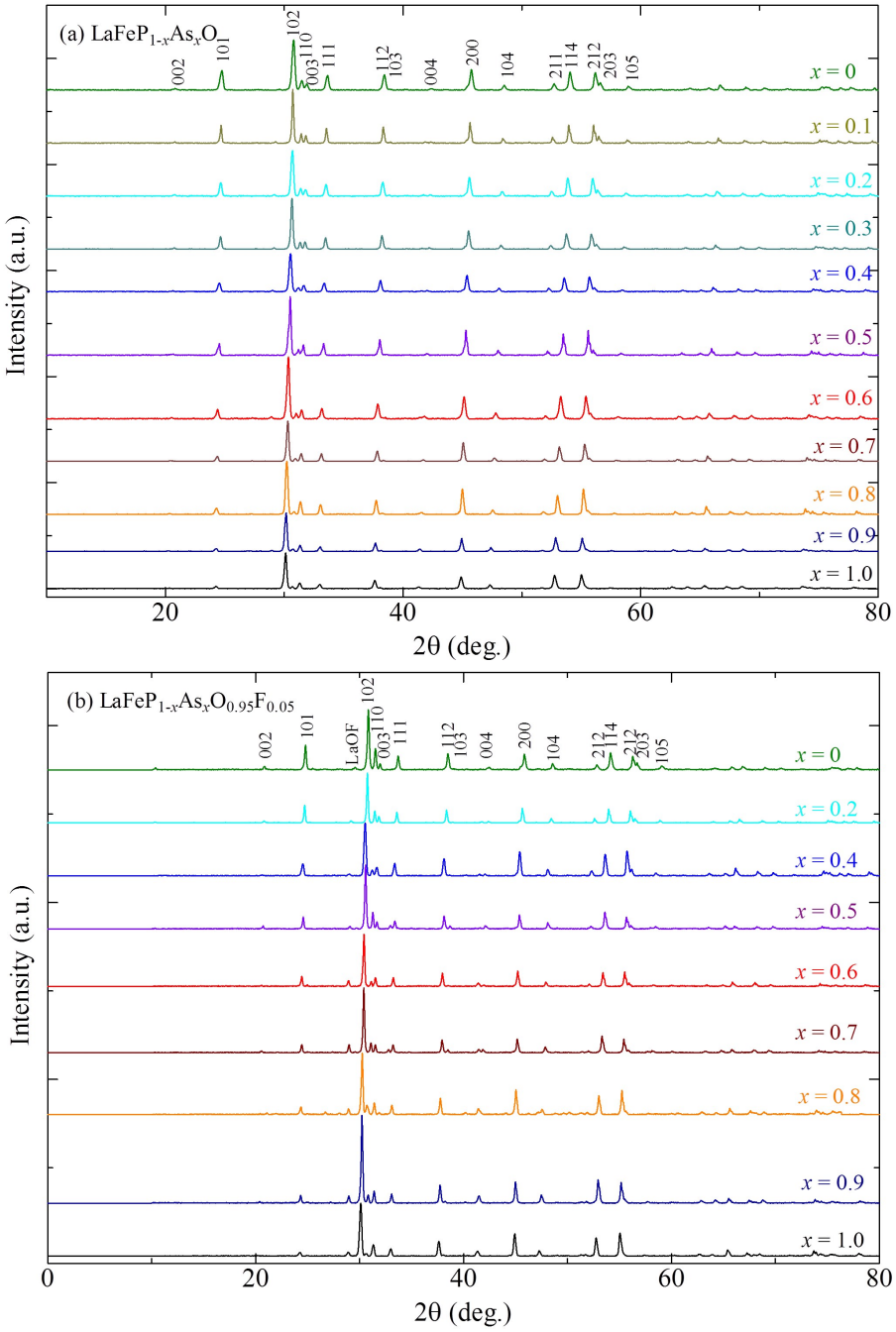

Figure 3.1: The X-ray diffraction spectra of $LaFeP_{1-x}As_xO_{1-y}F_y$ ($y = 0$, 0.05).

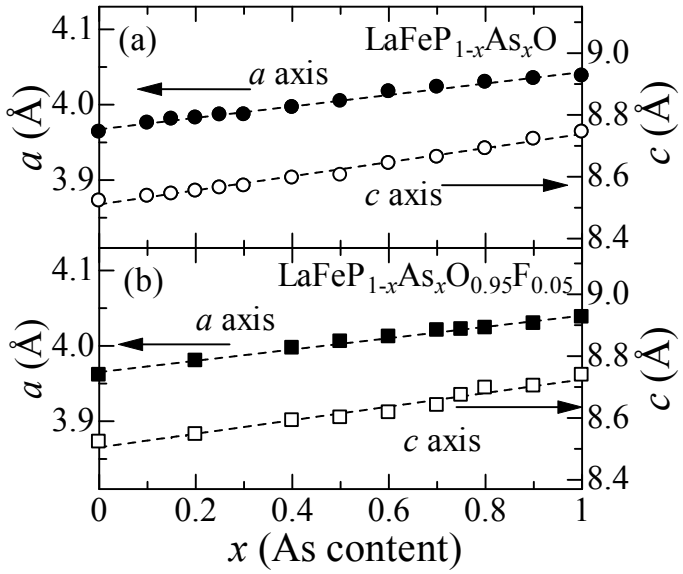

Figure 3.2: The x dependence of lattice constants a, c of (a) $LaFeP_{1-x}As_xO$ and (b) $LaFeP_{1-x}As_xO_{0.95}F_{0.05}$.

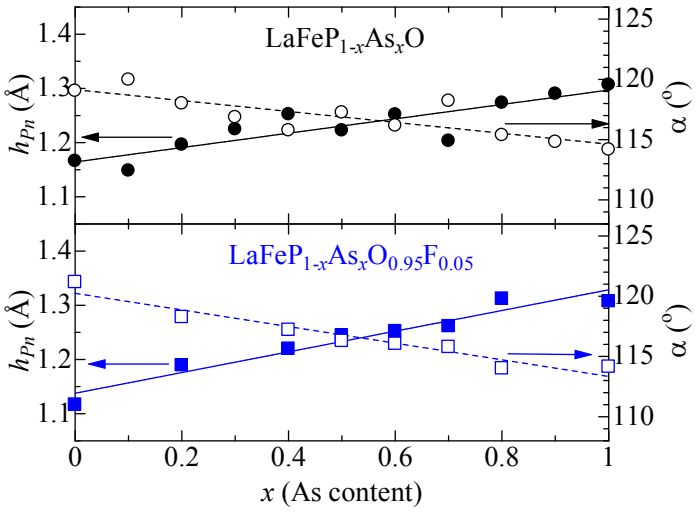

Figure 3.3: The x dependence of pnictogen height h_{Pn} and angle α of (a) $LaFeP_{1-x}As_xO$ and (b) $LaFeP_{1-x}As_xO_{0.95}F_{0.05}$.

Furthermore, the actual amount of F doping is also estimated by the Vegard's law. Comparing the data for nominal F concentration $y = 0$ - 0.1 (See Fig. 3.2 and Ref. [82], the lattice constants a and c continuously decrease with increasing y. In the previous report for $y = 0.1$ [82], we have roughly estimated the actual F concentration of ∼0.03 – 0.04 in the samples for $y = 0.1$ [82]. Assuming that the lattice constants depend linearly on the actual F concentration according to the Vegard's law, the actual F concentration is about 0.01 in the samples for $y = 0.05$. For the ease of further discussions, the nominal y will be used to represent the level of F doping.

As discussed in Section 1.1.2, AFM phase in iron-based superconductors is usually associated with structural transition. To investigate whether there is structural transition in $LaFeP_{0.6}As_{0.4}O$, which is found to be AFM with $T_N \sim 35$K [2], temperature dependence of the corresponding diffraction spectra were obtained. Figure 3.4 shows the spectra at the Bragg peak (220) at different temperatures. No peak splitting and broadening is observed down to 20 K, indicating that there is no structural transition above 20 K.

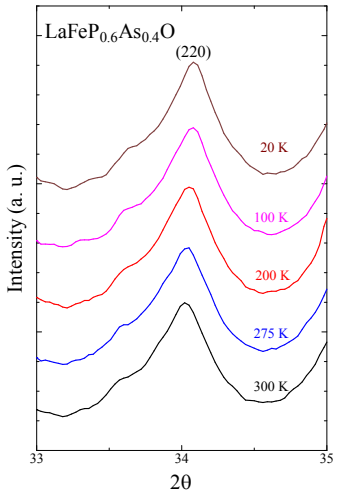

Figure 3.4: The XRD spectra of $LaFeP_{0.6}As_{0.4}O$ at the Bragg peak (220) at different temperatures.

[2] More details can be found in Section 4.1.

3.2 Elemental Composition

The Elemental composition of $LaFeP_{1-x}As_xO$ and $LaFeP_{1-x}As_xO_{0.95}F_{0.05}$ with $x \sim 0.3$ – 0.6 is obtained by the corresponding EDX spectra. Figure 3.5 shows a typical EDX spectrum of $LaFeP_{1-x}As_xO_{0.95}F_{0.05}$ ($x = 0.6$). The corresponding elements are able to be detected. In particular, the atomic ratio of As:P is calculated to confirm the existence of P/As substitution. The As content determined by EDX is compared with the nominal x, and the data are plotted in Fig. 3.6. Obviously the EDX determined value is very close to the nominal value, indicating the P/As substitution is successfully carried out.

Note that the actual F concentration cannot be estimated by EDX measurements because there are peaks for La and Fe near the energy of the F peak in the EDX spectrum. The amount of F content is based on the analysis from XRD measurements.

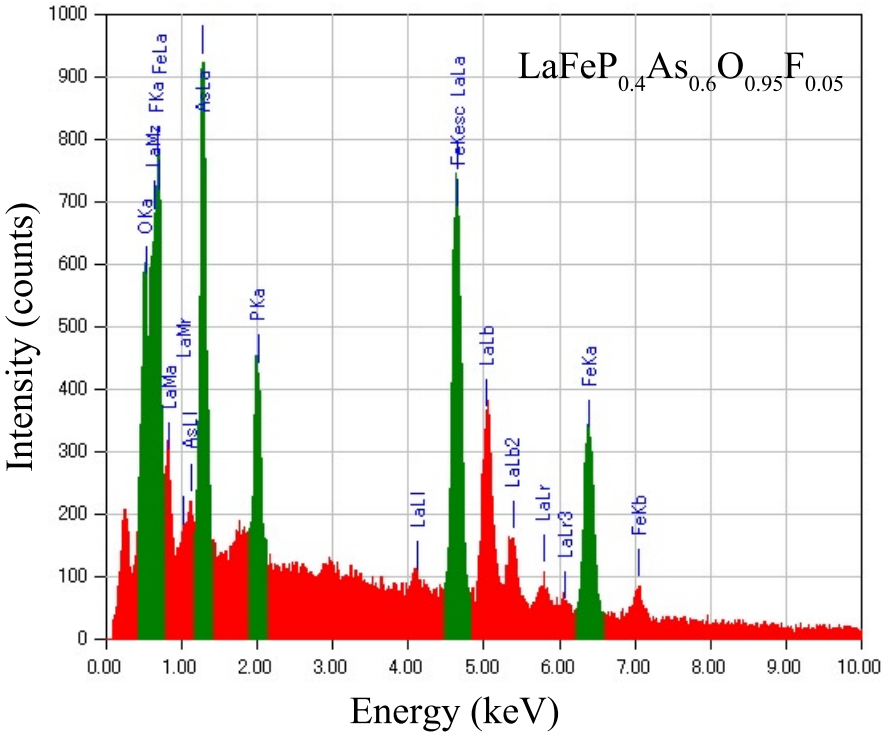

Figure 3.5: The typical EDX spectrum of $LaFeP_{0.4}As_{0.6}O_{0.95}F_{0.05}$.

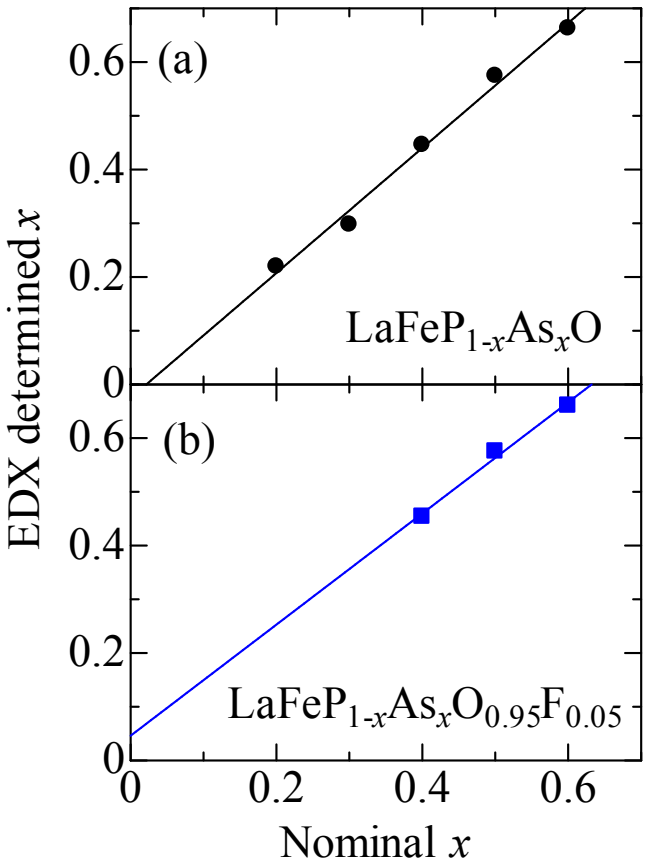

Figure 3.6: The plot of EDX determined As-content x against nominal x.

3.3 Magnetic Susceptibility and Electrical Resistivity

The temperature dependence of magnetic susceptibility for $y = 0$ and 0.05 is shown in Fig. 3.7. All the samples of $y = 0.05$ show a sharp drop due to Meissner effect, indicating the presence of SC phase transition. The SC volume fraction is approximately $> 70\%$. The samples of $y = 0$ with $x = 0$ – 0.25, 0.7 and 0.8 also show SC phase transition, but the SC volume fraction of the samples of $x = 0.7$ and 0.8 is much smaller. This is probably due to proximity of the SDW phase in $x = 1.0$. The samples of $x = 0.3$ – 0.6, 0.9 and 1.0 show no SC phase transition, indicating these samples are not SC.

The SC properties have been further investigated by electrical resistivity measurements. Figure 3.8 shows the temperature dependence of electrical resistivity for $y = 0$. The sudden drop of resistivity due to SC phase transition can be observed at $x = 0$ – 0.25, 0.7 and 0.8, which is consistent with the results of magnetic susceptibility measurements. The kink due to SDW phase transition is observed at $x = 0.9$ and 1.0 at temperature $T \sim 130$ K, which is consistent with the previous study [1]. Note that there is a strong upturn at $T < 60$ K at $x = 0.8$. It suggests that there is structural transition around $T = 60$ K, which is similar to the kink observed at $x = 0.9$ and 1.0. At $x = 0.3$ – 0.6, the behavior is rather metallic but not SC, which is again consistent with the results of magnetic susceptibility measurements. Nevertheless, the sample of $x = 0.5$ shows an upturn at low T (< 50K), which may be related to the recently reported AFM phase around $x = 0.5$ via ^{31}P-NMR technique [73]. Our collaborator, Kitaoka group in Graduate School of Engineering Science, Osaka University, has further studied in this region using ^{31}P-NMR technique [93]. AFM ordering with the maximum $T_N \sim$35 K at $x = 0.4$ is detected. More details about this AFM order will be discussed in Section 4.1.

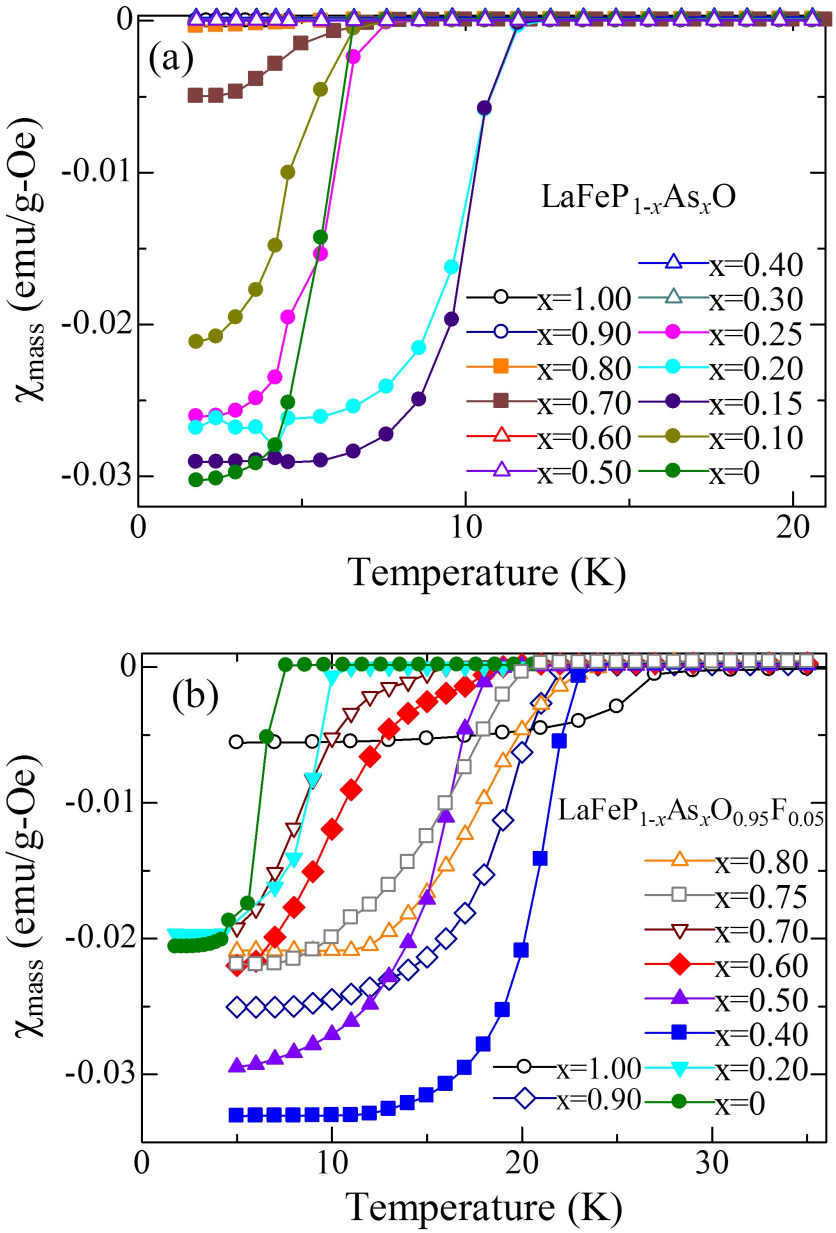

Figure 3.7: The temperature dependence of magnetic susceptibility of (a) $LaFeP_{1-x}As_xO$ and (b) $LaFeP_{1-x}As_xO_{0.95}F_{0.05}$.

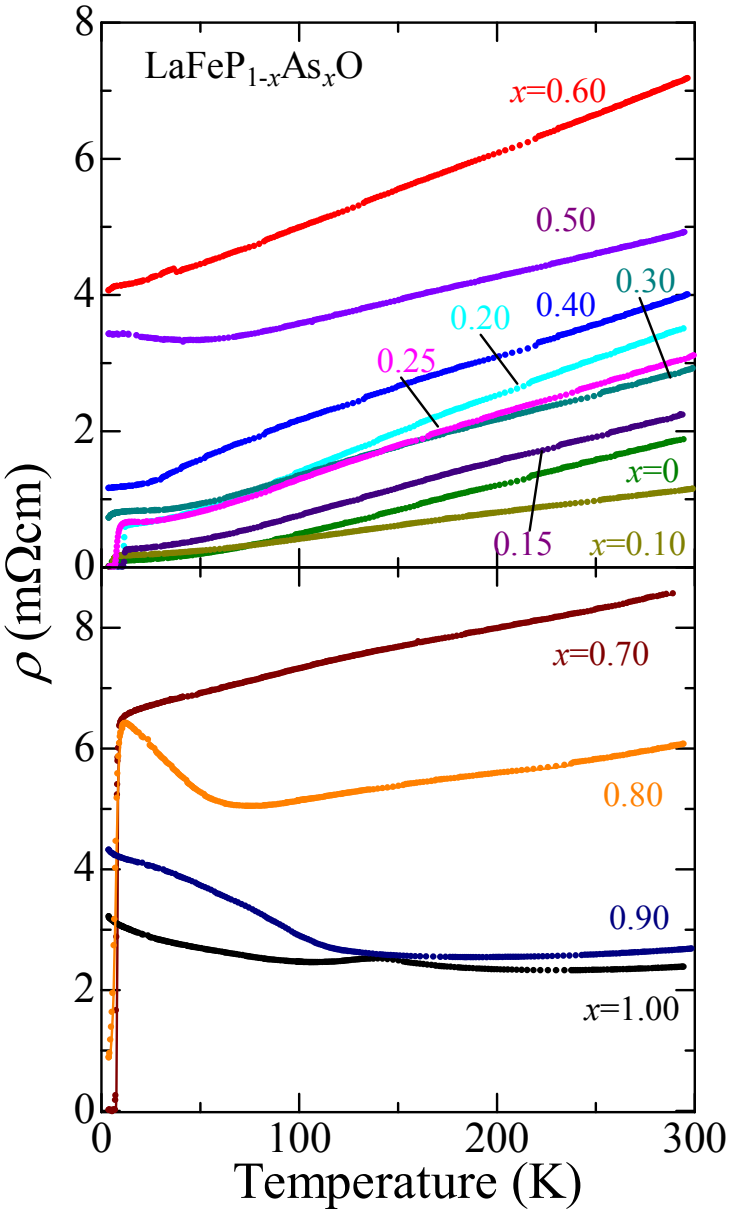

Figure 3.8: The temperature dependence of resistivity of $LaFeP_{1-x}As_xO$.

The temperature dependence of resistivity for $y = 0.05$ is shown in Fig. 3.9. All samples show SC phase transition at low temperatures and a typical metallic behavior in the normal state. Moreover, no anomalies are able to be found in the normal state.

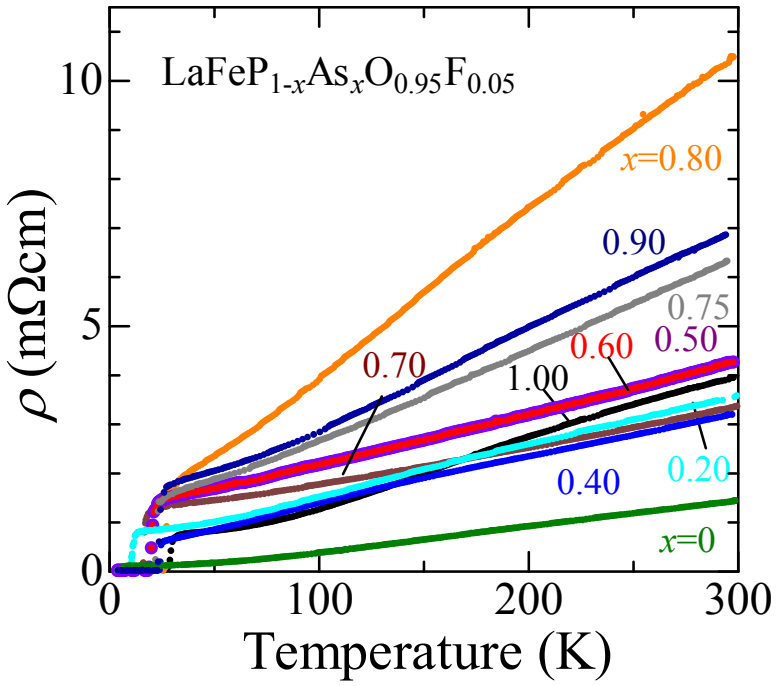

Figure 3.9: The temperature dependence of resistivity of $LaFeP_{1-x}As_xO_{0.95}F_{0.05}$.

Here it is noted that the behaviors of resistivity obtained in this polycrystalline study should be dominated by the *ab*-plane resistivity ρ_{ab} since it has been reported that the ratio of the *c*-axis resistivity ρ_c to ρ_{ab} is 20 – 200 in single crystalline 1111 samples revealed by upper critical field measurements [34, 94] as well as direct resistivity measurements [95]. However, it cannot be excluded that there is a possibility the ratio of the anisotropic resistivity may change during P/As substitution.

T_c and T_N of the samples are determined by T reaching zero resistivity and where the kink locates, respectively. The data for $y = 0$ is summarized in Fig. 3.10(a). It clearly shows that there are two SC domes and two AFM phases in the phase diagram. The values of T_c at $x = 0.6 – 0.8$ (SC1 dome) are consistent with the previous study [72].

The other SC dome at $x = 0$ – 0.3 (SC2 dome) is first found in the present study. The maximum T_c of SC2 dome is slightly higher ($\sim$12 K) than that of SC1 dome. Between the two SC domes, an AFM order (AFM2 phase) is observed, with T_N ranged from $\sim$15 K to 35 K. Another AFM phase (AFM1 phase) is also observed above $x = 0.8$ through the resistivity data and the NMR data [73]. Here the AFM order is accompanied with a structural phase transition as evidenced by the kink in the resistivity data. The values of T_N, between $\sim$50 K – 140 K, in AFM1 phase are much higher than that in AFM2 phase.

Figure 3.10(b) shows the x-dependence of T_c for $y = 0.05$. A local minimum of $T_c(x)$ is found around $x = 0.6$, giving a double-peak structure. The data of $y = 0.1$ [82] is also plotted in Fig. 3.10(c) for comparison. There is only a single peak at $x = 0.6$. These results suggest that the two SC domes found at $y = 0$ merge with each other when y increases.

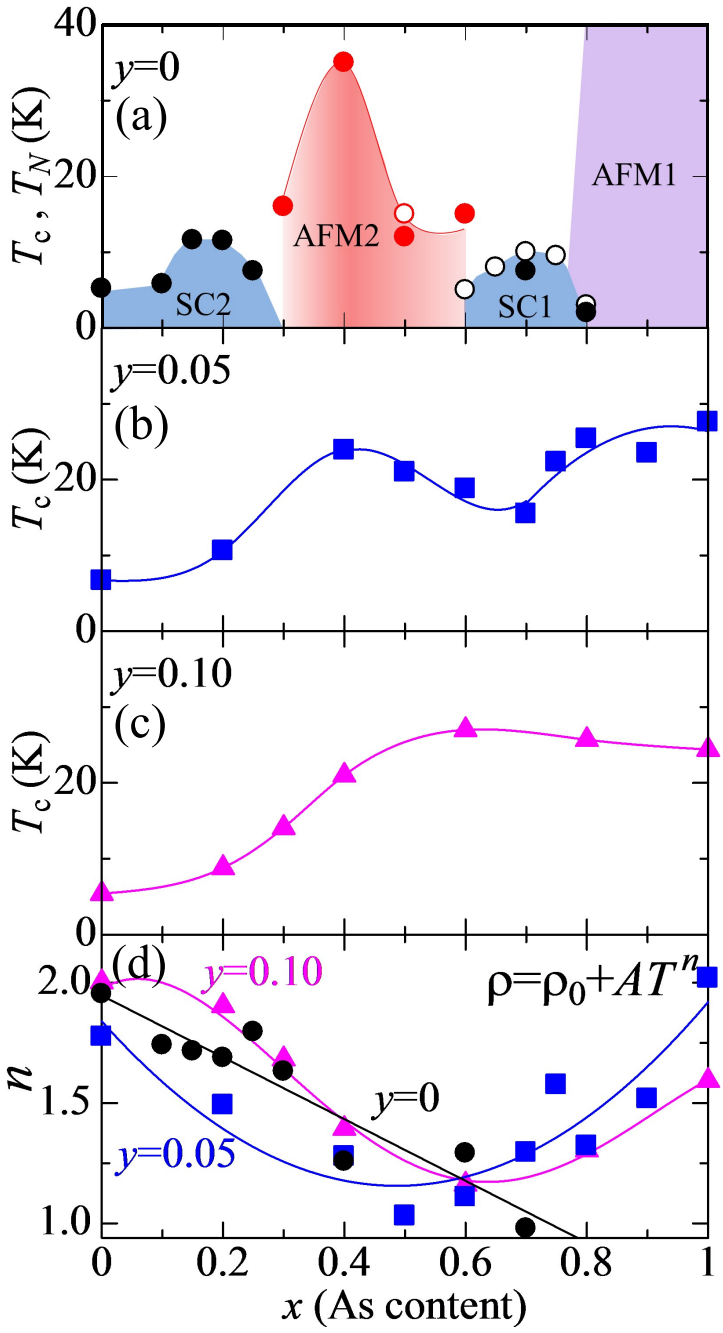

Figure 3.10: The x dependence of (a) critical temperature T_c, Neel temperature T_N of $LaFeP_{1-x}As_xO$, (b) T_c of $LaFeP_{1-x}As_xO_{0.95}F_{0.05}$, (c) T_c of $LaFeP_{1-x}As_xO_{0.9}F_{0.1}$, and (d) the exponent n in $\rho(T) = \rho_0 + AT^n$ of $LaFeP_{1-x}As_xO_{1-y}F_y$, respectively. The open circles are the data by C. Wang *et al.* [72] and S. Kitagawa *et al.* [73].

To understand the Fermi-liquid behavior of the samples, the temperature dependence of resistivity is extracted from the resistivity data $\rho(T)$. It can be achieved by fitting the data using $\rho(T) = \rho_0 + AT^n$ [Equation (1.1)] to obtain the value of n of each sample. The fitting has been performed above T_c and below 100 K to avoid the strong phonon contribution at high temperatures.

The data of n for $y = 0$ – 0.1 with various values of x is illustrated in Fig. 3.10(d). For $y = 0$, n changes gradually from 2 to 1 when x increases to 0.7. Note that the data of $x = 0.5$, 0.8 – 1.0 are not suitable for fitting because of the upturn at low T. Roughly speaking, the value of n is close to 2 in SC2 dome while that is $\sim$1 in SC1 dome. It suggests that the behavior of $\rho(T)$ near SC2 dome is described by Fermi liquid while that near SC1 dome is non-Fermi liquid. Since the sample of $x = 0.7$ is near the boundary of SDW phase, the gradual decrease in n with increasing x suggests the existence of a QCP around $x = 0.7$. This point of view is consistent with the previous theoretical prediction [96], which has predicted the suppression of SDW and the occurrence of the QCP due to P doping in LaFe(As,P)O. Meanwhile, the value of n approaches 1 around $x = 0.6$, and 2 at $x = 0$ and 1.0 for both series of $y = 0.05$ and 0.1. It indicates that both systems exhibit non-Fermi-liquid behavior around $x = 0.6$, while Fermi-liquid behavior is observed around $x = 0$ and 1.0.

Comparing the data of T_c and the exponent n in Fig. 3.10, it is clear that the enhancement of T_c in the low-x region (around the location of SC2 dome) is associated with the decrease in n from 2, which indicates that the system changes from Fermi liquid to non-Fermi liquid. This change of n is correlated to the increase in spin fluctuations, which has been observed by NMR experiments [85, 93]. Therefore, the SC in low-x region is more likely to be induced by spin fluctuations, which is consistent with our previous study in Ref. [82].

In contrast, the relationship between n and T_c is more complicated in the larger x (As-rich) region. For $y = 0$, SC disappears and AFM ordering arises even though the

value of n keeps decreasing at $0.3 \leq x \leq 0.6$. At $x = 0.7$, the value of n approaches to 1 but T_c is lower than the one found in $x \sim 0.2$. For $y = 0.05$, T_c is suppressed at $x = 0.5 - 0.7$ regardless of the decrease in n. From $x = 0.8$ to 1.0, T_c increases again but the value of n also increases. Hence it is concluded that there is no clear correlation between n and T_c in larger x (As-rich) region.

3.4 Hall Effect

Because the measurements of resistivity have shown some complicated behaviors, especially the non-Fermi-liquid metallic behavior in AFM2 phase, Hall coefficient R_H of this system is desired due to its sensitivity to the change of electronic states. In order to obtain R_H of each sample, the field dependence of Hall resistivity ρ_{xy} has been measured at different temperatures. All the data for $y = 0$ and 0.05 are plotted in Figs. 3.11 – 3.27.

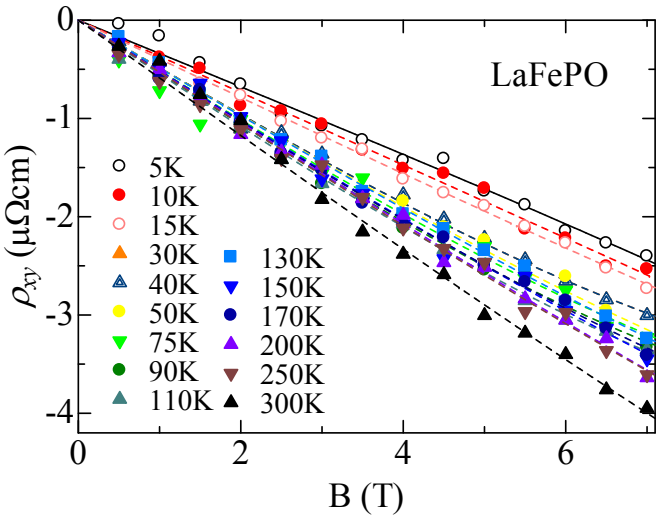

Figure 3.11: The field dependence of Hall resistivity ρ_{xy} of LaFePO.

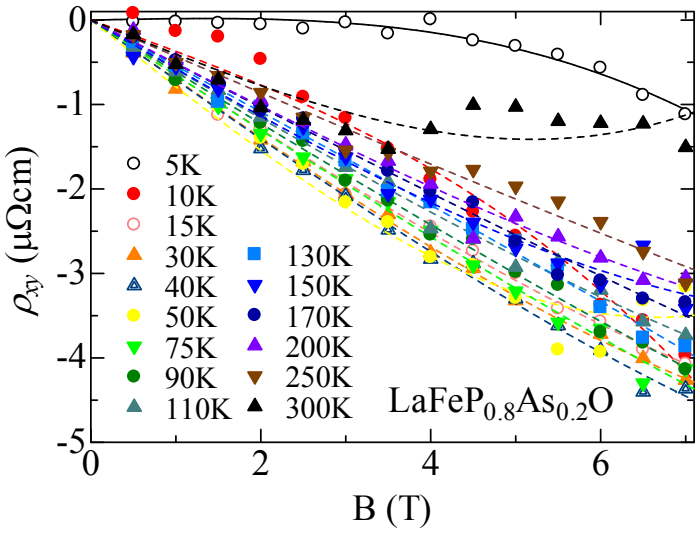

Figure 3.12: The field dependence of Hall resistivity ρ_{xy} of $LaFeP_{0.8}As_{0.2}O$.

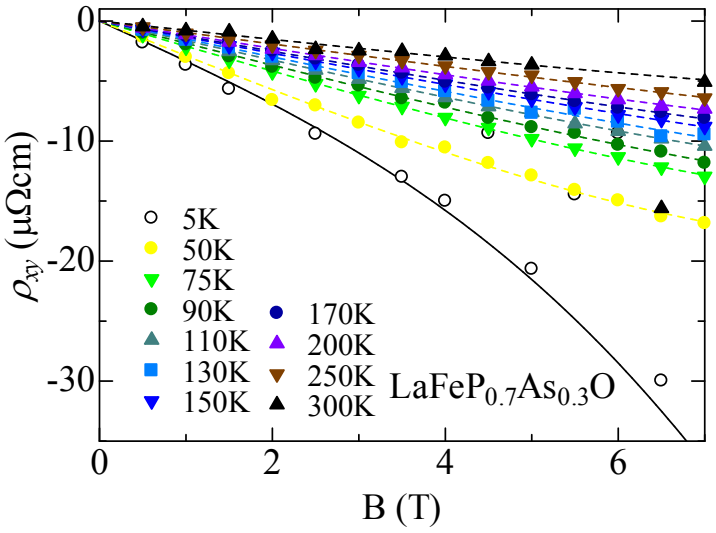

Figure 3.13: The field dependence of Hall resistivity ρ_{xy} of $LaFeP_{0.7}As_{0.3}O$.

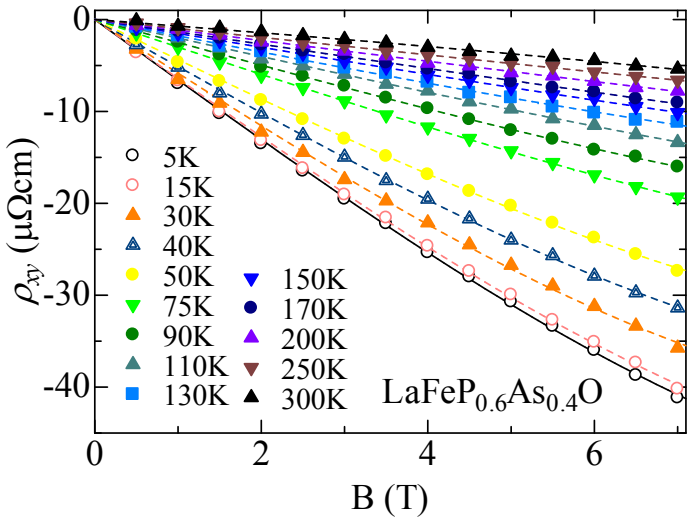

Figure 3.14: The field dependence of Hall resistivity ρ_{xy} of $LaFeP_{0.6}As_{0.4}O$.

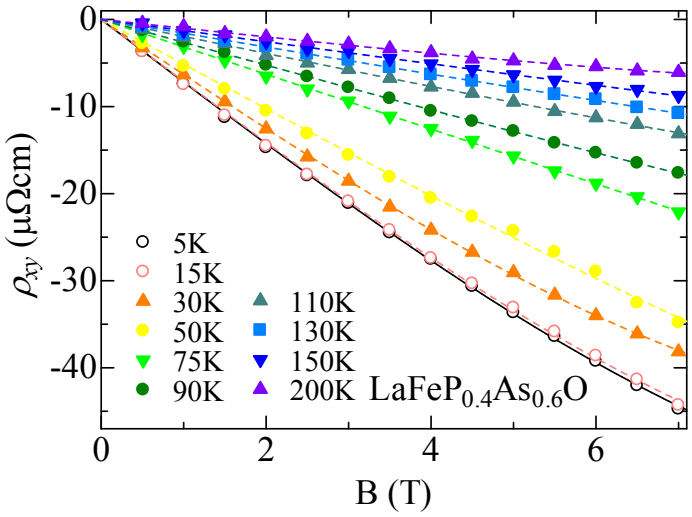

Figure 3.15: The field dependence of Hall resistivity ρ_{xy} of $LaFeP_{0.4}As_{0.6}O$.

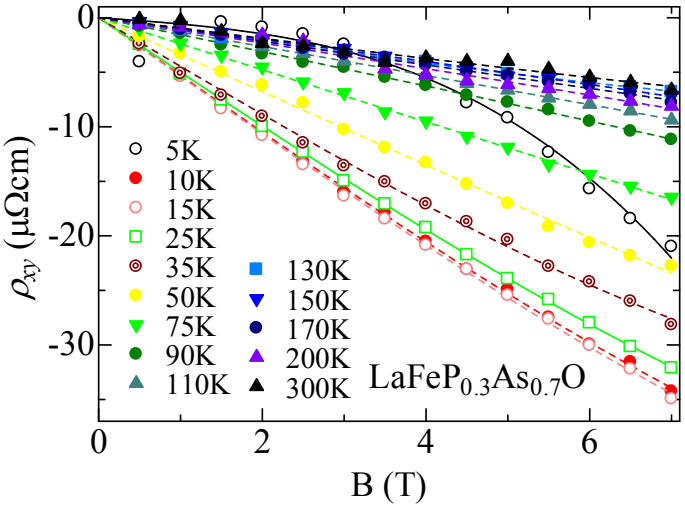

Figure 3.16: The field dependence of Hall resistivity ρ_{xy} of $LaFeP_{0.3}As_{0.7}O$.

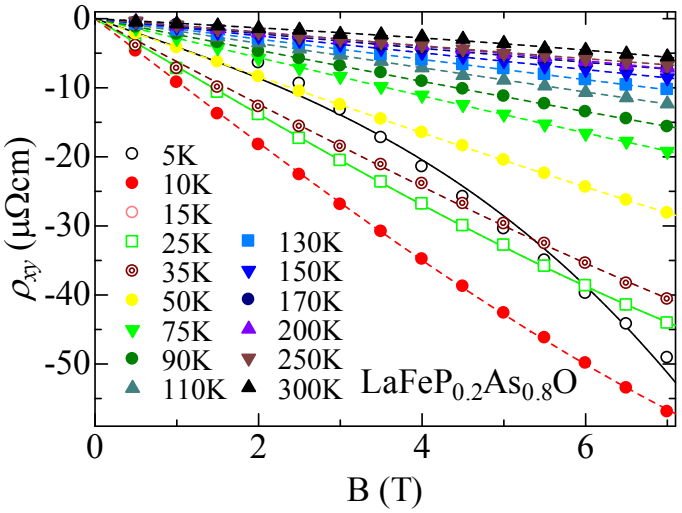

Figure 3.17: The field dependence of Hall resistivity ρ_{xy} of $LaFeP_{0.2}As_{0.8}O$.

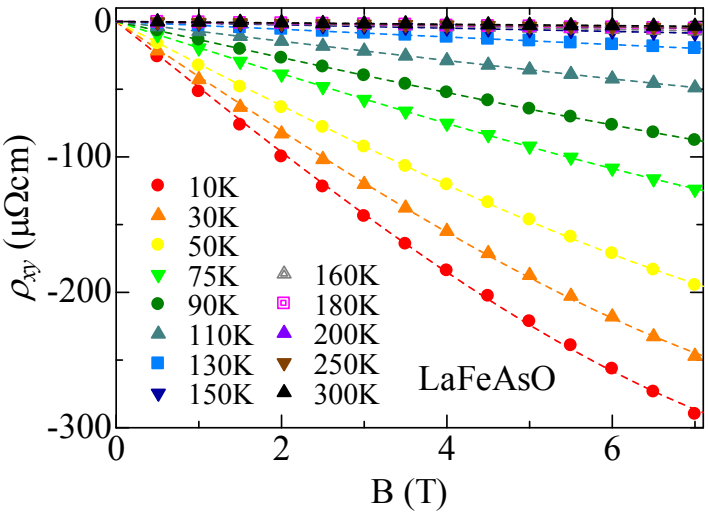

Figure 3.18: The field dependence of Hall resistivity ρ_{xy} of LaFeAsO.

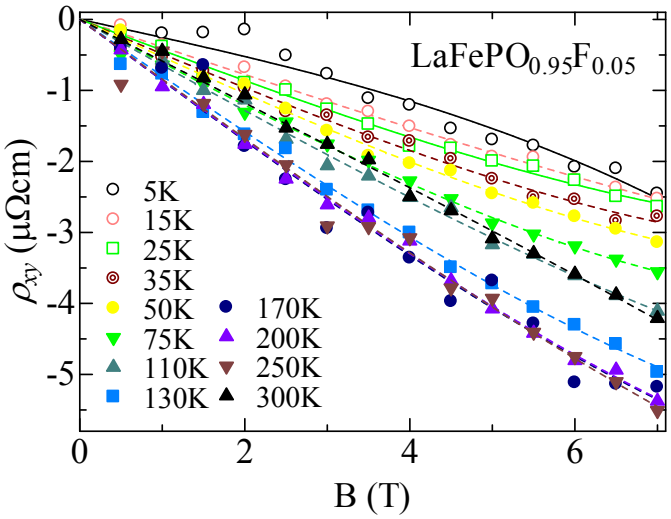

Figure 3.19: The field dependence of Hall resistivity ρ_{xy} of $LaFePO_{0.95}F_{0.05}$.

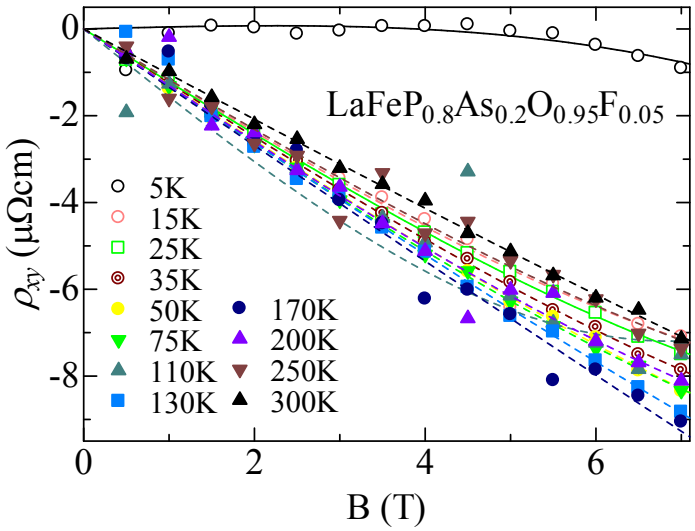

Figure 3.20: The field dependence of Hall resistivity ρ_{xy} of $LaFeP_{0.8}As_{0.2}O_{0.95}F_{0.05}$.

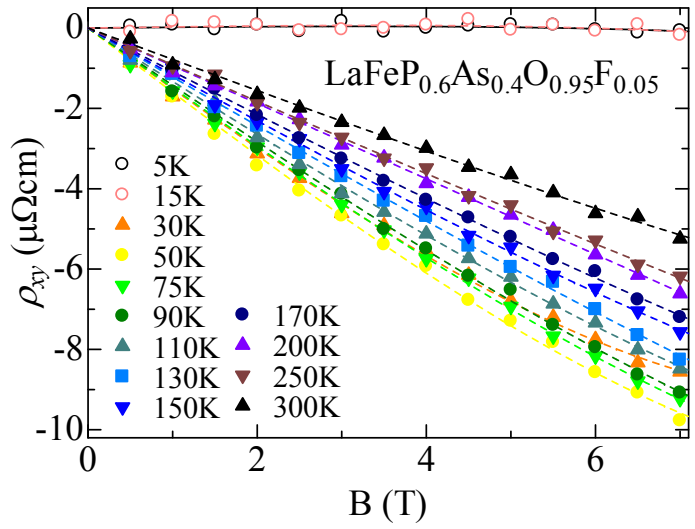

Figure 3.21: The field dependence of Hall resistivity ρ_{xy} of $LaFeP_{0.6}As_{0.4}O_{0.95}F_{0.05}$.

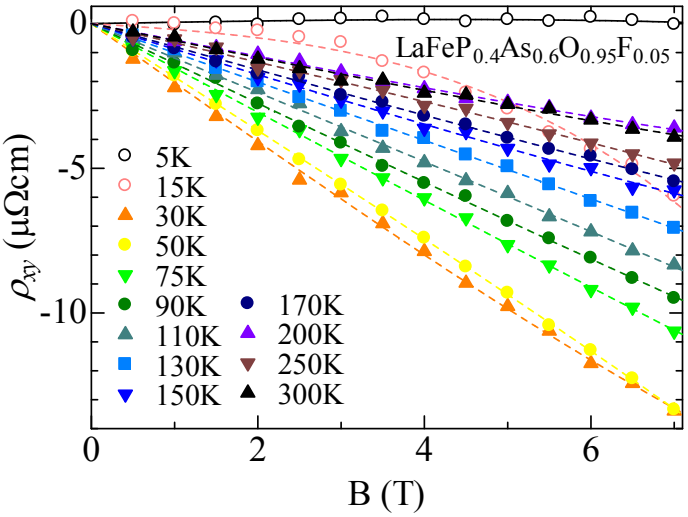

Figure 3.22: The field dependence of Hall resistivity ρ_{xy} of $LaFeP_{0.4}As_{0.6}O_{0.95}F_{0.05}$.

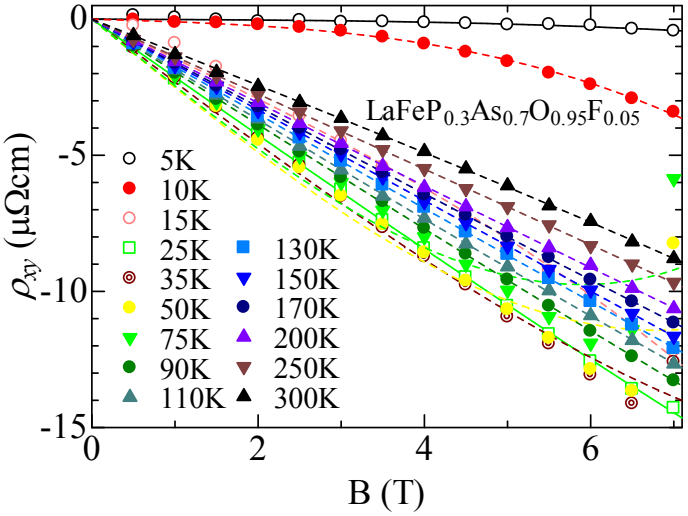

Figure 3.23: The field dependence of Hall resistivity ρ_{xy} of $LaFeP_{0.3}As_{0.7}O_{0.95}F_{0.05}$.

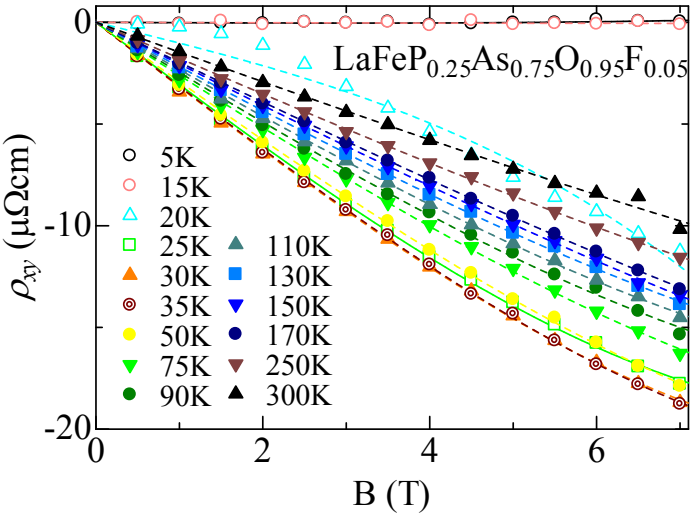

Figure 3.24: The field dependence of Hall resistivity ρ_{xy} of $LaFeP_{0.25}As_{0.75}O_{0.95}F_{0.05}$.

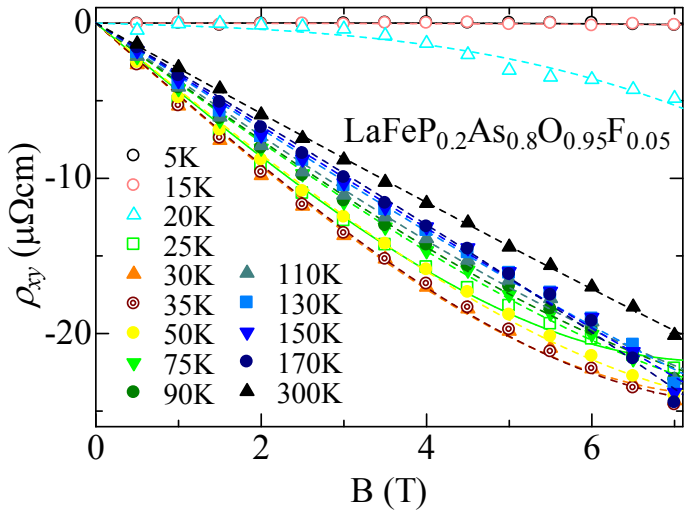

Figure 3.25: The field dependence of Hall resistivity ρ_{xy} of $LaFeP_{0.2}As_{0.8}O_{0.95}F_{0.05}$.

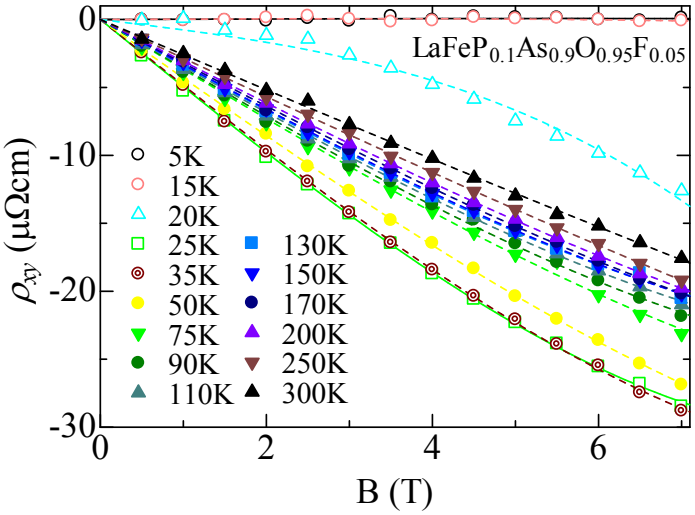

Figure 3.26: The field dependence of Hall resistivity ρ_{xy} of $LaFeP_{0.1}As_{0.9}O_{0.95}F_{0.05}$.

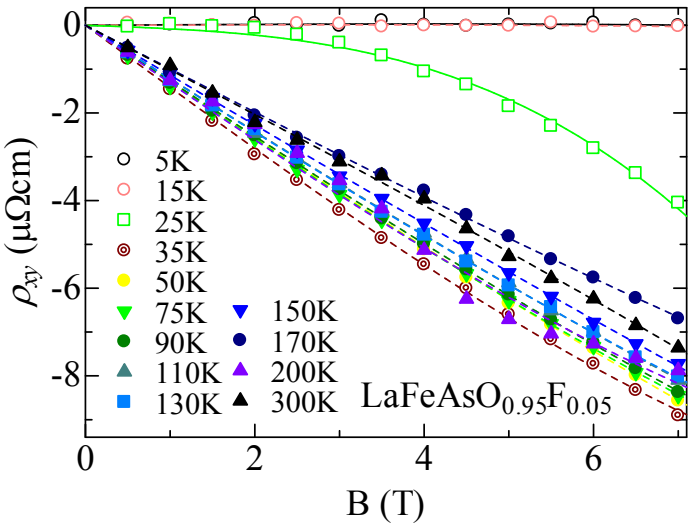

Figure 3.27: The field dependence of Hall resistivity ρ_{xy} of $LaFeAsO_{0.95}F_{0.05}$.

For single-carrier materials, it is clear that ρ_{xy} is proportional to H for sufficiently low field. Iron-based superconductors, however, are known as multiband materials. There will be different kinds of contribution to conduction carriers from different bands. Since the carriers are either electrons or holes, the field dependence of ρ_{xy} can be approximately described by a two-band model [97], which gives

$$\rho_{xy} = \frac{1}{|e|} \frac{n_h \mu_h^2 - n_e \mu_e^2 + (\mu_h \mu_e)^2 (n_h - n_e) H^2}{(n_h \mu_h + n_e \mu_e)^2 + (\mu_h \mu_e)^2 (n_h - n_e)^2 H^2} H, \tag{3.1}$$

where n_h (n_e) are the number densities of holes (electrons), $\mu_h = |e|\tau_h / m_h$ ($\mu_e = |e|\tau_e / m_e$ are the motilities of holes (electrons), τ_h (τ_e) are the relaxation rates of holes (electrons) and m_h (m_e) are the effective masses of holes (electrons). Therefore, multiband materials like iron-based superconductors may induce non-linear behaviors in field dependence of ρ_{xy} if the charge density and/or the mobility of electrons and holes are comparable, like the H^3 term included in the fitting equation (2.6).

In this study, most of the data in the normal state show negative values and mostly linear dependence with the applied field, suggesting that the majority of the charge carriers are electrons. In the SC state, ρ_{xy} is so low to be measured accurately, so that it usually shows rather no field dependence and gives low values in R_H in the later calculations. Sometimes ρ_{xy} in the SC state is increasing with the applied field when the applied field exceeds a certain value. It may be because the field exceeds the critical field so that SC is suppressed.

On the hand, the field dependence of ρ_{xy} shows essentially non-linear behaviors when T is just above T_c. It may be due to carrier density fluctuations near T_c.

Temperature dependence of R_H for $y = 0$, 0.05 and 0.1 [82] is illustrated in Fig. 3.28. The data of $y = 0.1$ is shown for comparison. All the values of R_H in the normal state are negative as expected.

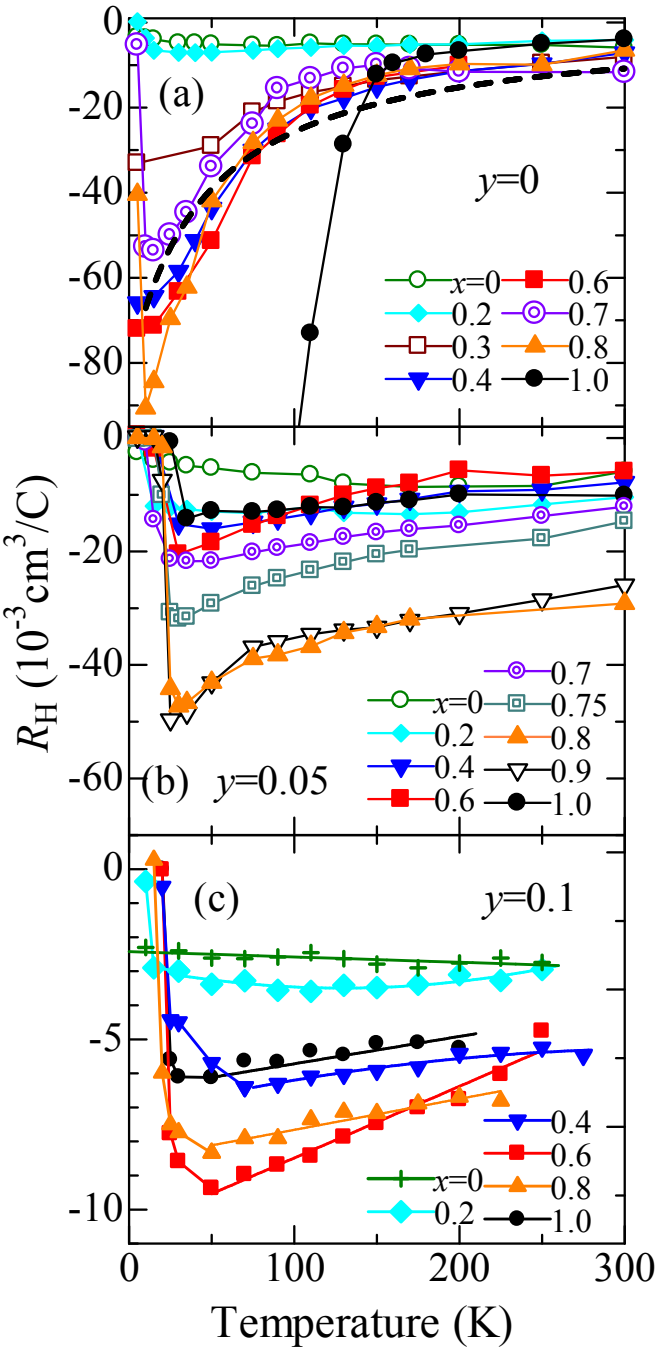

Figure 3.28: The temperature dependence of the Hall coefficient R_H of (a) $LaFeP_{1-x}As_xO$, (b) $LaFeP_{1-x}As_xO_{0.95}F_{0.05}$ and (c) $LaFeP_{1-x}As_xO_{0.9}F_{0.1}$. The dashed curve in (a) is the fitting of the data for $x = 0.4$ as an example, by using the equation $R_H = -\alpha_0/(T+\Theta)$.

For $y = 0$, a large drop of R_H is observed in LaFeAsO ($x = 1$) around 140 K. This indicates the appearance of SDW which is consistent with the $\rho(T)$ data and the previous studies [72, 98]. For the samples in SC1 dome ($x = 0.7$, 0.8), R_H shows very strong temperature dependence such that $|R_H|$ is strongly enhanced at low temperatures and has a sudden drop at T_c. Surprisingly, in the non-SC region ($x = 0.3$ – 0.6), their R_H also shows a similar T dependence to that in SC1 state, while the temperature dependence of R_H is much weaker for the samples of $x = 0.2$ and rather temperature-independent for $x = 0$.

For $y = 0.05$, the temperature dependence of R_H is gradually enhanced from $x =$ 0 – 0.7 instead of the rapid enhancement from $x = 0.2$ to 0.8 in the samples of $y = 0$. When x increases to around 0.8, the temperature dependence of R_H becomes larger and comparable to the results of $x = 0.3$ – 0.8 in the samples of $y = 0$. Compared with y = 0, the change of the temperature dependence of R_H is relatively mild for $y = 0.05$. More precisely, the temperature dependence of R_H is gradually enhanced from $x = 0.6$ to 0.8 for $y = 0.05$. At $x = 1.0$ ($LaFeAsO_{0.95}F_{0.05}$), the temperature dependence of R_H becomes as small as the low-x region, which is consistent with the previous study [99].

For $y = 0.1$, however, the temperature dependence of R_H is rather weak compared to the series of $y = 0$ and 0.05, as shown in Fig. 3.28(c). Nevertheless, the evolution of the temperature dependence among various values of x is able to be observed, and it shows that the temperature dependence is the strongest at $x = 0.6$.

To visualize these complex behaviors of R_H in various values of y, the doping dependence of R_H at 50 K for all y is plotted in Fig. 3.29. When the temperature dependence of R_H is stronger, $|R_H|$ at low temperatures, namely 50 K, will become larger. Hence the temperature dependence of R_H of each sample can be simply compared by looking at the value of $|R_H|$ at 50 K. Here the data at 50 K are chosen because 50 K is sufficiently low to show the enhancement of $|R_H|$ and reasonably above T_c to avoid the effect of carrier density fluctuations near the SC transition. Briefly summarizing the data, the

doping dependence of each y series, as described above, is well reproduced. Moreover, the strength of the temperature dependence of R_H is able to be compared among samples. For instance, the value of $|R_H|$ at 50 K has a peak at $x = 0.6$ for $y = 0$ and 0.1, while that is maximum around $x = 0.8$ – 0.9 for $y = 0.05$.

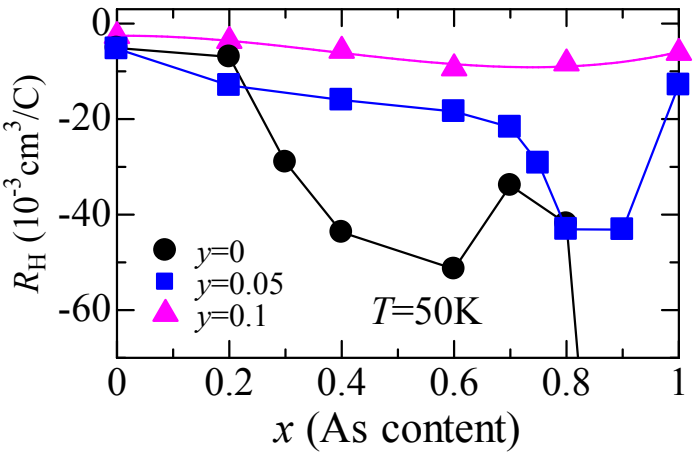

Figure 3.29: The x dependence of the Hall coefficient R_H of $LaFeP_{1-x}As_xO_{1-y}F_y$.

3.5 Specific Heat for $y = 0$

To further understand the electronic behavior of the samples for $y = 0$, especially the emergence of AFM2 phase, the specific heat C has been measured. Temperature dependence of C (or C/T) of the samples for $y = 0$ is shown in Figs. 3.30 – 3.34.

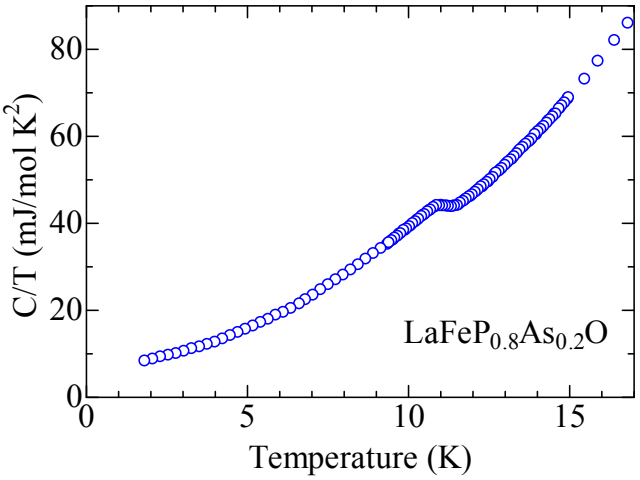

Figure 3.30: The temperature dependence of specific heat C/T of $LaFeP_{0.8}As_{0.2}O$.

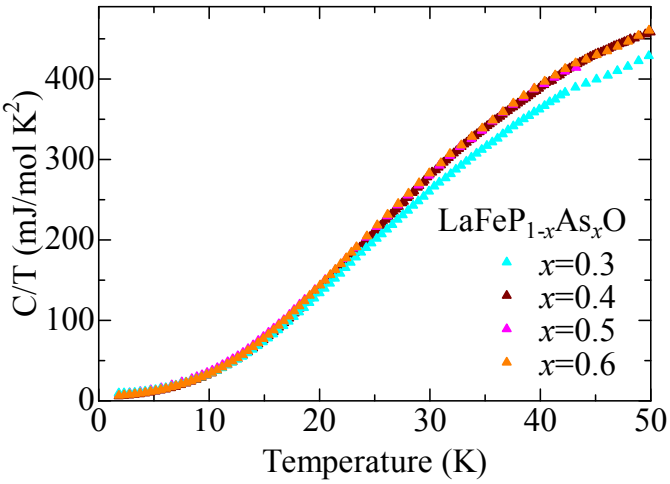

Figure 3.31: The temperature dependence of specific heat C/T of $LaFeP_{1-x}As_xO$ (x = 0.3, 0.4, 0.5 and 0.6).

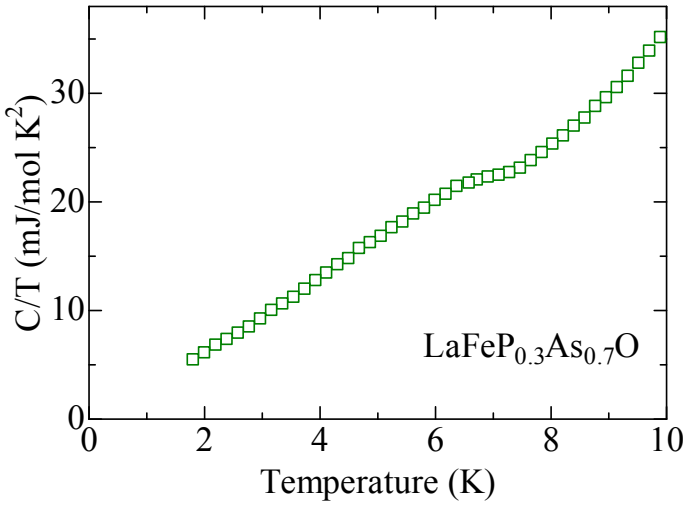

Figure 3.32: The temperature dependence of specific heat C/T of $LaFeP_{0.3}As_{0.7}O$.

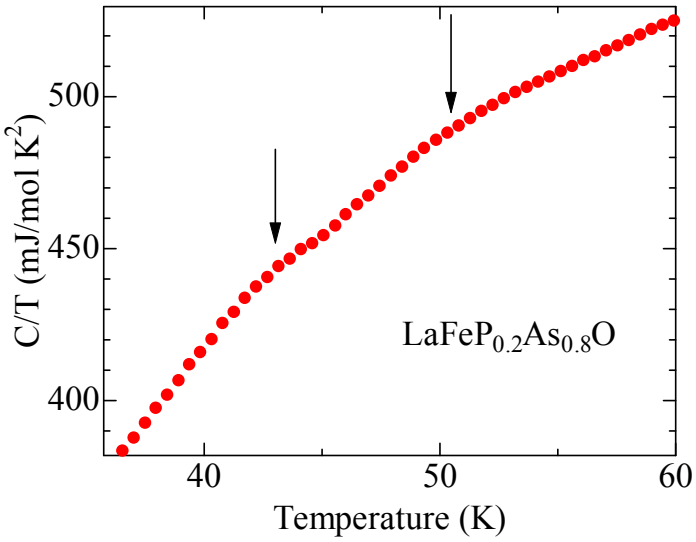

Figure 3.33: The temperature dependence of specific heat C/T of $LaFeP_{0.2}As_{0.8}O$. The arrows indicate the jump due to magnetic/structural transition.

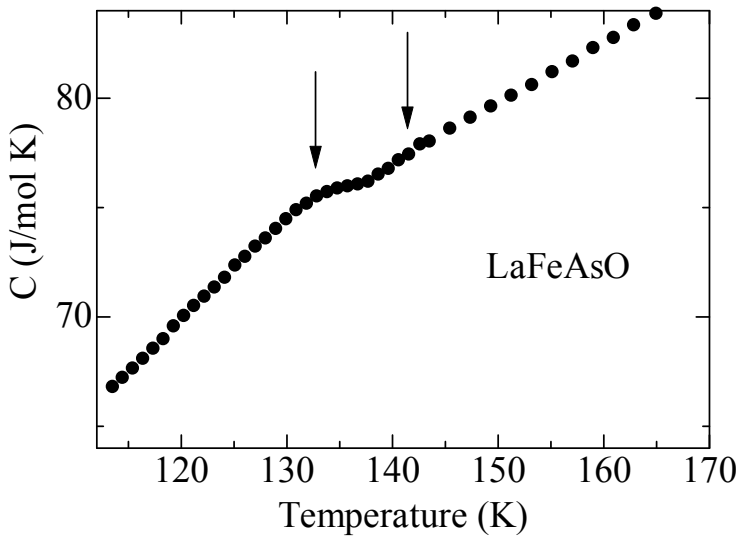

Figure 3.34: The temperature dependence of specific heat C of LaFeAsO. The arrows indicate the jump due to magnetic/structural transition.

In the sample of $x = 1.0$ (Fig. 3.34), a jump around $T = 135$ K is observed, indicating the magnetic transition from paramagnetic to SDW state which is consistent with the previous results [72, 98]. At T slightly above the magnetic transition ($\sim$145 K), there is a very small hump probably due to the structural transition.

A similar behavior can be found in temperature dependence of C at $x = 0.8$. Two small peaks are found around $T = 43$ K and 50 K, indicating the structural and magnetic transition temperature. This finding confirms that the upturn in resistivity at low temperatures is due to the emergence of the SDW state.

In the SC samples ($x = 0.2$ and 0.7), a jump corresponding the SC transition is observed. The jump can be more clearly visualized by plotting the temperature dependence of the coefficient of electron contribution γ, which is obtained from C/T subtracted by βT^2 according to Equation (2.7), as shown in Fig. 3.35. The value of T_c indicated by the jump of both samples is consistent with the results from the measurements of magnetic susceptibility and resistivity.

The samples in AFM2 phase ($x = 0.4$ – 0.6), however, do not show any anomalies

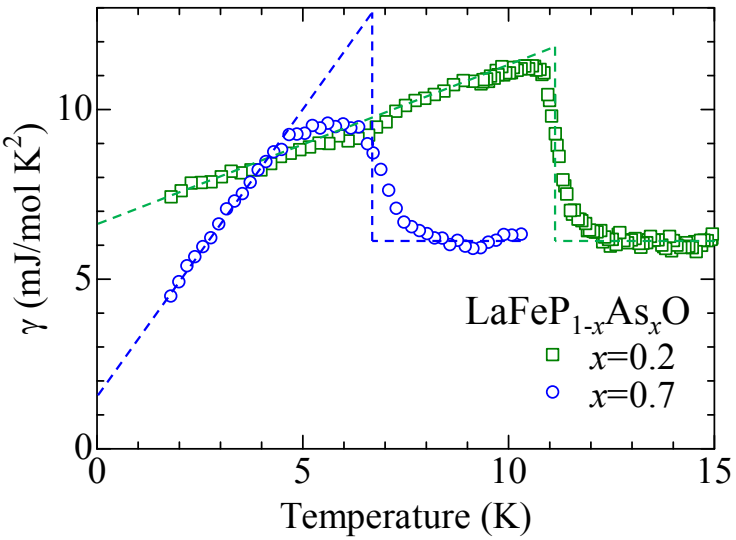

Figure 3.35: The temperature dependence of coefficient of electron contribution γ of $LaFeP_{0.8}As_{0.2}O$ and $LaFeP_{0.3}As_{0.7}O$.

in the temperature dependence. It suggests that there are no structural and magnetic transitions down to 2 K, while the magnetic transition has been observed in NMR measurements.

To realize the doping dependence of the electronic behaviors, the value of γ of each sample is obtained by fitting the data using Equation (2.7). The fitting of the data below 10 K for each sample is shown in Figs. 3.36 – 3.39. All the data can be well fitted by the linear fitting for the T^2 term, showing a good agreement with the predicted behavior of C/T at low temperatures.

It is worth noting that slight upturns at ∼3 K for $x = 0.3$, and at ∼4 K for $x = 0.8$ are visible in the corresponding plot of C/T against T^2 (see Figs. 3.37 and 3.39). It may indicate the SC transition in these samples.

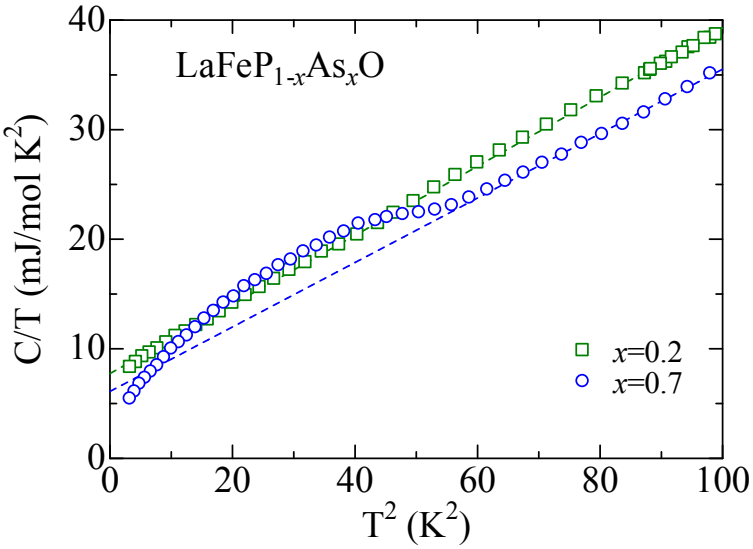

Figure 3.36: The T^2 dependence of specific heat C/T of $LaFeP_{1-x}As_xO$ with $x = 0.2$ and 0.7.

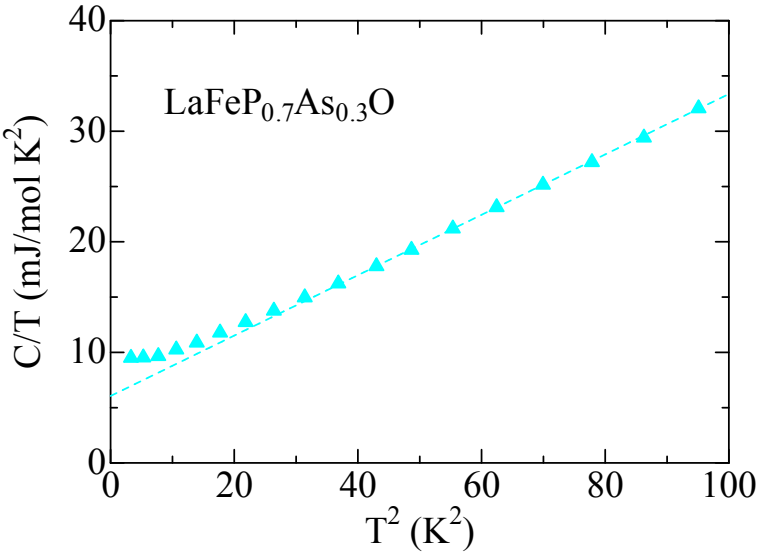

Figure 3.37: The T^2 dependence of specific heat C/T of $LaFeP_{0.7}As_{0.3}O$ with $x = 0.3$.

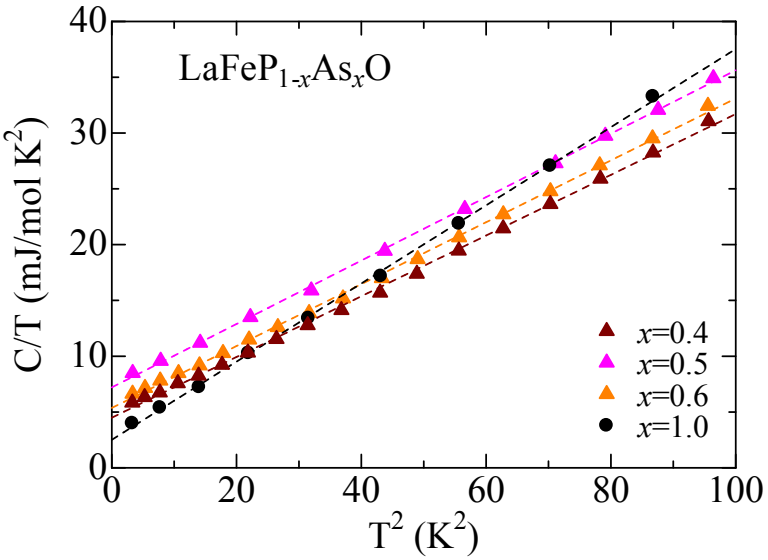

Figure 3.38: The T^2 dependence of specific heat C/T of $LaFeP_{1-x}As_xO$ with $x = 0.4$, 0.5, 0.6 and 1.0.

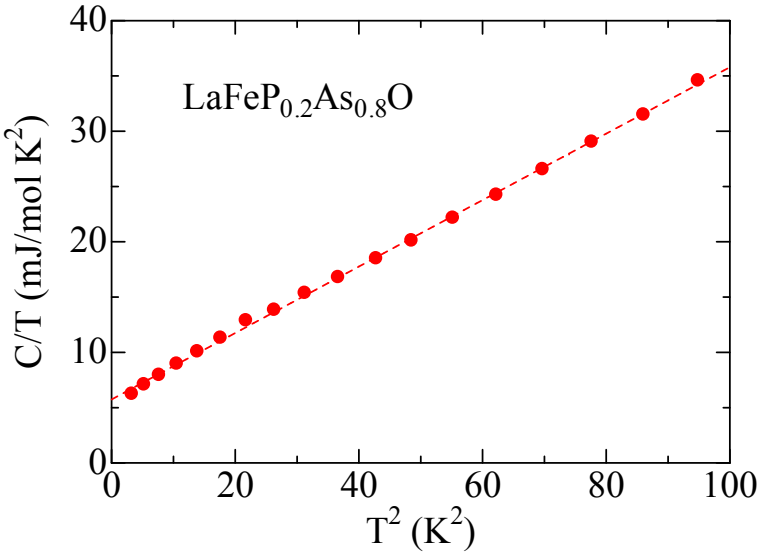

Figure 3.39: The T^2 dependence of specific heat C/T of $LaFeP_{0.2}As_{0.8}O$.

The doping dependence of the value of γ is then plotted in Fig. 3.40. Note that the data for the sample of $x = 0$ is adapted from our previous study of LaFePO [59]. Generally speaking, the value of γ decreases with increasing x. The decrease in γ is the most vigorous from $x \sim 0$ to 0.3. The further discussion about this behavior will be given in Section 4.1.1.

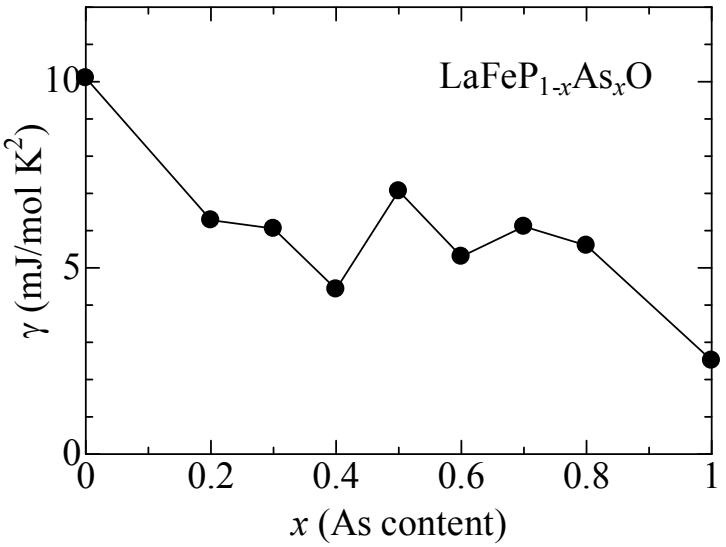

Figure 3.40: The x dependence of electronic specific heat coefficient γ of $LaFeP_{1-x}As_xO$.

Chapter 4

Discussions

4.1 The Behaviors of AFM2 Phase ($x = 0.3 - 0.6$) Found in $y = 0$

The appearance of AFM2 phase and SC2 dome in $LaFeP_{1-x}As_xO$ ($y = 0$) is unexpected and hard to explain by the existing theories. In this section, the experimental data for AFM2 phase will be discussed to understand the electronic properties of AFM2 phase.

4.1.1 Experimental Results of NMR

Figures 4.1 and 4.2 show the ^{31}P-NMR data for the series of $y = 0$ obtained by S. Kitagawa *et al.* [73] and H. Mukuda *et al.* [93], respectively. In particular, S. Kitagawa *et al.* have measured my samples of $x = 0.5$ and 0.6, while H. Mukuda *et al.* have measured the samples of $x = 0.3$ – 0.6 to identify the magnetic properties of AFM2 phase. For the samples of $x = 0.5$ and 0.6, a similar peak broadening is found below 15 K in both studies, indicating the presence of the magnetic order below 15 K. For the samples of 0.3 and 0.4, the peak broadening is found below ∼15K at $x = 0.3$ while that is found below ∼35 K at $x = 0.4$.

In the study of S. Kitagawa *et al.*, they have argued that the magnetic order in

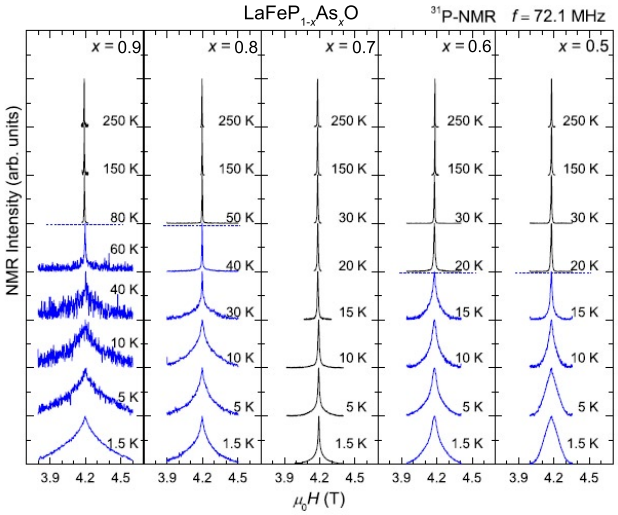

Figure 4.1: The NMR spectra of $LaFeP_{1-x}As_xO$ obtained by S. Kitagawa *et al.* [73].

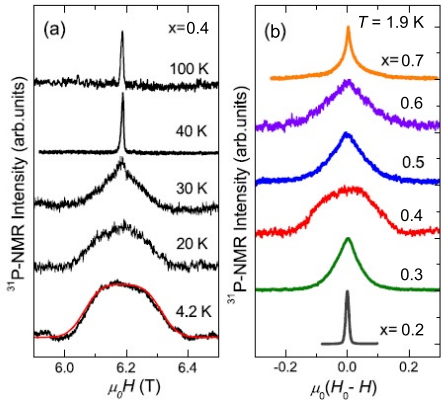

Figure 4.2: The NMR spectra of $LaFeP_{1-x}As_xO$ obtained by H. Mukuda *et al.* [93].

AFM2 phase is probably a short-ranged order. However, as shown in Fig. 4.2, the ^{31}P-NMR spectrum of the sample of $x = 0.4$ at the lowest temperature (4.2 K) exhibits a rectangular-like spectral shape. It indicates the sample is a randomly-oriented powder of commensurate AFM ordered compounds [55]. In other words, the study of H. Mukuda *et al.* suggests that the magnetic order in AFM2 phase is actually a long-ranged order. They have also suggested that the difference between AFM1 phase and AFM2 phase can be due to the wider bandwidth and larger itinerancy associated with the shorter Fe-As/P bond length in AFM2 phase.

Density of States at Fermi Level

On the other hand, the density of states at the Fermi level $D(E_F)$ for the series of $y = 0$ can be estimated from the Knight shift of the corresponding ^{31}P-NMR spectra. It can be revealed based on the fact that the Knight shift consists of a temperature-dependent spin shift $K_s(T)$ and a temperature-independent chemical shift K_{chem}, as well as the following relation:

$$K_s(T) \propto A_{hf} D(E_F), \tag{4.1}$$

where A_{hf} is the hyperfine coupling constant[1]. Basically the change of $D(E_F)$ across P/As substitution can be estimated from the change of K_s.

The corresponding x dependence of $K_s(T \to 0)$ extrapolating to 0 K is shown in Fig. 4.3. The value of $K_s(T \to 0)$ is generally decreasing with increasing x. It has been pointed out that the large value at $x = 0$ is by virtue of the sharp peak of the density of states of the d_{Z^2} band at Fermi level. Moreover, the great decrease in $K_s(T \to 0)$ at $x \sim 0.2 - 0.3$ reflects the shrinkage of the d_{Z^2} band at Fermi level, i.e. the d_{Z^2} band does not contribute to $D(E_F)$. Since the shrinkage of the d_{Z^2} band is near AFM2 phase, it suggests that this band may not be favorable for the emergence of AFM2 phase.

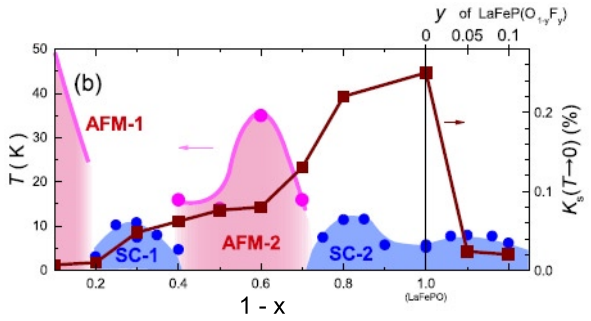

Figure 4.3: The x dependence of T_c, T_N and $K_s(T \to 0)$ of $LaFeP_{1-x}As_xO$ and $LaFePO_{1-y}F_y$ [93].

Meanwhile, $D(E_F)$ can also be estimated by the electronic specific heat coefficient γ

[1]Because A_{hf} depends on the coupling constant between Fe spin and P nucleus, it is possible to vary with x, but the value should be significantly small.

because

$$\gamma \propto D(E_F) \tag{4.2}$$

according to the Sommerfeld model [100].

As illustrated in Fig. 3.40, the x dependence shows a similar trend as obtained in the data for $K_s(T \to 0)$ in Fig. 4.3 that the density of states decreases with increasing x [2]. In particular, the great decrease around $x = 0.2$ – 0.3 is roughly reproduced in the specific heat measurements, confirming the picture about the shrinkage of the d_{Z^2} band.

4.1.2 Discussion on Hall Effect

In Section 3.4, we have discussed that the strong enhancement of $|R_H|$ at low temperatures is found in the samples of $x = 0.3$ – 0.6, i.e. within AFM2 phase (See Figs. 3.28 and 3.29). This kind of novel behaviors can be interpreted as follows. Since the AFM order may create a charge gap at some part of Fermi surface, it may decrease the number of charge carriers and thus enhance $|R_H|$ at low temperatures. Another fact is that the temperature dependence of R_H of these samples can be roughly fitted with the following equation derived from the spin fluctuation theory [101, 102]:

$$R_H = \frac{-\alpha_0}{T + \Theta}, \tag{4.3}$$

as shown in the dashed line in Fig. 3.28. Here α_0 and Θ are some constants. This relation suggests that the strong temperature dependence of $|R_H|$ is related to the presence of the backflow due to strong electron-electron scattering arising from spin fluctuations, which is consistent with the observation of low-energy spin fluctuations above T_N in these samples via ^{31}P-NMR measurements [73, 93]. Therefore, the enhancement of $|R_H|$ at $x = 0.3$ – 0.6 may be correlated to the AFM order in AFM2 phase.

[2] It is hard to compare the exact variation for each data point in the both measurements since there are some extrinsic factors like impurities to contribute some errors to the measurements. However, a qualitative comparison is valid.

Moreover, since the behaviors of R_H depends on the shape of Fermi surface, the origin of AFM2 phase is highly related to the reconstruction of the Fermi surface topology during P/As substitution. Although there are no theoretical studies about the Fermi surface topology in $LaFeP_{1-x}As_xO$, a theoretical calculation for $(Ca_4Al_2O_6)Fe_2(As_{1-x}P_x)_2$ has shown that the AFM phase around $x = 0.5$ – 0.9 appears because the topology of the Fermi surface reconstructs due to P/As substitution and gives a very good nesting for AFM ordering [103]. It suggests a possibility that the appearance of AFM2 phase is also due to a very good Fermi surface nesting when the Fermi surface changes during P/As substitution. In particular, the change of the Fermi surface in $LaFeP_{1-x}As_xO$ occurs through the crossover of the $d_{X^2-Y^2}$ and d_{Z^2} bands.

Before ending this section, it should be noted that this interpretation about the enhancement of $|R_H|$ cannot be adopted in the cases for $y = 0.05$ and 0.1 [82]. Although a similar enhancement of $|R_H|$ is observed around $x = 0.6$ – 0.8, the electronic state is far from the AFM order. This problem will be further discussed in Section 4.2.

4.1.3 Structural and Magnetic Transitions

In iron-based superconductors, the SDW transition is usually associated with the structural transition from tetragonal to orthorhombic with the transition temperature slightly above T_N. During the transition, there are some signatures to identify its presence. For example,

- Anomalies can be found in temperature dependent resistivity.
- A peak splitting, at the (220) Bragg peak for instance, can be observed in the corresponding XRD spectrum.
- A jump can be detected in temperature dependent specific heat.

Therefore, the detection of the above behaviors can help us to identify the presence of the structural transition and the corresponding transition temperature.

In our present data, however, it is not likely to show any structural transitions in AFM2 phase. For the resistivity data (see Fig. 3.8), the samples of $x = 0.3$, 0.4 and 0.6 shows metallic behaviors without any trace of anomalies. The sample of $x = 0.5$ shows a slight upturn at low temperatures. It may point out the influence due to the structural/magnetic transition, but it is too weak to give a solid conclusion.

In the temperature dependent XRD measurement, we have shown in Fig. 3.4 that there is no peak splitting in the Bragg peak (220) down to 20 K for the sample of $x = 0.4$. Moreover, there is no observation about the jump around T_N reported by NMR for the samples of $x = 0.3$ – 0.6 in the specific heat measurements (See Section 3.5). These results strongly suggest that there is no structural transition in AFM2 phase.

On the other hand, the lack of the jump in specific heat measurements also implies that the magnetic transition is not observable in specific heat. It may be related to the small magnetic moment of AFM2 phase ($\sim 0.18\mu_B$) [93]. If we look back to the NMR data as shown in Fig. 4.2, the peak broadening develops rather slowly with decreasing temperatures. Hence these results suggest that the magnetic transition may be smooth across T_N. Nevertheless, we cannot exclude the possibility that some extrinsic factors like impurities contribute to background to screen out the jump due to the magnetic, or even structural transition.

4.2 Phase Diagram of $\mathbf{LaFeP_{1-x}As_xO_{1-y}F_y}$ ($y = 0 - 0.1$): Effect of Band Crossover

The evolution of the electronic behaviors of $LaFeP_{1-x}As_xO_{1-y}F_y$ ($y = 0$ – 0.1) is summarized in the corresponding phase diagram, as illustrated in Fig. 4.4. At $y = 0$, the two SC domes (SC1 and SC2 domes) are separated by AFM2 phase. At $y = 0.05$, AFM1 and AFM2 phases disappear, and the two peaks are found in the SC dome. When $y = 0.1$, a single-dome structure is revealed.

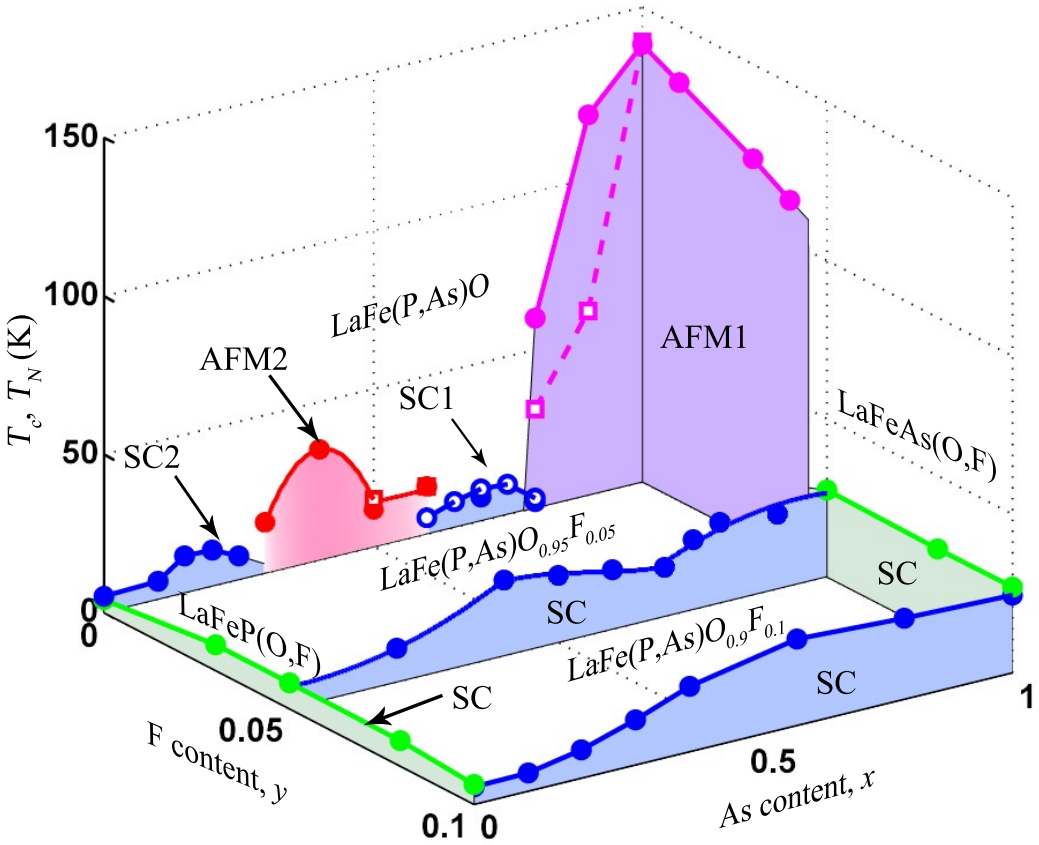

Figure 4.4: The phase diagram of $LaFeP_{1-x}As_xO_{1-y}F_y$ [56, 59, 72, 73, 82].

The existence of the two-dome structure at $y = 0$ and the two-peak structure at $y = 0.05$ suggests that there are two kinds of electronic states in P/As substituted La1111. The further evidence can be provided in the corresponding Hall effect measurements, as shown in Fig. 3.29. For $y = 0$, the strong temperature dependence of Hall coefficient R_H is found around $x = 0.3 - 0.8$, while such behavior can be found around $x = 0.6 - 0.8$ for $y = 0.05$. As discussed in Section 4.1.2, the behavior of R_H for $y = 0$ may be related to AFM2 phase, but it cannot explain the behaviors of R_H for other y. On the other hand, if we compare to the data for $y = 0.1$, these behaviors of R_H are reminiscent of the band crossover of the $d_{X^2-Y^2}$ and d_{Z^2} bands as discussed in Section 1.3. Following the same discussion, the strong temperature dependence of R_H suggests that the reconstruction

of the Fermi surface due to the interchange of the energy of the $d_{X^2-Y^2}$ and d_{Z^2} bands happens around $x = 0.3$ – 0.8 for $y = 0$ and around $x = 0.6$ – 0.8 for $y = 0.05$. Therefore, it indicates that there are two kinds of electronic states corresponding to two types of Fermi surface topology at the low-x region and the high-x region in P/As substituted La1111, and the crossover of these two electronic states causes the enhancement of $|R_H|$.

4.2.1 Relationship between SC and AFM

The evolution from the two-dome structure at $y = 0$ to the single-dome structure at $y = 0.1$ can be viewed as the expansion of SC2 dome with increasing y, and the expansion is due to the suppression of AFM2 phase through F doping. The spin fluctuation originating from AFM2 phase contributes to the development of SC at $x \sim 0.4$ in the series of $y = 0.05$, resulting in the expansion of the SC region. In the series of $y = 0.1$, the As-content for the maximum strength of spin fluctuations and the maximum value of T_c is shifted to $x = 0.6$. Hence it suggests that SC2 dome further expands and merges with SC1 dome, resulting in a single dome.

The spin fluctuations at $x \sim 0.4$ in the series of $y = 0.05$ and at $x \sim 0.6$ in the series of $y = 0.1$ have actually been detected by NMR technique [85]. It proves that the enhancement of T_c is correlated to the increase in spin fluctuations. The further discussion about the relationship between T_c and spin fluctuations can be continued by looking at the x dependence of T_c and the exponent n, as shown in Fig. 3.10. In SC2 dome (or in the lower x region), the enhancement of T_c is commonly associated with the decrease in the exponent n from 2. This implies that T_c increases with the development of spin fluctuations. Therefore, the SC in low-x region is more likely to be induced by spin fluctuations. In contrast, there is no clear correlation between T_c and the exponent n in larger x (As-rich) region, implying that it is hard to conclude whether the SC in high-x region is induced by spin fluctuations.

However, the above conclusions seem to contradict with the pairing mechanism pro-

posed by spin fluctuation theory [86]. If we adopt the band crossover picture, the SC mechanism should be controlled by the contribution of d_{z^2} band to Fermi surface in the low-x region. Moreover, the 2D Fermi surface dominated by $d_{x^2-y^2}$ band in the high-x region should be involved in the SC mechanism. However, in the framework of spin fluctuations, the 3D Fermi surface given from the d_{z^2} band does not contribute to the pairing force for SC, while the 2D Fermi surface in the high-x region is more likely to provide the pairing force for SC through spin fluctuations.

This suggests that the existing spin fluctuation theory based on Fermi surface nesting may not be enough to explain the SC mechanism in this system. Some modifications are necessary. In particular, the data for the density of states in Section 4.1.1 have suggested that the contribution of d_{z^2} band to the density of states decreases rapidly upon As doping for $y = 0$. As T_c increases from $x = 0$ to 0.2, it is possible that some contributions to pairing force from other bands arise when the energy of d_{z^2} band is leaving away from Fermi level. Of course we cannot exclude the possibility that other pairing mechanisms like orbital fluctuations are more suitable to explain the SC mechanism in this system.

Before leaving this section, it is worth mentioning that the exponent n approaches $\sim$1 around $x = 0.6$ in all y series, as shown in Fig. 3.10(d). Since the band crossover in the region of $0.3 \leq x \leq 0.8$ for $y = 0$ and at $x \sim 0.6$ – 0.8 for $y = 0.05$ and 0.1 is suggested by the Hall effect measurements, this behavior in n is possible to be one of the clues to indicate the band crossover. However, there is no theoretical model that connects T-linear behaviors of resistivity and the band crossover. This, together with the SC mechanism in high-x region, is a remaining puzzle.

4.2.2 Relationship between T_c and Structural Parameters

To study the relationship between T_c and pnictogen height h_{Pn} in $LaFeP_{1-x}As_xO_{1-y}F_y$, the corresponding data are plotted in Fig. 4.5 associated with the general trend con-

tributed by Y. Mizuguchi *et al.* [89].

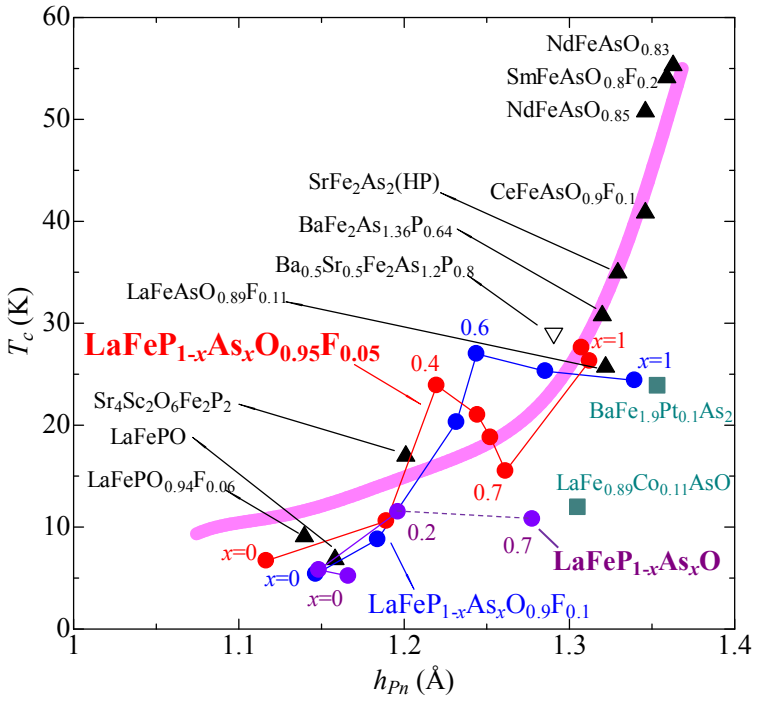

Figure 4.5: The plot of T_c and pnictogen height h_{Pn} [72, 82, 89, 104, 105]. The pink curve expresses the general trend for iron-based superconductors, which is constructed by Y. Mizuguchi *et al.* The purple, red and blue dots represent the data from $LaFeP_{1-x}As_xO_{1-y}F_y$ for $y = 0$, 0.05 and 0.1, respectively, and the value of x increases when the curve goes from left to right.

For $y = 0.1$ (the blue dots), the general trend is not followed at $x = 0.6$. For $y = 0.05$ (the red dots), a similar behavior can be observed, in which T_c decreases with increasing h_{Pn} from $x = 0.4$ to 0.7. For $y = 0$, the general trend is not followed for $x > 0.2$, especially by the virtue of the presence of AFM2 phase. Here we shall realize that the general trend is just a rough fitting and, more importantly, there are nearly no data to show the relationship between T_c and h_{Pn} around $h_{Pn} = 1.2 - 1.3$ Å. The disagreement between the general trend and our results suggests that this trend is not detailed enough to describe the relationship between T_c and h_{Pn} around $h_{Pn} = 1.2 - 1.3$ Å. More precisely, the relationship is not monotonic in this region and more complex

relationship should be applied instead.

The plot of pnictogen height against Fe-Fe atoms distance in Fig. 1.37 can also support the above argument. It is indicated in this plot that LaFePO changes from nodal SC to AFM when P is substituted by As. It fails to explain the complex electronic properties of $LaFeP_{1-x}As_xO$ observed in this study. As a result, we argue that the relationship between nodal SC, AFM and structural parameters is not as simple as the one indicated in the plot. A more complex picture is required to fully describe their relationship.

4.3 Comparison with other 1111 systems

In the previous section, we have addressed the picture of two electronic states in $LaFeP_{1-x}As_xO_{1-y}F_y$, and we have concluded that this picture is valid for $y = 0 - 0.1$. It is natural to ask whether this picture is applicable to other similar 1111 systems. In this section some comparisons will be made to find out the possibility to apply this picture to other systems.

4.3.1 Comparison with $SmFeP_{1-x}As_xO$

The electronic behaviors in $SmFeP_{1-x}As_xO$ [26, 74] show some similarities compared with $LaFeP_{1-x}As_xO$. In order to compare the electronic behaviors of both systems, the phase diagram of $SmFeP_{1-x}As_xO$ based on the resistivity data from Fig. 1.22 [74], together with the phase diagram of $LaFeP_{1-x}As_xO$, are plotted in Fig. 4.6.

It is obvious that both systems are AFM in the high-x region, but the AFM phase in $SmFeP_{1-x}As_xO$ persists down to $x \sim 0.5$. Moreover, there are two SC regions in the both systems but the SC domes in $SmFeP_{1-x}As_xO$ are much smaller. According to the resistivity data, the samples in the region around $x = 0.2 - 0.4$ (the green area in Fig. 4.6) show metallic behavior with any anomalies. It is reminiscent of the behaviors of

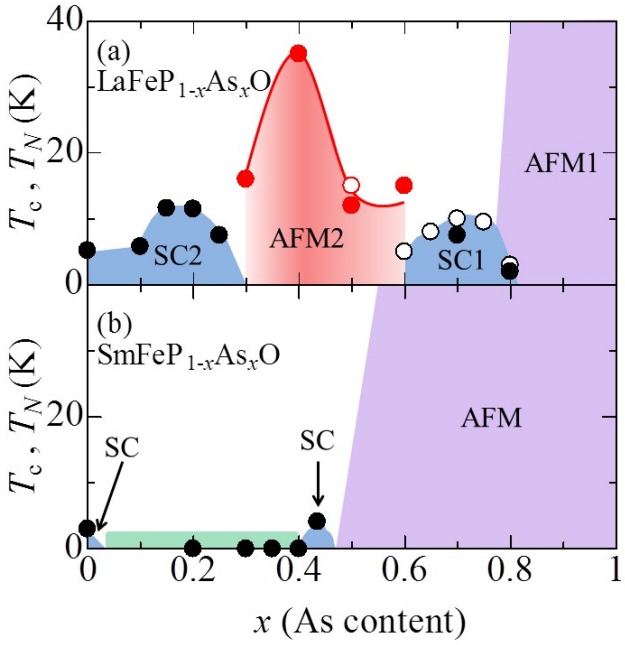

Figure 4.6: The phase diagrams of (a) $LaFeP_{1-x}As_xO$ and (b) $SmFeP_{1-x}As_xO$ [74].

resistivity in AFM2 phase of $LaFeP_{1-x}As_xO$. Moreover, that region also lies between the two SC regions in the phase diagram. Therefore, it is reasonable to expect that the samples in that region may show similar behaviors as AFM2 phase, i.e. some AFM ordering of Fe moments. It is also possible that the SC near $x = 0$ may persist in a large value of x, for example, 0.1. If it is actually observed in some future studies, it provides evidence that the feature of two SC domes separated by an AFM phase may be universal in P/As substituted 1111 systems, and once again proves the validity of the picture for two electronic states.

However, it should be reminded that AFM ordering of Sm moments with $T_N \sim 5$ K is observed in SmFePO [26]. The behaviors of the samples in the green region may show differences with AFM2 phase even though AFM ordering of Fe moments really exists.

4.3.2 Comparison with $LaFeAsO_{1-y}H_y$

As discussed in Section 1.1.3, $LaFeAsO_{1-y}H_y$ shows the two-dome structure in the corresponding phase diagram (see Fig. 1.20) [62, 71]. This feature is originated from the different spin/orbital fluctuations in the two SC domes due to the different topology of Fermi surface. Furthermore, the discovery of the AFM phase in heavily H-doped region has led to the conclusion that the two-dome structure is by virtue of the crossover of the two parent compounds.

On the other hand, it is revealed in this study that the behaviors of P/As substituted La1111 are correlated to the different two electronic states corresponding to LaFePO and LaFeAsO, respectively. Here we point out that the idea of the existence of two parent compounds in H-doped La1111 is similar to the idea of two electronic states in P/As substituted La1111. First, the term "two parent compounds" actually means the two different systems with two different kinds of electronic states, and the two states change from one to another through the substitution of an element (O/H and P/As). Second, the substitution of the corresponding element will cause the change of band structure and thus Fermi surface as well as the corresponding nesting in both H-doped La1111 and P/As substituted La1111. The reconstruction of Fermi surface during the crossover of the two states causes some anomalous behaviors, as we see the two-dome structure in $LaFeAsO_{1-y}H_y$ and the complicated phase diagram in $LaFeP_{1-x}As_xO$. Therefore, the picture of the two electronic states is also suitable to apply to the case of H-doped La1111. Of course the origin of the crossover of the two states is different in these two systems. More precisely, the crossover in H-doped La1111 comes from the switch of orbital characters during the enlargement of the electron pockets and the shrinkage of the hole pockets due to H doping, while the crossover in P/As substituted La1111 comes from the appearance of γ hole pocket when the amount of As content increases.

Finally, some comments will be made for the phase diagram of $LaFeP_{1-x}As_xO_{1-y}(F/H)_y$, as plotted in Fig. 4.7 according to the all existing data.

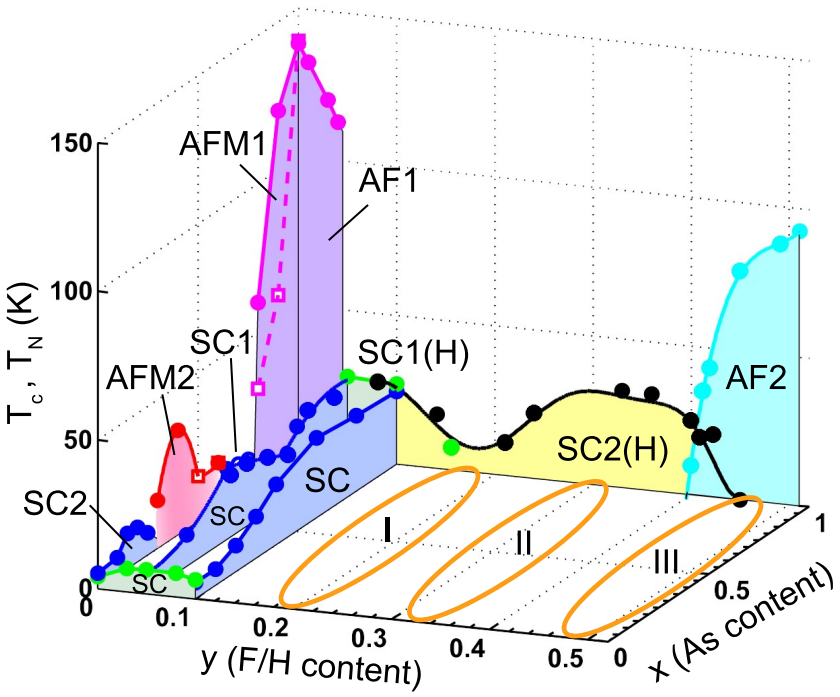

Figure 4.7: The phase diagram of $LaFeP_{1-x}As_xO_{1-y}(F/H)_y$ [56, 59, 71, 72, 73, 82].

We shall first discuss the possible behaviors in heavily H-doped $LaFePO_{1-y}H_y$. Due to the huge amount of electron doping, it is natural to forecast that the electron pockets enlarge and the hole pockets decrease in size. Hence the Fermi surface nesting will change. In particular, the electron-hole nesting will not be favorable due to the huge difference in the size of the electron and hole pockets. As a result, the electronic behaviors in the heavily H-doped region may not be as same as the behaviors in the low-y region.

We next discuss the possible behaviors in $LaFeP_{1-x}As_xO_{1-y}H_y$ for $y > 0.1$. For simplicity, the three regions located in the phase diagram (the orange areas) will be discussed. Region I lies on the region when SC1(H) and SC2(H) domes crossover. P/As substitution in this region may give us some interesting behaviors since the system will face two kinds of crossover effect around $x = 0.6$. Yet what the behaviors we will actually see are hard to forecast.

Region II lies on SC2(H) dome and the region of heavily H-doped $LaFePO_{1-y}H_y$. Since the electronic states of both As-end and P-end compounds are different from the low H-doped region, the effect of P/As substitution would be quite different from the samples for $y = 0.1$.

Region III is at AF2 phase in $LaFeAsO_{1-y}H_y$. The suppression of AFM in AF2 phase is expected due to the introduction of P, and hopefully SC will be induced. The behaviors in low-x region highly depend on the electronic state of heavily H-doped $LaFePO_{1-y}H_y$, so these behaviors may not be the same as the behaviors in $LaFeP_{1-x}As_xO$.

Chapter 5

Conclusions

5.1 Observations in $LaFeP_{1-x}As_xO$

In this study, the polycrystalline samples of $LaFeP_{1-x}As_xO$ for x 0 – 1 have successfully been synthesized. In particular, the samples of $x = 0.1$ – 0.3 had not been studied in the previous reports [24, 72]. The new SC dome (SC2 dome) has been found at $x = 0$ – 0.3. Together with SC1 dome at $x \sim 0.7$, a two-dome structure in the phase diagram is revealed.

More interestingly, apart from the AFM phase near LaFeAsO (AFM1 phase at $x =$ 0.8 – 0.1), another AFM phase has been observed at $x = 0.3$ – 0.6 (AFM2 phase) via ^{31}P-NMR measurements. The maximum T_N is ∼35 K. The magnetic order is a long-ranged order, but the magnetic moment is smaller than AFM1 phase. The measurements of XRD, resistivity and specific heat show no structural transition associated with the magnetic transition.

The magnetic transition is also not observed in specific heat measurements. Together with the NMR data, the results suggest that the magnetic transition is rather smooth. The density of states obtained from both the NMR and specific heat measurements shows a good agreement that it generally decreases with increasing x, and it particularly

drops sharper around $x = 0.2$ – 0.3. It suggests that the shrinkage of the d_{Z^2} band is important for the emergence of AFM2 phase.

Strong temperature dependence of R_H is observed in AFM2 phase. It suggests that the reconstruction of Fermi surface during P/As substitution is related to the formation of the AFM order in AFM2 phase, and the AFM order opens a charge gap at some parts of the Fermi surface.

5.2 Presence of Two Electronic States and Effect of Band Crossover in $LaFeP_{1-x}As_xO_{1-y}F_y$

The polycrystalline samples of $LaFeP_{1-x}As_xO_{0.95}F_{0.05}$ ($y = 0.05$) for $x = 0$ – 1 have also been synthesized to study the presence of two electronic states in P/As substituted La1111 system. A two-peak structure in the phase diagram is revealed. Together with the samples for $y = 0$ and 0.1 [82], the evolution of the electronic behaviors of $LaFeP_{1-x}As_xO_{1-y}F_y$ is revealed. Essentially, AFM2 phase in the series of $y = 0$ is suppressed by F doping, and the corresponding spin fluctuation causes SC2 dome to expand and merge with SC1 dome with increasing y. Consequently, it results in a double-peak structure for $y = 0.05$ and a single SC dome for $y = 0.1$.

Strong temperature dependence of R_H is observed at $x = 0.3$ – 0.8 for $y = 0$, and at $x \sim 0.6$ – 0.8 for $y = 0.05$ and 0.1. These results suggest that the reconstruction of Fermi surface takes place at these regions. According to the band calculation [86], it has been understood that the band structures of LaFePO and LaFeAsO are different from each other. The most obvious difference is that the Fermi surface at (π,π) is mainly controlled by d_{Z^2} band in LaFePO, while that is mainly controlled by $d_{X^2-Y^2}$ band in LaFeAsO. As a result, the hole Fermi surface γ pocket is absent in LaFePO while it is visible in LaFeAsO. Hence during P/As substitution, these two bands interchange, and the crossover from LaFePO-type Fermi surface to LaFeAsO-type Fermi surface, or

called *band crossover*, is naturally the origin of the strong temperature dependence of R_H. We believe that it indicates the presence of the two different kinds of electronic states across P/As substitution, and the band crossover are important factors to induce anomalous behaviors, such as the emergence of AFM2 phase, the two-dome structure, etc., in $LaFeP_{1-x}As_xO_{1-y}F_y$.

Moreover, the SC mechanism in low-x region is found to be correlated to spin fluctuations while that in high-x region is not conclusive. This result seems not to agree well with the existing spin fluctuation theory. It is possible that there are other bands which contribute to the pairing force for SC when the energy of d_{z^2} band is rapidly decreasing upon As doping.

On the other hand, the relationship between T_c and structural parameters around band crossover does not follow the prediction from the previous studies. It suggests that these studies are not precise enough to describe the correct relationship between T_c and structural parameters around band crossover. In particular, the relationship between T_c and pnictogen height h_{Pn} is not monotonic.

The electronic behaviors of $SmFeP_{1-x}As_xO$ and $LaFeAsO_{1-y}H_y$ are also compared. In $SmFeP_{1-x}As_xO$, it is possible to see a similar electronic behavior as $LaFeP_{1-x}As_xO$. It can prove that the feature of two SC domes separated by an AFM phase may be universal in P/As substituted 1111 systems. In $LaFeAsO_{1-y}H_y$, we argue that the picture for two electronic states is also applicable to this system since it is believed that there are two kinds of parent compounds inducing two different SC states, and the crossover of the two SC states gives an anomaly (a T_c valley).

In summary, the phase diagram of $LaFeP_{1-x}As_xO_{1-y}F_y$ can be well described by the presence of two kinds of electronic states. We also argue that the picture for two electronic states is valid not only for $LaFeP_{1-x}As_xO_{1-y}F_y$, but also other 1111 systems to describe the electronic behaviors in their phase diagrams.

5.3 Future Works

The further observations for AFM2 phase in $LaFeP_{1-x}As_xO$ are essential to understand the relationship between AFM2 phase and SC. Magnetic probe experiments like μSR and neutron scattering are highly recommended to be performed for further investigations. The understanding of Fermi surface topology in AFM2 phase is also important to reveal the origin of its electronic state. The related experimental and theoretical investigations are also recommended.

As discussed in Section 4.3.1, $SmFeP_{1-x}As_xO$ is possible to have a similar behavior as $LaFeP_{1-x}As_xO$. It is worth to further investigate the electronic behaviors at $x \sim 0$ – 0.5, especially the magnetic properties around $x = 0.2$ – 0.4 by some magnetic probes like NMR. It is also worth to synthesize $PrFeP_{1-x}As_xO$ and $NdFeP_{1-x}As_xO$, which had not been studied before, to investigate the x dependence of their electronic properties. Hopefully they may show similar behaviors as $LaFeP_{1-x}As_xO$, and further prove the validity of the presence of two kinds of electronic states in P/As substituted 1111 systems.

High pressure synthesis can also be applied to synthesize polycrystalline $LaFeP_{1-x}As_xO_{1-y}H_y$ and $LaFeP_{1-x}As_xO$ single crystals. It may be very difficult, but if the synthesis is successful, the effect of P/As substitution at heavily electron-doped region can be studied and more precise measurements on the electronic properties of $LaFeP_{1-x}As_xO$, such as angle-resolved photoemission spectroscopy (ARPES), can be performed to reveal the details of the band crossover.

Bibliography

[1] Y. Kamihara, T. Watanabe, M. Hirano, and H. Hosono, J. Am. Chem. Soc. **130**, 3296 (2008).

[2] X. H. Chen, T. Wu, G. Wu, R. H. Liu, H. Chen, and D. F. Fang, Nature **453**, 761 (2008).

[3] Z. A. Ren *et al.*, Chin. Phys. Lett. **25**, 2215 (2008).

[4] J .Zhao *et al.*, Nat. Mater. **7**, 953 (2008).

[5] Z. A. Ren *et al.*, EPL **82**, 57002 (2008).

[6] Z. A. Ren, J. Yang, W. Lu, W. Yi, G. C. Che, X. L. Dong, L. L. Sun, and Z. X. Zhao, Mater. Res. Innov. **12**, 105 (2008).

[7] P. Cheng *et al.*, Science in China G **51**(6), 719 (2008).

[8] M. Rotter, M. Pangerl, M. Tegel, and D. Johrendt, Angew. Chem. Int. Ed. **47**, 7949 (2008).

[9] J.-Q. Yan *et al.*, Phys. Rev. B **78**, 024516 (2008).

[10] H. S. Jeevan, Z. Hossain, Deepa Kasinathan, H. Rosner, C. Geibel, and P. Gegenwart, Phys. Rev. B **78**, 052502 (2008).

[11] S. Kasahara, T. Shibauchi, K. Hashimoto, Y. Nakai, H. Ikeda, T. Terashima, and Y. Matsuda, Phys. Rev. B **83**, 060505(R) (2011).

[12] X. C. Wang, Q. Q. Liu, Y. X. Lv, W. B. Gao, L. X. Yang, R. C. Yu, F. Y. Li, C. Q. Jin, Solid State Commun. **148**, 538 (2008).

[13] F. C. Hsu *et al.*, Proc. Natl. Acad. Sci. U.S.A. **105**, 14262 (2008).

[14] Clarina de la Cruz *et al.*, Nature **453**, 899 (2008).

[15] T. Nomura, S. W. Kim, Y. Kamihara, M. Hirano, P. V. Sushko, K. Kato, M. Takata, A. L. Shluger, and H. Hosono, Supercond. Sci. Technol. **21**, 125028 (2008).

[16] M. A. McGuire *et al.*, Phys. Rev. B **78**, 094517 (2008).

[17] Z. A. Ren and Z. X. Zhao, Adv. Mater. **21**, 4584 (2009).

[18] H. H. Wen, G. Mu, L. Fang, H. Yang, and X. Zhu, EPL **82**, 17009 (2008).

[19] C.-H. Lee *et al.*, J. Phys. Soc. Jpn. **77**, 083704 (2008).

[20] H. Okada, K. Igawa, H. Takahashi, Y. Kamihara, M. Hirano, H. Hosono, K. Matsubayashi, and Yoshiya Uwatoko, J. Phys. Soc. Jpn. **77**, 113712 (2008).

[21] P. M. Aswathy, L. B. Anooja, P. M. Sarun, and U. Syamaprasad, Supercond. Sci. Technol. **23**, 073001 (2010).

[22] D. A. Zocco *et al.*, Physica C **468**, 2229 (2008).

[23] H. Takahashi, K. Igawa, K. Arii, Y. Kamihara, M. Hirano, and H. Hosono, Nature **453**, 376 (2008).

[24] Y. Kamihara, H. Hiramatsu, M. Hirano, R. Kawamura, H. Yanagi, T. Kamiya, and H. Hosono, J. Am. Chem. Soc. **128**, 10012 (2006).

[25] R. E. Baumbach, J. J. Hamlin, L. Shu, D. A. Zocco, N. M. Crisosto, and M. B. Maple, New J. Phys. **11**, 025018 (2009).

[26] Y. Kamihara, H. Hiramatsu, M. Hirano, Y. Kobayashi, S. Kitao, S. Higashitaniguchi, Y. Yoda, M. Seto, and H. Hosono, Phys. Rev. B **78**, 184512 (2008).

[27] Y. Luo, Y. Li, S. Jiang, J. Dai, G. Cao, and Z. Xu, Phys. Rev. B **81**, 134422 (2010).

[28] M. Tegel, S. Johansson, V. Weis, I. Schellenberg, W. Hermes, R. Pöttgen, and D. Johrendt, EPL **84**, 67007 (2008).

[29] X. Zhu, F. Han, P. Cheng, G. Mu, B. Shen, L. Fang, and H. H. Wen, EPL **85**, 17011 (2009).

[30] S. Matsuishi, Y. Inoue, T. Nomura, H. Yanagi, M. Hirano, and H. Hosono, J. Am. Chem. Soc. **130**, 14428 (2008).

[31] S. Matsuishi, Y. Inoue, T. Nomura, Y. Kamihara, M. Hirano, and H. Hosono, New J. Phys. **11**, 025012 (2008).

[32] S. Matsuishi, Y. Inoue, T. Nomura, M. Hirano, and H. Hosono, J. Phys. Sci. Jpn. **77**, 113709 (2008).

[33] P. Cheng, B. Shen, G. Mu, X. Zhu, F. Han, B. Zeng, and H. H. Wen, EPL **85**, 67003 (2009).

[34] M. Ishikado, S. Shamoto, H. Kito, A. Iyo, H. Eisaki, T. Ito, and Y. Tomioka, Physica C **469**, 901 (2008).

[35] N. D. Zhigadlo, S. Katrych, Z. Bukowski, S.Weyeneth, R. Puzniak, and J. Karpinski, J. Phys.: Condens. Matter **20**, 342202 (2008).

[36] H. Ding *et al.*, EPL **83**, 47001 (2008).

[37] K. Kihou *et al.*, J. Phys. Sci. Jpn. **79**, 124713 (2010).

[38] K. Hashimoto *et al.*, Phys. Rev. B **82**, 014526 (2010).

[39] J.-H. Chu, J. G. Analytis, C. Kucharczyk, and I. R. Fisher, Phys. Rev. B **79**, 014506 (2009).

[40] S. Kasahara *et al.*, Phys. Rev. B **81**, 184519 (2010).

[41] S. A. J. Kimber *et al.*, Nat. Mater. **8**, 471 (2009).

[42] H. Kotegawa, H. Sugawara, and H. Tou, J. Phys. Sci. Jpn. **78**, 013709 (2009).

[43] M. S. Torikachvili, S. L. Bud'ko, N. Ni, and P. C. Canfield, Phys. Rev. Lett. **101**, 057006 (2008).

[44] A. Kreyssig *et al.*, Phys. Rev. B **78**, 184517 (2008).

[45] R. Mittal *et al.*, Phys. Rev. B **83**, 054503 (2011).

[46] X. G. Luo *et al.*, New J. Phys. **13**, 053011 (2011).

[47] Y. Zhang *et al.*, Nat. Mat. **10**, 273 (2011).

[48] T. Qian *et al.*, Phys. Rev. Lett. **106**, 187001 (2011).

[49] Y. J. Yan, M. Zhang, A. F. Wang, J. J. Ying, Z. Y. Li, W. Qin, X. G. Luo, J. Q. Li, Jiangping Hu, and X. H. Chen, Sci. Rep. **2**, 212 (2012).

[50] B. Wei *et al.*, Chin. Phys. Lett. **28**, 086104 (2011).

[51] W. Li *et al.*, Nat. Phys. **8**, 126 (2012).

[52] L. Sun *et al.*, Nature **483**, 67 (2012).

[53] K. Mydeen, E. Lengyel, Z. Deng, X. C. Wang, C. Q. Jin, and M. Nicklas, Phys. Rev. B **82**, 014514 (2010).

[54] S. Kakiya, K. Kudou, Y. Nishikubo, K. Oku, E. Nishibori, H. Sawa, T. Yamamoto, T. Nozaka, and M. Nohara, J. Phys. Sci. Jpn. **80**, 093704 (2011).

[55] H. Kinouchi, H. Mukuda, Y. Kitaoka, P. M. Shirage, H. Fujihisa, Y. Gotoh, H. Eisaki, and A. Iyo, Phys. Rev. B **87**, 121101(R) (2013).

[56] H. Luetkens et al., Nat. Mater. **8**, 305 (2009).

[57] A. J. Drew *et al.*, Nat. Mater. **8**, 310 (2009).

[58] S. Takeshita, R. Kadono, M. Hiraishi, M. Miyazaki, A. Koda, Y. Kamihara, and Hideo Hosono, J. Phys. Soc. Jpn. **77**, 103703 (2008).

[59] S. Suzuki, S. Miyasaka, S. Tajima, T. Kida, and M. Hagiwara, J. Phys. Soc. Jpn. **78**, 114712 (2009).

[60] T. Hanna, Y. Muraba, S. Matsuishi, N. Igawa, K. Kodama, S. Shamoto, and H. Hosono, Phys. Rev. B **84**, 024521 (2011).

[61] S. Matsuishi, T. Hanna, Y. Muraba, S. W. Kim, J. E. Kim, M. Takata, S. Shamoto, R. I. Smith, and H. Hosono, Phys. Rev. B **85**, 014514 (2012).

[62] S. Iimura, S. Matuishi, H. Sato, T. Hanna, Y. Muraba, S. W. Kim, J. E. Kim, M. Takata, and Hideo Hosono, Nat. Commun. **3**, 932 (2012).

[63] H. Hosono and S. Matsuishi, Curr. Opin. Solid State Mater. Sci. **17**, 49 (2013).

[64] N. W. Ashcroft and N. D. Mermin, Solid State Physics, 345 (1976).

[65] S. Iimura *et al.*, Phys. Rev. B **88**, 060501(R) (2013).

[66] K. Suzuki, H. Usui, L. Kuroki, S. Iimura, Y. Sato, S. Matsuishi, and H. Hosono, J. Phys. Soc. Jpn. **82**, 083702 (2013).

[67] Y. Yamakawa, S. Onari, H. Kontani, N. Fujiwara, S.Iimura, and H. Hosono, Phys. Rev. B **88**, 041106(R) (2013).

[68] K. Suzuki, H. Usui, S. Iimura, Y. Sato, S. Matsuishi, H. Hosono, and K. Kuroki, arXiv:1311.2413v1.

[69] S. Onari, Y. Yamakawa, and H. Kontani, Phys. Rev. Lett. **112**, 187001 (2014).

[70] N. Fujiwara, S. Tsutsumi, S. Iimura, S. Matsuishi, H. Hosono, Y. Yamakawa, and H. Kontani, Phys. Rev. Lett. **111**, 097002 (2013).

[71] M. Hiraishi *et al.*, Nat. Phys. **10**, 300 (2014).

[72] C. Wang, S. Jiang, Q. Tao, Z. Ren, Y. Li, L. Li, C. Feng, J. Dai, G. Cao, and Z. A. Xu, EPL **86**, 47002 (2009).

[73] S. Kitagawa, T. Iye, Y. Nakia, K. Ishida, C. Wang , G.-H. Cao, and Z.-A. Xu, J. Phys. Soc. Jpn. **83**, 023707 (2014)

[74] Y. Li, X. Lin, T. Zhou, J. Shen, Y. Luo, Q. Tao, G. Cao, Z. Xu, Physica C **470**, 493 (2009).

[75] N. D. Zhigadlo *et al.*, Phys. Rev. B **84**, 134526 (2011).

[76] S. Matsuishi, T. Maruyama, S. Iimura, and H. Hosono, Phys. Rev. B **89**, 094510 (2014).

[77] A. Jesche *et al.*, Phys. Rev. B **86**, 0200501(R) (2012).

[78] Y. Luo, H. Han, S. Jiang, X. Lin, Y. Li, J. Dai, G. Cao, and Z. Xu, Phys. Rev. B **83**, 054501 (2011).

[79] S. Sharma, J. Prakash, G. S. Thakur, A. T. Satya, A. Bharathi., A. K. Ganguli, and C. S. Sundar, Supercond. Sci. Technol. **24**, 065020 (2011).

[80] S. Saijo, S. Suzuki, S. Miyasaka, and S. Tajima, Physica C **470**, S298 (2010).

[81] S. Miyasaka, A. Takemori, S. Saijo, S. Suzuki, and S. Tajima, J. Phys. Chem. Solid **72**, 414 (2011).

[82] S. Miyasaka, A. Takemori, T. Kobayashi, S. Suzuki, S. Saijo, and S. Tajima, J. Phys. Soc. Jpn. **82**, 124706 (2013).

[83] T. Moriya, Y. Takahashi, and K. Ueda, J. Phys. Soc. Jpn. **59**, 2905 (1990).

[84] H. Kontani and S. Onari, Phys. Rev. Lett. **104**. 157001 (2010).

[85] H. Mukuda, F. Engetsu, K. Yamamoto, K. T. Lai, M. Yashima, Y. Kitaoka, A. Takemori, S. Miyasaka, and S. Tajima, Phys. Rev. B **89**, 064511 (2014).

[86] K. Kuroki, H. Usui, S. Onari, R. Arita, and H. Aoki, Phys. Rev. B **79**, 224511(2009).

[87] V. Vildosola, L. Pourovskii, R. Arita, S. Biermann, and A. Georges, Phys. Rev. B **78**, 064518 (2008).

[88] S. Ishida *et al.*, Phys. Rev. B **81**, 094515 (2010).

[89] Y. Mizuguchi, Y. Hara, K. Deguchi, S. Tsuda, T. Yamaguchi, K. Takeda, H. Kotegawa, H. Tou, and Y. Takano, Supercond. Sci. Technol. **23**, 054013 (2010).

[90] K. Terashima *et al.*, Proc. Natl. Acad. Sci. USA **106**, 7330 (2009).

[91] F. Izumi, and K. Momma, Solid. State. Phenom. **130**, 15 (2007).

[92] A. R. Denton and N. W. Ashcroft, Phys. Rev. A **43**, 3161 (1991).

[93] H. Mukuda , F. Engetsu, T. Shiota, K. T. Lai, M. Yashima, Y. Kitaoka, S. Miyasaka, and S. Tajima, J. Phys. Soc. Jpn. **83**, 083702 (2014).

[94] Y. Jia, P. Cheng, L. Fang, H. Luo, H. Yang, C. Ren, L. Shan, C. Gu, and H. Wena, Appl. Phys. Lett. **93**, 032503 (2008).

[95] A. Jesche, F. Nitsche, S. Probst, Th. Doert, P. Müller, and M. Ruck, Phys. Rev. B **86**, 134511 (2012).

[96] J. Dai, Q. Si, J.-X. Zhu, and E. Abrahams, Proc. Natl. Acad. Sci. U.S.A. **106**, 4118 (2009).

[97] N. W. Ashcroft and N. D. Mermin, Solid State Physics, 240 (1976).

[98] I. Pallecchi, F. Bernardini, F. Caglieris, A. Palenzona, S. Massidda, and M. Putti, Eur. Phys. J. B **86**, 338 (2013).

[99] Y. Kohama, Y. Kamihara, S. Riggs, F. F. Balakirev, T. Atake, M. Hirano, and H. Hosono, EPL **84**, 37005 (2008).

[100] J. Singleton, Band Theory and Electronic Properties of Solids, 12 (2001).

[101] H. Kontani, K. Kanki, and K. Ueda, Phys. Rev. B **59**, 14723 (1999).

[102] Y. Nakajima *et al.*, J. Phys. Soc. Jpn. **76**, 024703 (2007).

[103] H. Usui, K, Suzuki, K. Kuroki, N. Takeshita, P. M. Shirage, H. Eisaki, and A. Iyo, Phys. Rev. B **87**, 174528 (2013).

[104] H. Okabe, N. Takeshita, K. Horigane, T. Muranaka, and J. Akimitsu, Phys. Rev. B **81**, 205119 (2010).

[105] S. Adachi, T. Murai, and K. Tanabe, Physica C **483**, 67 (2012).

List of Publications

- *K. T. Lai*, A. Takemori, S. Miyasaka, F. Engetsu, H. Mukuda, and S. Tajima, **"Evolution of the phase diagram of $\mathbf{LaFeP_{1-x}As_xO_{1-y}F_y}$ $(y = 0 - 0.1)$"**, accepted for publication in Phys. Rev. B.

- H. Mukuda , F. Engetsu, T. Shiota, *K. T. Lai*, M. Yashima, Y. Kitaoka, S. Miyasaka, and S. Tajima, **"Emergence of Novel Antiferromagnetic Order Intervening between Two Superconducting Phases in $\mathbf{LaFe(As_{1-x}P_x)O}$: ^{31}P-NMR Studies"**, J. Phys. Soc. Jpn. **83**, 083702 (2014).

- H. Mukuda, F. Engetsu, K. Yamamoto, *K. T. Lai*, M. Yashima, Y. Kitaoka, A. Takemori, S. Miyasaka, and S. Tajima, **"Enhancement of superconducting transition temperature due to antiferromagnetic spin fluctuations in iron pnictides $\mathbf{LaFe(As_{1-x}P_x)(O_{1-y}F_y)}$: ^{31}P-NMR studies"**, Phys. Rev. B **89**, 064511 (2014).

- *K. T. Lai*, A. Takemori, S. Miyasaka, S. Tajima, A. Nakao, H. Nakao, R. Kumai, and Y. Murakami, **"Suppression of Superconductivity around $x = 0.5 - 0.7$ in $\mathbf{LaFeP_{1-x}As_xO_{0.95}F_{0.05}}$"**, JPS Conf. Proc. **1**, 012104 (2014).

List of Conferences

- *K. T. Lai*, A. Takemori, S. Miyasaka, S. Tajima, H. Nakao, R. Kumai, and Y. Murakami.

  Oral presentation: "Transport properties of $LaFeP_{1-x}As_xO_{1-y}F_y$: Evidence for two superconducting states".

  IRON-SEA Meeting 2014, Nagoya, Japan

- *K. T. Lai*, A. Takemori, S. Miyasaka, S. Tajima, H. Nakao, R. Kumai, and Y. Murakami.

  Oral presentation: "Transport properties of $LaFeP_{1-x}As_xO_{1-y}F_y$: Evidence for two superconducting states".

  American Physics Society March Meeting 2014, Denver, USA

- *K. T. Lai*, A. Takemori, S. Miyasaka, S. Tajima, H. Nakao, R. Kumai, and Y. Murakami.

  Oral presentation (O-1-02): "Crossover of the two electronic states in $LaFeP_{1-x}As_xO_{1-y}F_y$ ".

  International Workshop on Superconductors and Super Materials 2013, Tokyo, Japan

- *K. T. Lai*, A. Takemori, S. Miyasaka, S. Tajima, H. Nakao, R. Kumai, and Y. Murakami.

  Oral presentation (PC-13): "Crossover of the two electronic states in $LaFeP_{1-x}As_xO_{1-y}F_y$ ".

  The 26th International Symposium on Superconductivity 2013, Tokyo, Japan

- *K. T. Lai*, A. Takemori, S. Miyasaka, S. Tajima, H. Nakao, R. Kumai, and Y. Murakami.

  Poster presentation (P1): "Two superconducting states in $LaFeP_{1-x}As_xO_{1-y}F_y$ ".

  Workshop in Institute of Fundamental Physics in Kyoto University 2013: Physics in Iron-based Superconductors, Kyoto, Japan

- *K. T. Lai*, A. Takemori, S. Miyasaka, S. Tajima, H. Nakao, R. Kumai, and Y. Murakami.

  Oral presentation (27aEC-5): "Relation between superconductivity and antiferromagnetic order/fluctuation around $x = 0.5$ – 0.7 in $LaFeP_{1-x}As_xO_{1-y}F_y$ ".

  The Japan Physics Society Fall Meeting 2013, Tokushima, Japan

- *K. T. Lai*, A. Takemori, S. Miyasaka, S. Tajima, A. Nakao, H. Nakao, R. Kumai, and Y. Murakami.

  Oral presentation (A6-2-O2): "Suppression of Superconductivity due to Antiferromagnetic Order around $x = 0.5$ – 0.7 in $LaFeP_{1-x}As_xO_{0.95}F_{0.05}$".

  The 12th Asia Pacific Physics Conference 2013, Chiba, Japan

- *K. T. Lai*, A. Takemori, S. Miyasaka, and S. Tajima.

  Poster presentation: "Coexistence of superconductivity and antiferromagnetic order/fluctuation around $x = 0.6$ – 0.8 in $LaFeP_{1-x}As_xO_{0.95}F_{0.05}$".

  IRON-SEA Meeting 2013, Osaka, Japan

- *K. T. Lai*, A. Takemori, S. Miyasaka, and S. Tajima.

  Poster presentation (Poster No. 10): "Coexistence of superconductivity and antiferromagnetic order/fluctuation around $x = 0.6$ – 0.8 in $LaFeP_{1-x}As_xO_{0.95}F_{0.05}$". **The 2nd Osaka-Netherlands Joint Symposium 2012**, Osaka, Japan